An investigation of using micromachined silicon diaphragms in high temperature pressure sensors

By

JUAN REN

A thesis submitted to

The University of Birmingham

for the degree of

DOCTOR OF PHILOSOPHY

School of Mechanical Engineering

College of Engineering

The University of Birmingham

2012

Abstract

Micromachined silicon diaphragms have been widely used as sensing elements in standard pressure sensors. However, at elevated temperature, the pressurized silicon diaphragms may suffer from the plastic deformation or creep. Therefore, this project is to investigate the possibility of using silicon diaphragms in high temperature pressure sensors.

A series of experiments were performed to investigate the effect of size, temperature and ion implantation on the mechanical behaviour of the micromachined silicon diaphragms. The test structures were annealed under the atmospheric pressure at a temperature of 600°C, 800°C and 900°C, respectively. The surface profiles of the diaphragms were measured with respect to the anneal time. Based on the experimental results, the suggestions of the design of the silicon diaphragms for the high temperature pressure sensors were given. Moreover, the onset of the plastic deformation was predicted by the theory of the critical resolved shear stress. The predicted behaviour was in good agreement with the experimental observation for the heavily-boron-doped silicon diaphragms. Finally, the constitutive equations were implemented in Comsol Multiphysics to simulate the evolution of the diaphragm deformation in the initial anneal stage. The model successfully predicted the deflections for the diaphragms with a radius from 0.5mm to 2.0mm at 900°C.

Acknowledgements

First and foremost I offer my sincerest gratitude to my supervisor, Dr Michael Ward, who has supported me thoughout my PhD study with his patience and encouragement. His passion for research and broad knowledge of MEMS sensors play an important role in pushing the research project forward. Also, he supported me to take part in various training courses and international conferences.

Secondly, I would like to thank the sponsor of the project, GE Druck, for their financial support and the technique support. Special thanks have to be given Russell Craddock, Peter Kinnell and Martin Geear for generously sharing the knowledge of the micromachined pressure sensors, and kindly providing help in the fabrication of the test structures.

I would also like to thank many members in the Bio-Medical and Micro Engineering Centre. Thank Dr Carl Anthony for his interest in the project, and he was always there for help when I got problem in the clean room. Thank Dr Emma Carter, with who I had both lovely time and sad time. But I will never forget her great help for me. Dr Jason Teng gave useful guidance in the use of FIB and showed me how to make TEM samples. Mr Ken Dawkins trained me the use of clean room facilities, including the lithographer and the STS etcher. And thank Mr Alan Saywell for showing me the use of the software Talymap. I am also very grateful to those who have given me useful advices to the research, including Professor Phil Prewett, Dr. Xianzhong Chen, Dr Raya Al-Dadah and Mr Meng Pan.

In addition, I am also very grateful to those who gave me help outside the research group. Dr Mike Keeble, in BUEHLER Laboratory UK, helped to take many nice microscopic photos for the test samples. Dr Peter Hartley in our department taught me the basics of continuum mechanics. I would like to thank all the staff in the Centre for Electron Microscopy. Especial thank is given Ms Ming Chu for training me to use SEM and helping to lift out the TEM samples. Thank Dr Jon Petzing and Mr Singh Jagpal, in the Wolfson School of Mechanical & Manufacturing Engineering in the Loughborough University, for training me to use Zygo 5000, and were there to help when I was making the measurements. I would also like to express my deep thanks to James Bowen, in the School of Chemical Engineering, who helped me to access the facility in Birmingham Science City.

Most importantly, I would like to thank my parents for their great love and encouragement. And I would like to thank my husband Xueyong Wei. He is always there for me and encourages me to overcome the difficulties in the research.

Table of contents

List of illustrations

List of tables

List of abbreviations

MEMS: Micro Electro Mechanical Systems

SiC: Silicon Carbide

SEM: Scanning Electron Microscope

SCS: Single Crystal Silicon

IC: Integrated Circuit

RF: Radio Frequency

Q-factor: Quality Factor

SOI: Silicon on Insulator

CVD: Chemical Vapour Deposition

DETF: Double-Ended Tuning Fork

PECVD: Plasma-Enhanced Chemical Vapour Deposition

RIE: Reactive-Ion Etching

BDT: Brittle-to-Ductile Transition

AFM: Atomic Force Microscope

RT: Room Temperature

CTE: Coefficient of Thermal Expansion

FEA: Finite Element Analysis

BESOI: Bond and Etch Back Silicon On Insulator

DRIE: Deep Reactive-Ion Etch

CRSS: Critical Resolved Shear Stress

TEM: Transmission Electron Microscope

FIB: Focused Ion Beam

1 INTRODUCTION

1.1 *Research background*

An increased demand for precision measurements in extreme conditions has stimulated the development of MEMS (Micro Electro Mechanical Systems) sensors for harsh environments. Many efforts have been focused on pressure sensors for high temperature applications due to the needs from the automotive and aerospace industries. SiC has been considered as the candidate material for the high temperature pressure sensors because it has good mechanical and thermal stability and a wide bandgap for stable electronic properties at elevated temperatures [1-1]. However, microfabrication technology of SiC is not mature and the cost for SiC-based MEMS sensors is very high [1-1]. Therefore, the development of high temperature low-cost pressure sensors is very attractive.

MEMS mechanical sensors derive enormous benefits from the use of silicon in the sensing elements [1-2]. The availability of the batch fabrication of silicon manufacturing techniques enables high-precision small-size devices to be widely used in many areas of industrial activity with low cost. Because the mechanical properties of silicon start to deteriorate above 500°C, the use of silicon in high temperature sensors is restricted. However, for the sake of reduced cost, it is worthy to extend the operating temperatures of existing Si-based pressure sensors.

1.2 *Problem statement*

This project is sponsored by GE Druck Limited. The company is a global supplier of MEMS pressure sensors. The aim of the project is to explore the operating limits of Si-based pressure sensing diaphragms in high temperature environments (≥600°C). Silicon diaphragms are the basic components for most standard micromachined pressure sensors. Normally, the sensor determines the magnitude of the pressure by detecting the deformation or the stress/strain in the pressure sensing diaphragm using various transduction mechanisms. The SEM photo of a pressure sensing diaphragm used in Druck sensors is shown in Figure 1- 1(a). There are two bosses on the backside of the diaphragm to allow electrical connection with the transducer. The pressure is applied to the other side of the diaphragm which is flat. The diaphragm works perfectly at room temperatures.

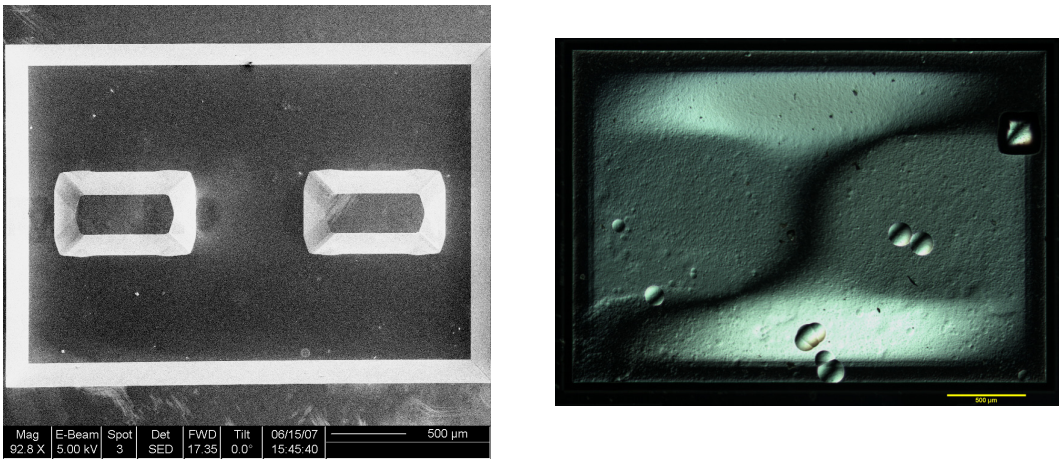

(a) (b)

Figure 1- 1 Druck pressure sensing diaphragm. (a) SEM photo of the diaphragm backside with bosses. (b) Microscopic photo of the diaphragm front side after annealing at 1100°C

The idea of using silicon diaphragms to sense pressure in high temperature environment is stimulated for two reasons. Firstly, the micromachining process of Si is mature and cost-effective. Secondly, it has been shown that the SCS (single crystal

silicon) pressure sensing diaphragm with carefully designed dimensions is capable of operating at very high temperature (500°C) [1-3].

The problem with current Druck silicon diaphragms is the occurrence of the plastic deformation at elevated temperatures. Figure 1- 1(b) shows the front side of the deformed diaphragm after annealing at 1100°C under atmospheric pressure for 2 hours. The elastic deformation, due to the applied pressure, was released by milling a small hole through the diaphragm. Since the plastic deformation is permanent, the diaphragm still deforms downward after unloading (the deformation may look like upward in Figure 1- 1(b) due to the effect of the reflective light from the diaphragm surface).

The observation of the plastic deformation raises several questions:

- Why the silicon diaphragm failed after annealing at 1100°C while its behaviour before annealing is perfect for micromachined pressure sensors?
- What are the mechanical properties of single crystal silicon at elevated temperatures? For what reason the silicon diaphragm deforms plastically during annealing at 1100°C?
- Is it possible to prevent the silicon diaphragm from elastic failure at high temperatures, and how? Because the permanent deformation will lead to output signal drift in the pressure sensor, the plastic deformation of the silicon diaphragm should be avoided or be under strict control.

1.3 *Project objective and thesis overview*

This project is to investigate the possibility of using silicon diaphragms in high temperature pressure sensors. Before this, we need to answer the questions in section 1.2 and have a clear understanding of the mechanical behaviour of micromachined silicon diaphragms at high temperatures. So the objectives of the research are set as follows:

- Understand the working principles of standard micromachined pressure sensors, and be aware of the technologies which extend the MEMS sensor to high temperature environment;
- Fundamentally understand the mechanical properties of single crystal silicon, and know the available mechanical testing methods for the characterization of single crystal silicon.
- Design a series of experiments to investigate the behaviour of micromachined silicon diaphragms with annealing time at a temperature above 600°C. Based on the experimental results, develop methods to prohibit the pressure sensing diaphragm from failing.
- Be able to predict the occurrence of plastic deformation for the test samples, and build a model to predict the amount of plastic deformation.

The remainder of the thesis is organized into six chapters. Chapter 2 presents the background information focusing on the state of current Silicon-diaphragm-based pressure sensors, outlining the technologies which extend MEMS sensor to harsh environment applications, and reviewing the characterization of silicon properties at high temperatures. Chapter 3 simulates the load-deflection behaviour of pressurized

silicon diaphragms, and predicts their elevated temperature behaviour. In chapter 4, the experimental procedures used to investigate the elevated temperature behaviour of micromachined silicon diaphragms are described in detail. Based on the evolution of the diaphragm deflections, the suggestions of designing a silicon diaphragm for high temperature applications are given. Chapter 5 presents a constitutive model for the plastic deformation of the micromachined silicon diaphragms at high temperatures. In chapter 6, the predicted results from chapter 3 and chapter 5 are compared with the experimental results, and the implementation of the mathematical models is discussed. Chapter 7 summarizes the research work and proposes the directions for future research.

List of References

[1-1] Mehregany M, Zorman CA, Rajan N and Wu CJ, Silicon carbide MEMS for harsh environments. P IEEE 1998; 86(8): 1594-1610

[1-2]Greenwood JC, Silicon in mechanical sensors. J Phys E: Sci Instrum 1988; 21: 1114-1128

[1-3] Shuwen Q, Eriksen H, Childress K, Fink A, and Hoffman M, High temperature high accuracy piezoresistive pressure sensor based on smart-cut soi. in Micro Electro Mechanical Systems, 2008. MEMS 2008. IEEE 21st International Conference on. 2008.

2 BACKGROUND

2.1 *Introduction*

This chapter presents the background related to the development of micromachined pressure sensors for high temperature applications. MEMS technology is introduced briefly and the new trends on MEMS devices are outlined. The material properties of single crystal silicon are then summarized and the current state of Si-based MEMS pressure sensors is reviewed. Then the achievements and the challenges in the development of MEMS pressure sensors for harsh environment are presented. Finally, the material testing methods which are used to characterize the mechanical properties of SCS are summarized, and the high temperature behaviour of SCS, especially yield strength and creep properties, are reviewed.

2.2 *Introduction to MEMS*

2.2.1 MEMS technology

Micro-Electro-Mechanical Systems (MEMS) is the integration of mechanical elements, sensors, actuators, and electronics on a common silicon substrate. The MEMS devices are in the size range from micrometer to millimetre. The process by

which the micromechanical components are manufactured is known as micromachining [2-1]. Micromachining technologies are generally divided into bulk micromachining in which parts of the substrate material are selectively etched away, and surface micromachining in which thin films are deposited on the substrate in order to form the intended structures. The electronics in MEMS systems are fabricated using integrated circuit (IC) process sequences, which are identical to those used in IC fabrication.

MEMS devices generally provide the advantages of reduced size, batch fabrication, low cost, low power and high precision. These advantages have lead to a growing number of applications of MEMS devices in a variety of industrial fields, for example:

- Airbag accelerometers, tyre pressure sensors, motion sensors and angular rate sensors for the automobile industry applications [2-2];
- DNA analysis system [2-3] and drug delivery system [2-4] for the health care industry;
- Microinertial reference system, microgyroscope and RF (radio frequency) communications system for the aerospace industry [2-5];

- Inkjet printer heads for the information technology industry [2-6];
- Micromirror array for the television industry [2-7].

The automotive industry is one of the major commercial markets for MEMS products since various kinds of sensors and actuators are being used in the vehicles in order to improve the fuel efficiency and the safety [2-2]. MEMS reliability is essential for space application because the devices should be able to operate under the extreme conditions [2-5].

2.2.2 Trend of MEMS technology

With the market needs for low cost high performance instruments and recent advances in micromachining technology, the next evolution of the microsystems will be the development of intelligent systems which are able to provide a number of functions, improved performance and low production cost [2-8]. Therefore, the future of MEMS lies in the integration of larger numbers of diverse components into systems of increasing complexity [2-9].

Meanwhile, the development of the microsystems for harsh environments has been a general trend in MEMS technology. Due to the increasing demand for precision measurements and electronic control using MEMS, microsensors and microactuators are required to operate in extreme conditions [2-10]. For example, in the oil industry, the accelerometers which are used for downhole drilling have to survive in the presence of high temperature and intense vibration. In the aerospace industry, the microsystems used in a spacecraft must operate in high radiation environment, and sometimes need to survive in extreme temperature conditions. Other harsh environments include corrosive media, extreme pressure, and/or strong shock. Much progress has been made to overcome the effects of the extreme conditions by the utilisation of new MEMS materials and technologies. However, more efforts are required to improve the reliability and the performance of the newly developed devices.

2.3 *Silicon-diaphragm-based pressure sensors*

The key components of silicon-diaphragm-based pressure sensors are shown in Figure 2- 1. The micromachined silicon diaphragms are widely used as pressure sensing elements. The pressure is determined by the resultant strain or the displacement of the

diaphragm due to applied pressure. According to the transduction mechanisms, the micromachined pressure sensors can be classified into capacitive, piezoresistive, and resonant sensors. By taking the advantage of MEMS technology, miniaturization and sophistication of the pressure sensor have been achieved. At the same time, by upgrading the standard micromachined sensors, the operation range of the silicon based sensors has been extended to moderate temperatures.

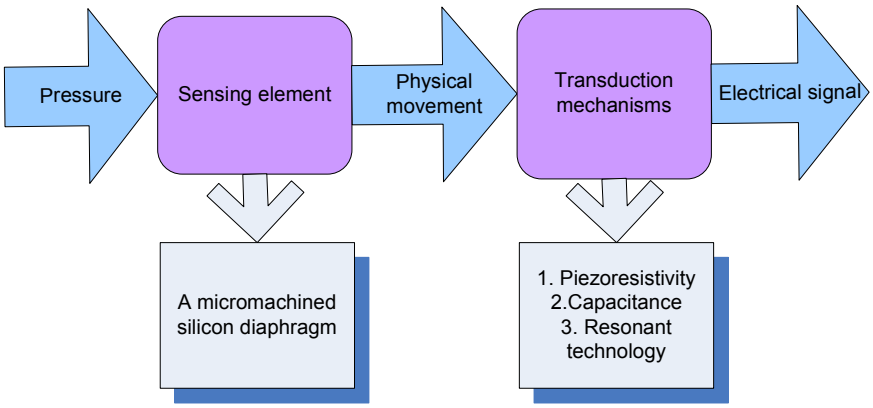

Figure 2- 1 Key components of silicon-diaphragm-based pressure sensors [2-11]

2.3.1 Silicon in mechanical sensors

Silicon is the most wildly used material for etched diaphragms and strain gauges in pressure sensors because of its excellent mechanical properties, high purity and crystalline perfection, and the advanced silicon micromachining technology [2-12]. Silicon has a high Young's modulus (190GPa), a high melting point (1400°C), a small thermal expansion coefficient (2.33×10^{-6}/°C), and a low density ($2.3 g/cm^3$) [2-13]. As

a result, the components made by silicon are able to work in the small deflection region under relative high load, and to operate at normal temperatures with good mechanical properties.

In addition, single crystal silicon is a brittle material with no plasticity or creep at normal temperatures. This characteristic makes the sensing devices free from signal drift or hysteresis. Since silicon fails by brittle fracture, high strength can be achieved by the optimized design of the structure and the careful application of the micromachining process. Silicon micromachining is based on photolithography and includes etching, doping and deposition of thin films. Therefore, silicon structures can be shaped easily with high precision. Silicon is therefore regarded as an excellent material for MEMS mechanical sensors.

However, silicon has its own limitations and disadvantages. Firstly, the elastic properties of single crystal silicon are orientation dependent. This makes the exact simulation of the mechanical behaviour very difficult for silicon structures with complex geometry. Secondly, the mechanical properties of silicon start to deteriorate above 500°C. At elevated temperatures, silicon becomes ductile and is susceptible to

creep. In addition, pure silicon sensors containing p-n junctions for electrical isolation (Piezoresistive sensors normally use p-n junctions to isolate the piezoresistive elements from the silicon substrate) can not be used at a temperature above 150°C due to the rising leakage current across the junctions [2- 14]. It is considered that conventional silicon-based electronics can not function above 250°C [2-15]. So it is necessary to use the packaging technology or a thermal isolation method to protect the electronics from the effects of high temperature.

2.3.2 Silicon-diaphragm-based capacitive pressure sensors

MEMS capacitive pressure sensors use a micromachined silicon diaphragm as one plate of a capacitor. As shown in Figure 2- 2(a), one side of the diaphragm is exposed to the external pressure, while the other side is exposed to a reference pressure. The changes of the pressure cause the diaphragm to deflect, and therefore change the capacitance of the capacitor. The capacitive pressure sensor exhibits high sensitivity to pressure, low power consumption and low temperature sensitivity. However, it is inherently non-linear because the capacitance is inversely proportional to the distance between the electrodes, and the range of operating pressure is limited.

Good linearity of a capacitive sensor can be achieved by operating in the contact mode [2-16]. As shown in Figure 2- 2(b), the pressure sensing diaphragm touches the substrate structure during operation. Because the thickness of the isolation layer is small and the dielectric constant of the isolation layer is large, the capacitance of the contacted area is much larger than that of the uncontacted area. At the same time, the capacitance of the contact area is nearly proportional to the applied pressure over a limited pressure range. So the output capacitance of the pressure sensor is nearly linear as a function of the applied pressure.

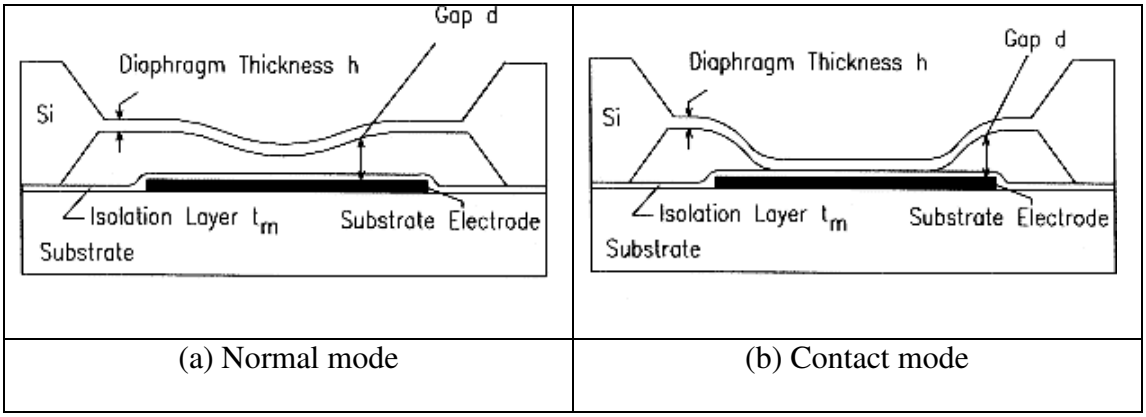

(a) Normal mode | (b) Contact mode

Figure 2- 2 Basic structure of a capacitive pressure sensor

(a) normal mode; (b) contact mode [2-16]

The large overload ability and robust structure make the touch mode capacitive sensor able to withstand a high pressure environment. Ko and Wang employed touch mode capacitive sensor in tyre pressure monitoring, as shown in Figure 2- 3. The silicon

substrate is used as bottom electrode. The gap is defined by the thickness of thermally grown oxide. The sensor chip consists of two capacitors. One is constructed by the silicon diaphragm and the substrate separated by a reference cavity. This capacitor is sensitive to pressure. The other is constructed by the silicon diaphragm and the substrate separated by the oxide in the rest of the bonding area. This capacitor is not sensitive to pressure and is used as a reference capacitor. This pressure sensor is able to measure the pressure up to 10^3psi (6.89MPa) with good temperature characteristics from 25°C to 100°C [2-16].

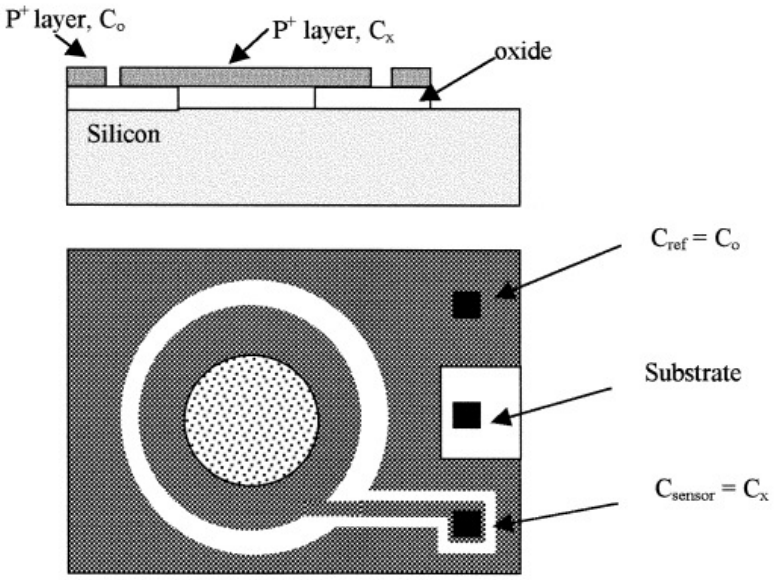

Figure 2- 3 structure of a touch mode capacitive pressure sensor [2-16]

Another way to increase the linearity is to use a bossed diaphragm as the sensing element. For example, the capacitive differential pressure sensor designed by Moe et

al. employed the bossed diaphragm in their membrane capacitor, as shown on top right side in Figure 2- 4 [2-17]. The differential pressure sensor is developed for the flow-rate measurement in hot petroleum wells. The reference capacitor on the top right side in Figure 2- 4 enables the pressure and temperature to be compensated. The ASIC (SMS-5) is used for signal read-out. The sensor was able to survive in the pressure range of 0-1000bar (0-100MPa) and the temperature range of 0-200°C.

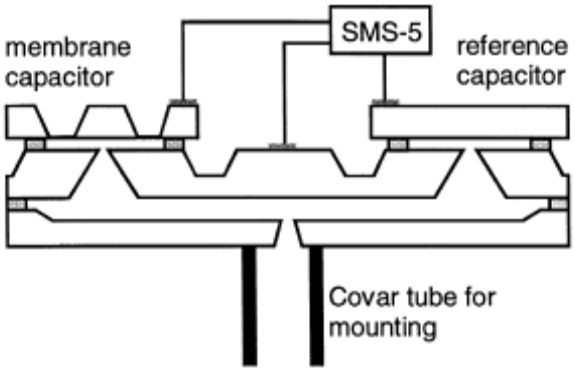

Figure 2- 4 Schematic cross section of the differential pressure element [2-17]

2.3.3 Silicon-diaphragm-based piezoresistive pressure sensor

The piezoresistive pressure sensor consists of a micromachined silicon diaphragm and a substrate, as shown in Figure 2- 5. The piezoresistive strain gauges are diffused or implanted into the pressure sensing diaphragm. The deformation of the diaphragm under pressure causes a change in the structure of the piezoresistors, this leads to a change in the resistivity of the material. The pressure sensor normally has four

piezoresistors connected in a Wheatstone bridge configuration (as shown in Figure 2-5) in order to convert the resistance into a voltage output [2-18]. Because the piezoresistors are highly sensitive to the changes of the operating temperature, the use of temperature compensation techniques is necessary.

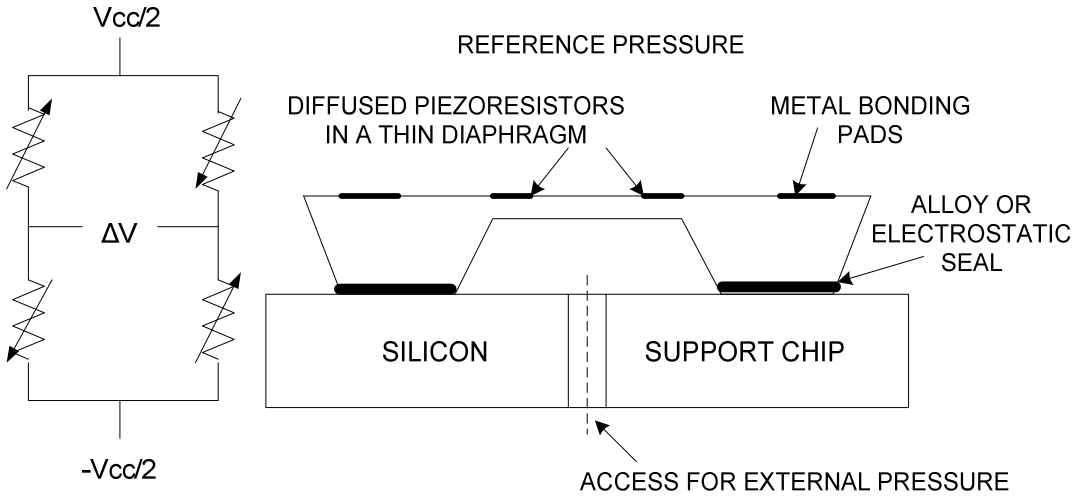

Figure 2- 5 Full bridge piezoresistive pressure sensing structure [2-18]

The sensitivity of the piezoresistive pressure sensor is mainly influenced by the diaphragm thickness and the diaphragm alignment [2-18]. When the diaphragm is subjected to a high pressure (for example, 100MPa), the deflection may be so large that the output voltage is not linear to the applied pressure any more. Aravamudhan and Bhansali employed double bulk-micromachined diaphragms in the piezoresistive sensor in order to reduce the non-linearity effect [2-19]. As shown in Figure 2- 6, the

inner diaphragm is thinner while the outer diaphragm is thicker. When operating under lower pressures, the inner diaphragm deflects and the outer remains insensitive. At higher pressures, inner diaphragm is in tension and change of resistance in the outer diaphragm is measured. In order to compensate for temperature variations, the piezoresistors are in the form of the Wheatstone bridge configuration. This reinforced sensor is capable of operating up to 703m of water (6.89MPa) with higher sensitivity and wider operating pressure capability compared to the conventional single diaphragm sensor.

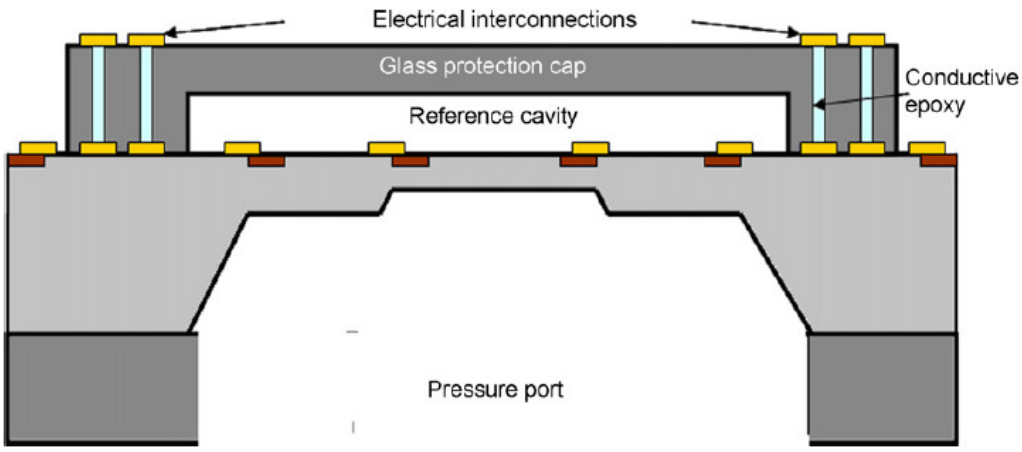

Figure 2- 6 Packaging scheme for the reinforced piezoresistive pressure sensor [2-19]

2.3.4 Silicon-diaphragm-based resonant pressure sensor

Resonant pressure sensors are typically based on a vibrating structure coupled to a micromachined silicon diaphragm. The diaphragm deforms under applied pressure,

and the resultant tension in the vibrating structure changes its resonant frequency. There are three basic resonant structures: the beam, the bridge and the diaphragm. A block diagram of a typical resonant sensor is shown in Figure 2- 7. A resonant sensor comprises four parts: the vibrating structure, the excitation unit, the detection unit and the feedback circuitry [2-20]. The excitation unit excites the vibrating structure into resonance, and the detection unit senses the vibrations. Normally, there are six main types of excitation and detection techniques, including electrostatic excitation and capacitive detection, dielectric excitation and detection, piezoelectric excitation and detection, resistive heating excitation and piezoresistive detection, optical heating and detection, magnetic excitation and detection [2-21]. It is also important to note that the output signal of a resonant sensor is in the frequency domain [2-22]. Therefore, the interface to a digital system can be simplified. The output signal should feedback via an amplifier to the excitation unit, to ensure that the structure can be maintained at resonance over the entire measured range.

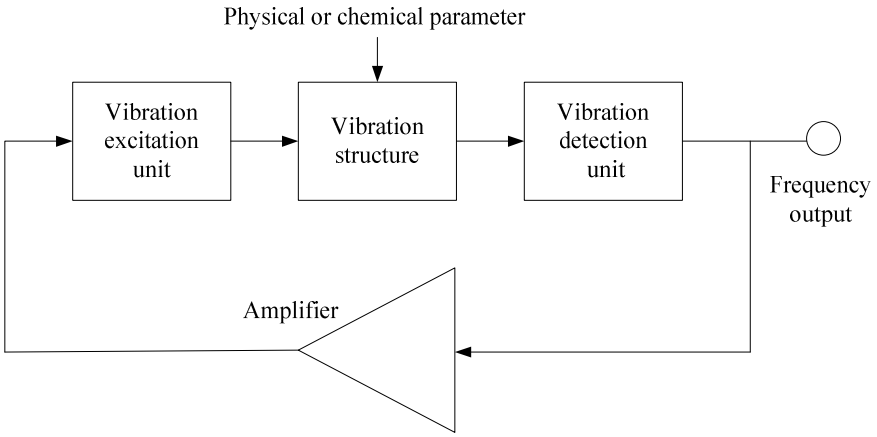

Figure 2- 7 A block diagram of a typical resonant sensor [2-20]

One of the main resonator characteristics is Quality factor (Q-factor). The Q-factor is defined as a ratio of the total energy stored in the structure to the total energy lost from the vibrating structure per cycle [2-23]. For a general device, the Q-factor is limited by several damping mechanisms: the damping from a surrounding fluid, Q_a; the damping due to imbalance, Q_s; and damping resulting from internal material related losses, Q_i. These Q-factors can be related to the total Q-factor as: $1/Q = 1/Q_a + 1/Q_s + 1/Q_i$ [2-24]. A high Q-factor is always wanted in a resonant sensor [2-25]. Firstly, it will enhance the desired resonant vibration, while suppressing the nonresonant vibrations. This enables the resonance frequency to be clear and easily distinguished. Secondly, it will improve the performance and resolution of the resonator. Thirdly, it will give a high accuracy and long-term stability.

The first silicon resonant pressure sensor was developed by Greenwood [2-26]. This sensor applied a butterfly-shape resonator (as shown in Figure 2- 8) on a silicon diaphragm and used electrostatic excitation and capacitive detection mechanism. The shape of the resonator and the diaphragm were defined by boron doping, and were etched from a single piece of silicon using anisotropic etching techniques. The resonator has a Q-factor of approximately 10,000 in a vacuum better than 0.133Pa.

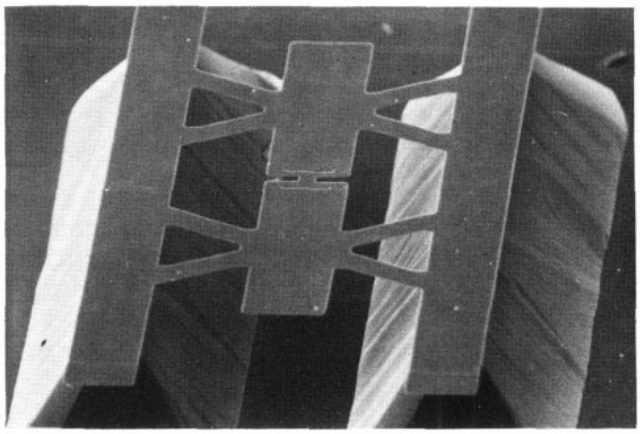

Figure 2- 8 SEM view of the butterfly-shape resonator [2-26]

The advantages of silicon as the resonator material are very high intrinsic Q-factors and high repeatability [2-20]. Compared to pure piezoresistive sensors, the resonant pressure sensors exhibit a better sensitivity overall but a lower temperature sensitivity. In addition, the output signal frequency has low noise level and can be interfaced with digital electronics easily. However, the structure of the resonator can be very

complex, and the coupling between the excitation and detection mechanism is a technical challenge.

2.4 *Micromachined pressure sensors for harsh environment*

The MEMS pressure sensors which are able to operate at high temperatures are in great demand by the automotive and aerospace industries. The pressure sensors should operate up to 450°C for diesel engines, or around 650°C for turbine engines [2-27]. In order to extend MEMS sensor to harsh environment applications, silicon carbide (SiC) or silicon on insulator (SOI) technology has been employed in high temperature pressure sensors.

2.4.1 SiC based pressure sensors

Silicon carbide (SiC) is an attractive material for MEMS devices in harsh environments because of its superior properties including high modulus, high fracture strength, corrosion resistance, radiation resistance, mechanical stability and stable electronic properties at elevated temperatures, and its compatibility with existing Si processing techniques [2-15]. Ned et al. reported the performance of a full 6H-SiC piezoresistive pressure sensor based on batch fabrication process from room

temperature up to 600°C [2-28]. Wu et al. developed a pressure sensor using electrically isolated 3C-SiC piezoresistors on silicon substrate [2-29]. Its performance was tested up to a temperature of 385°C. It is found that at elevated temperatures, the SiC piezoresistors do not suffer from the junction leakage, and there is no plastic deformation of the SiC diaphragm. For both sensors, the output voltages are almost linear as a function of the applied pressure at a given temperature. However, it is shown that both sensors exhibit strong temperature dependence because the resistance varies with the increasing temperature. Therefore, it is necessary to implement the high temperature compensation scheme in the devices.

Young et al. developed a 3C-SiC capacitive pressure sensor which demonstrated a high-temperature sensing capability up to 400°C [2-30]. This sensor uses a 3C-SiC diaphragm as the pressure sensing element and operates in contact mode. The results show that the device exhibits separate responses at different temperatures due to the trapped air between the plates. It is suggested that this temperature dependent effect can be minimized by the wafer bonding process in vacuum. However, the device is expected to have thermal drift because of the mismatch of the thermal expansion coefficient between the SiC and the silicon substrate.

The superior properties of silicon carbide allow the SiC based pressure sensors to operate at very high temperature (>500°C). However, the micro-fabrication processes for SiC is far less mature than silicon based micromachining processes. The cost for SiC sensors is much higher than that of silicon micromachined sensors.

2.4.2 SiC coated pressure sensors

It is necessary to mention here that SiC coating of standard Si MEMS structure is an effective approach for MEMS sensors that need to operate in corrosive environment and at moderate temperatures (below 300°C) [2-31]. Silicon carbide can be deposited by chemical vapour deposition (CVD) techniques. The coated SiC film functions as passivation layer on top of sensors and enables normal Si-based pressure sensors to operate in harsh environments.

The poly-SiC coated poly-Si DETF (double-ended tuning fork) resonant strain sensor developed by Azevedo et al. shows resistance to KOH etching with the operating temperature up to 190°C in air [2-31]. By optimizing the deposition thickness of the SiC coating, the strain resolution was maintained at the level which is comparable to the uncoated device performance. Zhang et al. used a PECVD (plasma-enhanced

chemical vapour deposition) silicon carbide thin film to protect a piezoresistive pressure sensor from an erosion environment [2-32].

The SiC coated Si devices are more cost effective than full SiC devices, and demonstrate better performance in harsh environments than traditional Si devices. However, there might be large residual stress in the coated SiC film due to the mismatch in lattice parameter and thermal expansion between the SiC film and the Si substrate [2-33]. The deposition process needs to be optimized to improve the coating uniformity and to minimize the residual stress.

2.4.3 SOI based pressure sensors

The SOI (Silicon On Insulator) technology is an attractive approach to build the piezoresistive pressure sensors for high temperatures. The traditional silicon-based piezoresistive sensors use p-n junctions for electrical isolation. Therefore, the application temperature is limited to 150°C due to the junction leakage. The SOI wafer contains an oxide layer between the device layer and the silicon substrate. The SOI based piezoresistive sensors use the buried oxide layer to isolate the

piezoresistors from the substrate and from each other. Thus, the upper limit of the temperature range can be extended.

One example is the high temperature piezoresistive pressure sensor developed by Guo et al. [2-34]. The ultra-thin silicon films (less than 0.5μm) of SOI are used as the pressure sensing element. As shown in Figure 2- 9(a), the sensor has four pressure sensing resistors in Wheatstone bridge configuration. The resistors are located on the edge of the square diaphragm. In order to prevent the elastic failure of the diaphragm, its dimensions are chosen carefully so that the maximum stress induced by the highest operating pressure (103.4MPa) is well below the yield strength of silicon at the highest operating temperature. In addition, a capping wafer is attached to the device wafer in order to form a reference pressure chamber, as shown in Figure 2- 9(b). A temperature sensor is used to measure the temperature of the pressure sensor in order to compensate for the temperature variations. The packaged sensor is able to measure over the pressure range from 16psi to 600psi (0.110MPa to 4.136MPa) and in the temperature range from -55°C to 500°C. The low pressure hysteresis at 500°C indicates that the designed silicon diaphragm is capable of operating at high temperature without creep or plastic deformation.

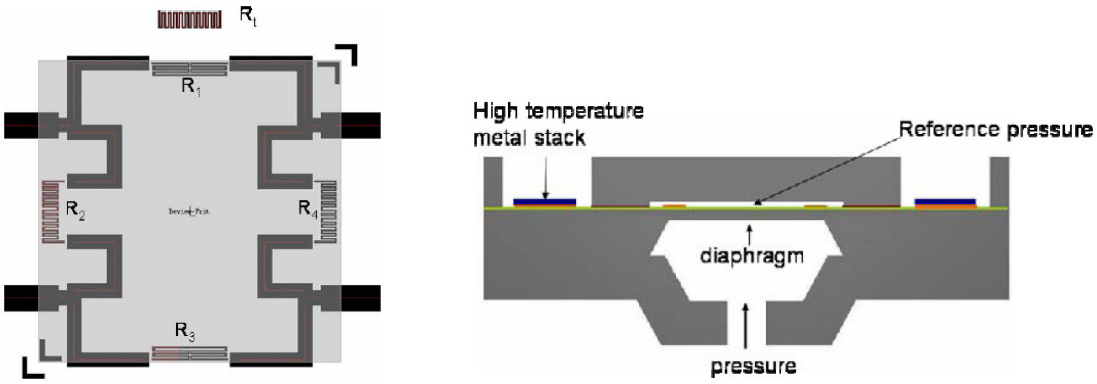

(a) (b)

Figure 2- 9 A piezoresistive pressure sensor (a) a top view; (b) a cross section view [2-34]

Zhao et al. developed a novel piezoresistive pressure sensor based on SOI technology [2-35]. The strain gauge is etched in the device layer by means of RIE (reactive-ion etching), and a layer of silicon-nitride is deposited to protect the silicon gauge. The sensor is capable of operating up to 200°C.

The SOI technology is compatible with the standard silicon micromachining process. High quality SOI wafers are now commercially available. However, the application of SOI technology in harsh environments is limited. Firstly, the silicon surface is not stable in aggressive media, such as KOH solutions. Secondly, single crystal silicon is susceptible to creep at temperatures above 500°C [2-27].

2.5 *Material characterization of single crystal silicon*

The mechanical behaviour of the structures is related to the properties of the material from which the structures are made. So the mechanical testing methods are summarized especially for the characterization of single crystal silicon. The probable failure modes associated with the silicon-based high pressure temperature sensors are plastic deformation or creep. In order to prevent silicon structure from failing, the characterization of the yield strength and the creep properties for single crystal silicon is important. Previous investigations and measurement methods are reviewed in the first instance.

2.5.1 Mechanical testing methods

For micromachined silicon structures, the mechanical properties of silicon may relate to the fabrication routes [2-36]. The fabrication routes of silicon include surface micromachining and bulk micromachining. Surface micromachined devices consist of thin deposited layers, while bulk micromachined structures are created from bulk material by etching processes. The mechanical properties of the deposited silicon layers can be different from those of the bulk silicon.

At the same time, some properties of silicon, such as fracture strength, are dependent on the scale [2-36]. The strength of the brittle material is governed by the maximum size of the flaws which are presented at the surface or inside the structure. The larger the flaw size, the lower the fracture strength. When the scales of the micromachined structures decrease to the range from 0.1μm to 10mm, the range of the flaw size reduces sequentially. Therefore, the mechanical elements at small scales are inherently stronger than the macroscale structures.

As a result, the mechanical characterization of micromachined material is very important for the design and fabrication of the MEMS devices. The mechanical properties such as strength, fatigue, creep, internal stress and Young's modulus have been investigated by a number of researchers. This section focuses on the mechanical testing methods used in the characterization for single crystal silicon including bending, tensile, membrane and bulge.

The beam bending test and the direct tension test are two of the popular methods to study the Young's modulus, yield strength and fracture strength of the micromachined cantilevers or beams. The experimental setup for bending test is simple. The method

needs a relatively small force to yield a lateral deformation which is large enough to be tested. However, the interpretation of the experimental data is not straightforward.

The tension test is the most effective and direct way to obtain the testing results, but the method is not easy to use. Firstly, for small samples it is a challenge to apply a tensile load in the direction of the sample. The results can be affected by the slight misalignments. Secondly, it is difficult to measure the magnitude of the sample elongation since it is very small. Nakao et al. evaluated the fracture toughness of the SCS film by on-chip tensile test [2-37]. The load was applied by a double cantilever beam spring and the displacement was measured by a capacitive sensor. In addition, the testing system consists of a heating stage which enables the researcher to perform the test at high temperatures up to 500°C.

Other testing methods such as the membrane bulge test and resonant test have been applied to single crystal silicon as well. Bonnotte et al. studied the elastic properties of thin silicon membranes by bulging tests [2-38]. The displacement of the pressurized membrane is recorded as a function of the applied pressure using interferometry. The test is easy to perform, and the silicon micromachining techniques are suitable for the

creation of the membrane structures. Schindel. et al. investigated the temperature dependence of Young's modulus for silicon from 20°C to 700°C using the miniaturized silicon tuning forks [2- 39]. Its resonant vibration is measured by noncontact capacitive transducers. It was confirmed again that the Young's modulus decreases with increasing temperature.

2.5.2 Yield strength characterization of SCS

2.5.2.1 Yield strength of bulk silicon

Single crystal silicon increasingly becomes ductile above about 500°C. Samuel and Roberts studied the brittle-to-ductile transition (BDT) temperature by conventional four-point bending test [2-40]. It was observed that silicon deformed by macroscopic plastic yielding at temperatures above the transition temperature, while it fractured in a completely brittle manner below the transition. The variation of the transition temperature depends on the strain rate and the electronic doping. An increase in strain rate caused an increase in the transition temperature. The transition temperature for intrinsic silicon with very slow loading rate is about 560°C. The heavy boron doping ($2\times10^{18}/cm^3$) was found to reduce the transition temperature by about 30°C. This is

because the presence of the impurity decreases the activation energy for the dislocation motion.

Patel and Chaudburi studied the yield strength in silicon by conventional tensile test [2-41]. The stress-strain curves are sensitive to the initial dislocation density, the temperature and the strain rate. The maximum stresses reached during yield decreases with the increase of the initial dislocation density, as shown in Figure 2- 10(a). The yield stress and the flow stress for dislocation-free silicon is shown in Figure 2- 10(b). It can be seen that with increasing temperatures, the yield stress decreases because of the increased mobility of dislocations in crystal silicon. The pronounced strain rate dependence of the yield stress is a result of the relatively small stress dependence of the dislocation velocities. An increase in stress causes a small change in dislocation velocity, thus accommodating a small strain rate. In order to accommodate a higher strain rate, the dislocation velocity must increase significantly (the change in strain rate has little effect on the dislocation density), resulting in a dramatic increase of the yield stress.

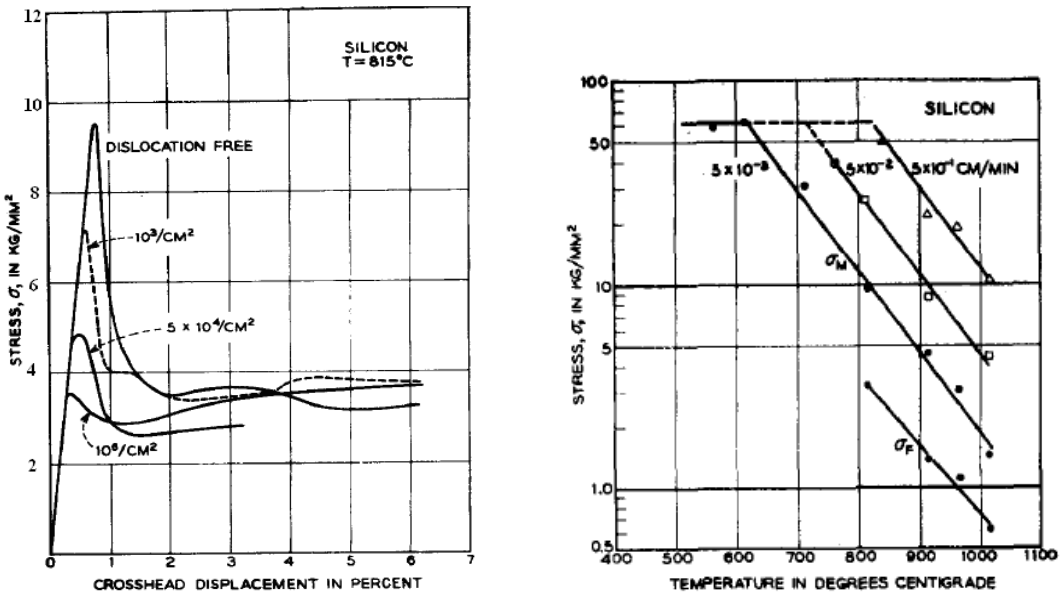

(a) (b)

Figure 2- 10 (a) Influence of initial dislocation density on the stress-strain curve at 815°C; (b) Temperature and strain rate dependence of yield stress σ_M and flow stress σ_F for dislocation-free silicon (1kg/mm^2= 10MPa) [2-41]

The yield deformation of silicon was also studied by Pearson et al. using bending test [2-42], and by Sumino using the tensile test [2-43]. The experiments revealed the effect of the temperature, strain rate and the dislocation density on the yield behaviour of silicon crystals. The results provide very useful reference values of the yield strength for various conditions.

2.5.2.2 Yield strength of micromachined SCS

The study for the plastic deformation of silicon microstructures is reviewed as follows.

Huff et al. applied bulge test to pressurized micromachined cavities and also developed an analytical model to predict the amount of plastic deformation [2-44]. The fabrication process of the microstructure and the plastic deformation after high-temperature exposure are shown in Figure 2- 11. The sealed cavities were made by bonding an etched silicon wafer to a second silicon wafer. The second wafer was then etched in KOH etchant in order to thin the cap layer to a thickness of 55 microns. The residual pressure inside the cavity is about 0.8atm (81kPa). The structures were then exposed to a high temperature environment for a period of 1 hour. Due to the expanding residual gases within the sealed cavity and the reduced yield strength of silicon at high temperatures, the silicon capping layer deforms plastically. The permanent deformation was observed after cooling and the maximum amount of deformation was measured by an optical microscope. As shown in Figure 2- 12, the resultant height of the capping layer is from 10 to 30 microns with the temperatures ranging from 900°C to 1150°C. The occurrence of the plastic deformation has been

predicted by comparing experimental values of the yield strength with the calculated maximum stress in the capping layer of silicon due to the expanding heated gases within the sealed cavity.

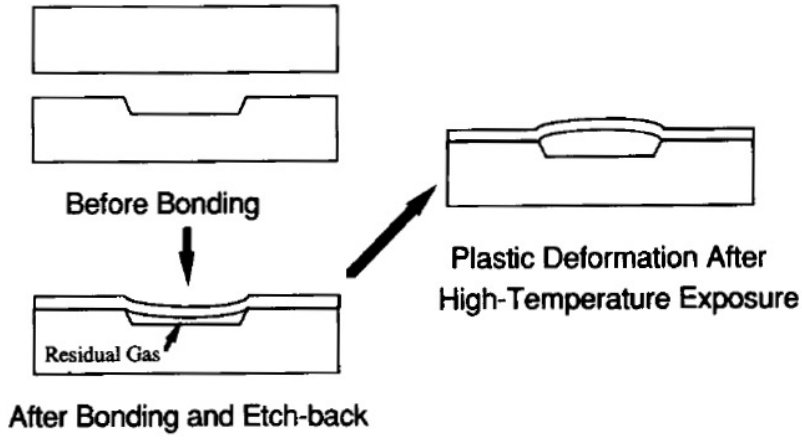

Figure 2- 11 Silicon wafer bonding resulting in residual gas pressure inside the sealed cavities and plastic deformation after high-temperature exposure [2-44]

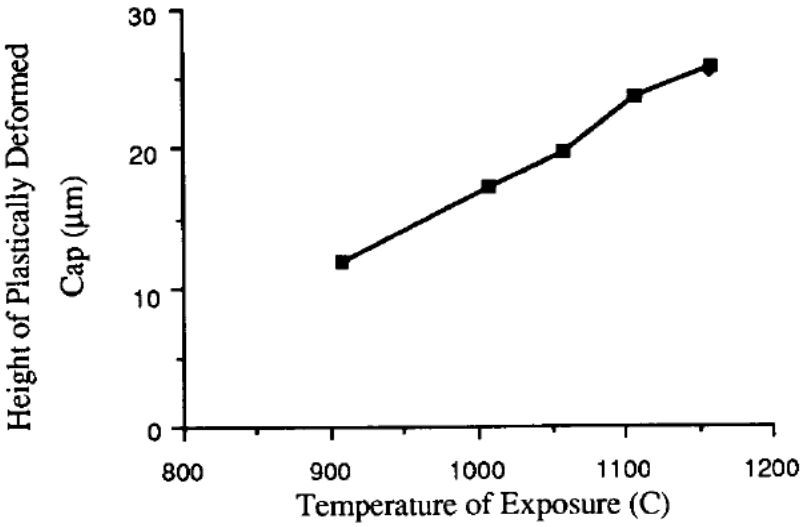

Figure 2- 12 Measured heights of plastically deformed capping layer of silicon [2-44]

Frühauf et al. carried out 3-point bending tests on silicon beams in order to characterize the plastic behaviour of the silicon microelements (Figure 2- 13) [2-45]. The structure was created by the combination of wet anisotropic etching and plastic deformation at high temperatures. The tests were performed at the temperatures of 700°C, 800°C, 900°C and 1000°C with the bending rates of 0.1mm/min, 0.3mm/min, 1.0mm/min, 3.0mm/min and 5.0mm/min. The yield point values of the upper and lower yield points are listed in Table 2- 1. The values of the <100> orientated beams are lower than those of the <110> orientated beams. This is because there are eight slip systems in the <100> orientated material while there are only such four systems in the <110> orientated beams. The different number of working glide systems generates a different number of dislocations, and thus leads to the difference of the upper yield-point values.

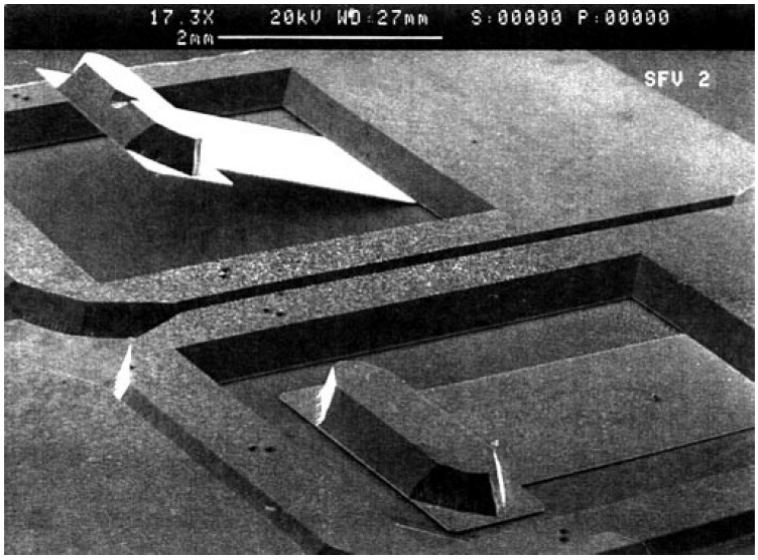

Figure 2- 13 Plastically deformed bending spring with mass (an undeformed element is shown in the foreground) [2-45]

Table 2- 1 Yield point values of differently orientated beams (deformation rate: 0.1mm/min) [2-45]

Deformation temperature /°C	700	800	900	1000
⟨100⟩lower yield point /MPa	153.9	70.4	38.3	23.2
⟨100⟩upper yield point /MPa	309.3	142.8	71.1	38.9
⟨110⟩lower yield point /MPa	163.7	77.3	41.3	26.0
⟨110⟩upper yield point /MPa	364.6	174.5	81.6	71.1

Namazu et al. studied the elastic-plastic properties of nanometric single crystal silicon (SCS) wires by bending tests with an atomic force microscope (AFM) [2-46]. The SCS wires with widths from 200nm to 800nm were fabricated by means of

anisotropic wet etching. Figure 2- 14(a) shows the SEM photograph of the 200-nm-wide wires. The schematic diagram of the bending test is illustrated in Figure 2- 14 (b). The wires were fixed at both ends. They were bent to failure by a diamond tip. The bending force and the maximum displacement were calculated from the differential voltage detected by a built-in laser reflection technique of the AFM.

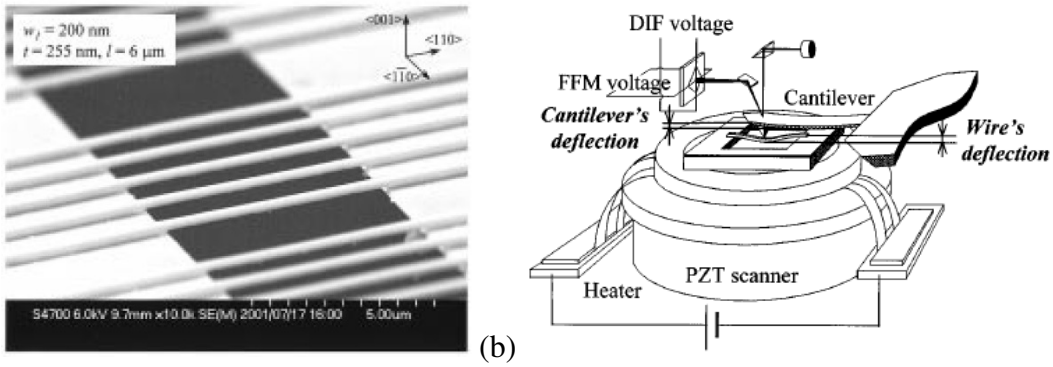

(a) (b)

Figure 2- 14 (a) SEM photograph of 200-nm-wide SCS wires, (b) Schematic of bending test with AFM at intermediate temperatures. [2-46]

The mechanical behaviour is not only influenced by the temperature, but also affected by the specimen size (Figure 2- 15). The critical resolved shear stress decreases with the increasing wire size. The SCS wires with the width of 200nm, 300nm and 550nm began to show plastic behaviour at 373K, which is much lower than the brittle-to-ductile transition temperature in bulk silicon. This is because the yield stress of deformed SCS wires (range from 4.2GPa to 7.2GPa) is high enough to move the

dislocations. Hence a large thermal energy which is essential to activate the dislocation motion in bulk SCS is not necessary for SCS on a nanometre scale.

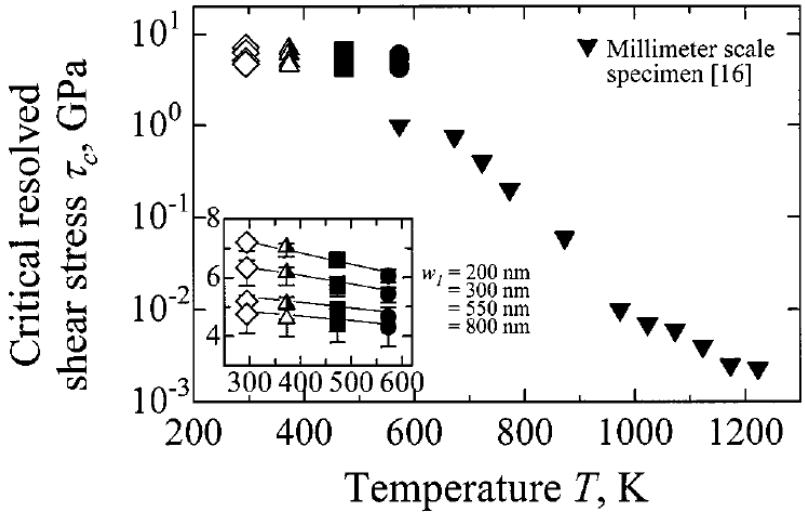

Figure 2- 15 Relationship between critical resolved shear stress and temperature at each wire size [2-46]

The mechanical properties of a micron-sized SCS film were investigated by Nakao et al. using an 'on-chip' tensile test [2-47]. The specimen along with a loading system is shown in Figure 2- 16(a). The straight portion of the specimen is 50μm or 100μm long, 4μm wide and 4μm thick. The specimen profile was formed by dry etching and the tensile axis is aligned to the <110> direction. The loading system consists of torsion bars, a load lever and a support frame. When a load is applied to the load lever, the lever rotates around the axis of the torsion bars, leading to stretching of the specimen.

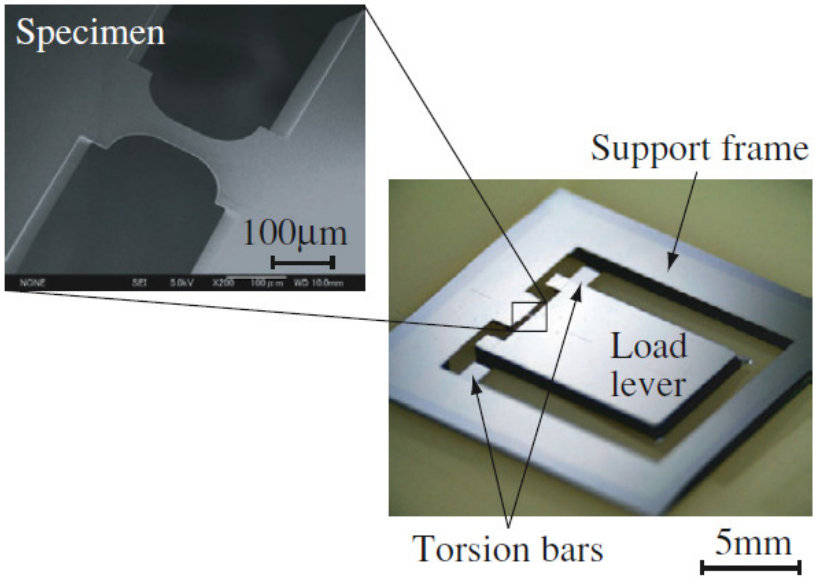

Figure 2- 16 'On-chip' tensile test device [2-47]

Figure 2- 17 plots the stress-strain relationship obtained from the tensile test at elevated temperatures. At room temperature (RT) and 300°C, the specimens deformed in an elastic manner, and the stress is linear to the strain until the specimen fractured (Figure 2- 17(a) and (b)). At 400°C and 500°C, the specimens showed ductility, and the stress-strain curves exhibited non-linear property under high stress (Figure 2- 17(c) and (d)). Therefore, for micron-sized SCS samples, it is possible to show ductile behaviour even at 400°C.

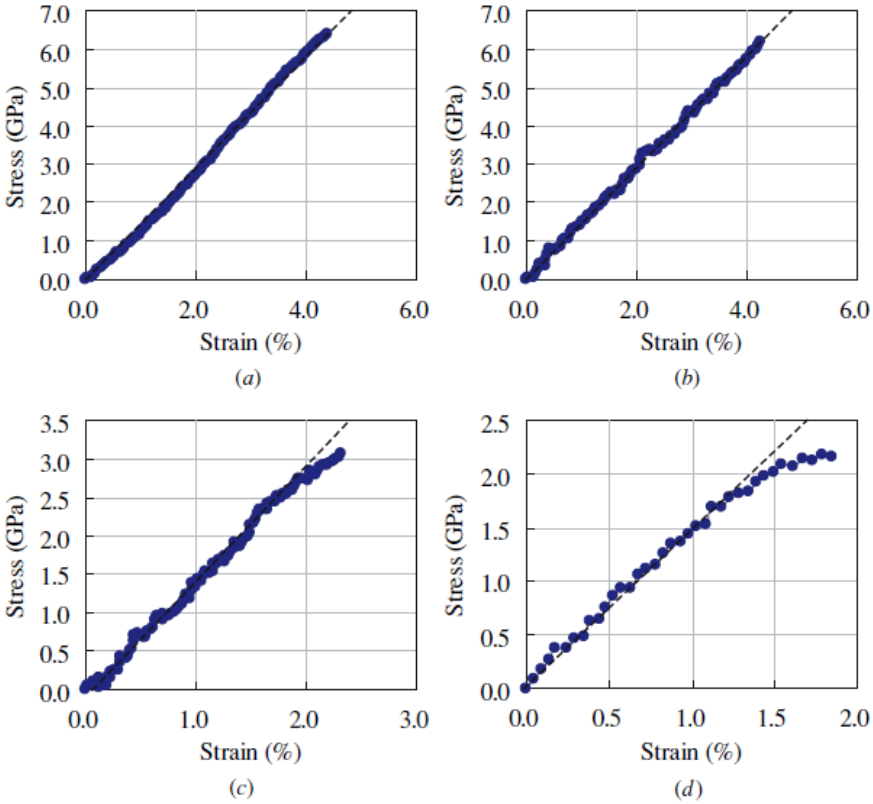

Figure 2- 17 Stress-strain relationship at (a) RT, (b) 300°C, (c) 400°C, (d) 500°C [2-47]

2.5.3 Creep characterization of SCS

Creep is the continued slow straining of a material under the influence of a constant load [2-48]. In silicon, creep deformation occurs at a temperature higher than half of the absolute melting point T_m (=1685K). The continuous deformation will result in unacceptable dimensional changes or creep rupture of the component. When a silicon micromachined sensor is considered, prolonged exposure to elevated temperatures can lead to the shift of the output signals, and probably detrimental tertiary creep with

catastrophic failure of sensing element. Therefore, creep plays a key role in the sensor lifetime and needs a serious investigation.

The creep test is usually carried out under constant load. The elongation of the specimen is measured against time in order to obtain the creep curve. A typical creep curve indicates three stages of creep deformation: primary creep, steady-state creep and tertiary creep (as illustrated by Figure 2- 18) [2-49]. In the primary stage, the rate of creep strain is relatively high, but slows down with increasing time. The strain rate reached its minimum value and become near constant in the secondary stage. In tertiary stage, the creep rate increases rapidly and leads to failure. For a given load, the higher the temperature, the steeper the creep curve is, and the faster the material will creep.

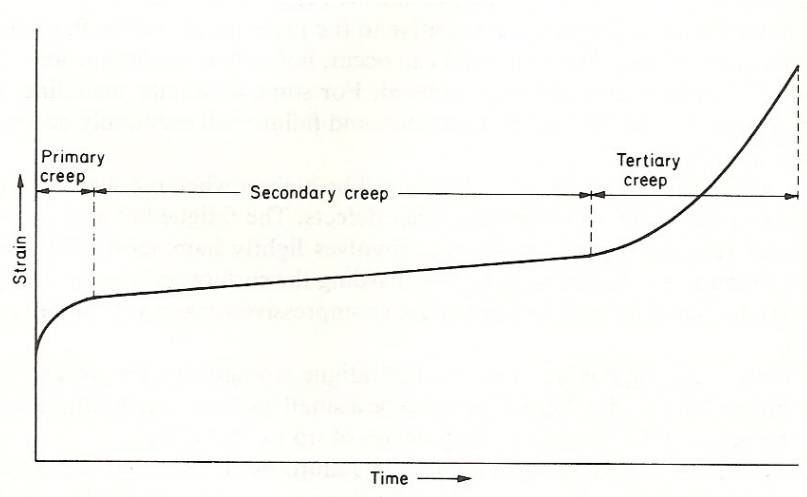

Figure 2- 18 A typical creep curve [2-49]

Creep properties for Si have previously been investigated in several studies. Reppich and Haasen studied creep deformation of single crystal silicon under uniaxial compressive loading [2-50]. Creep curves were obtained in the stress range of 1MPa to 20MPa at 750 ºC to 1050 ºC.

Myshlyaev et al. carried out the creep tests under uniaxial compression within the temperature range from 900ºC to 1300ºC at stresses from 19.6MPa to 147.1MPa [2-51]. The experimental data showed that the shape of creep curves is related to the applied stress, as shown in Figure 2- 19. At a low stress of 19.6MPa, the primary part of the creep curve exhibits a gradual strain rate increase (curve 1) followed by a steady creep stage (curve 2) which occupies the main portion of the test time. The extent of the creep stages decreases with increasing stress and temperature. At a high stress of 98MPa, the creep curves of silicon became similar to those of metals: the specimens deformed instantaneously under applied stress, and then the creep strain steadily reduced to a constant rate, and then increases rapidly until the rupture of specimens occurred. The stationary creep rate at stresses up to 98MPa is governed by the kinetic equation

$$\dot{\varepsilon} = 10^{11} s^{-1} \exp\left(-\frac{5.6eV - 2.7\times 10^{-21} cm^3 \sigma}{kT}\right)$$

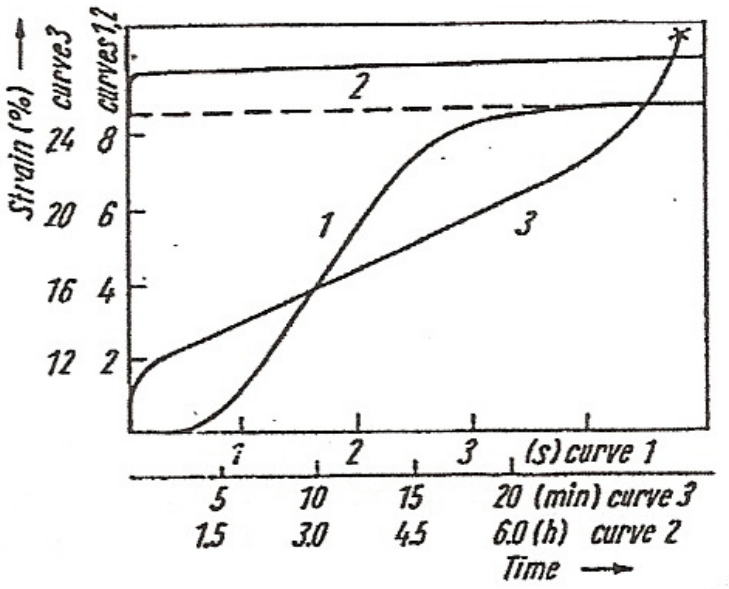

Figure 2- 19 Creep curves of silicon single crystals. Temperture 1100°C , stress 19.6MPa (curve 1 and 2, curve 1 represents the early creep stages) and 98MPa (curve 3). Point × indicates the rupture [2-51]

Taylor and Barrett investigated the plastic deformation of silicon which occurs at the early stages of creep behaviour [2-52]. Data was obtained at temperatures from 850ºC to 1200ºC. The applied stress in this case is quite low, ranging from 1.38MPa to 8.27MPa. The specimens were oriented in the way that shear stress in the $(\bar{1}11)$ $[01\bar{1}]$ slip system is maximum when the uniaxial compressive load is applied. And because the strain is kept low, only this slip system (mentioned above) is operative. So the authors assumed that it is the dislocation glide that controls the creep rate. The logarithmic creep was observed below about 1000°C. The creep curve obtained at 865°C is shown in Figure 2- 20. It can be seen that the ratio of creep strain over log

time increases with increasing stress. The creep strain at 865°C can be represented by equation

$$\gamma = \alpha \ln(\upsilon t + 1)$$

where α and υ are 10^{-3} and $2.5 min^{-1}$, respectively. Above about 1000°C, the steady state creep was observed with the activation energy of about 39kcal/mole.

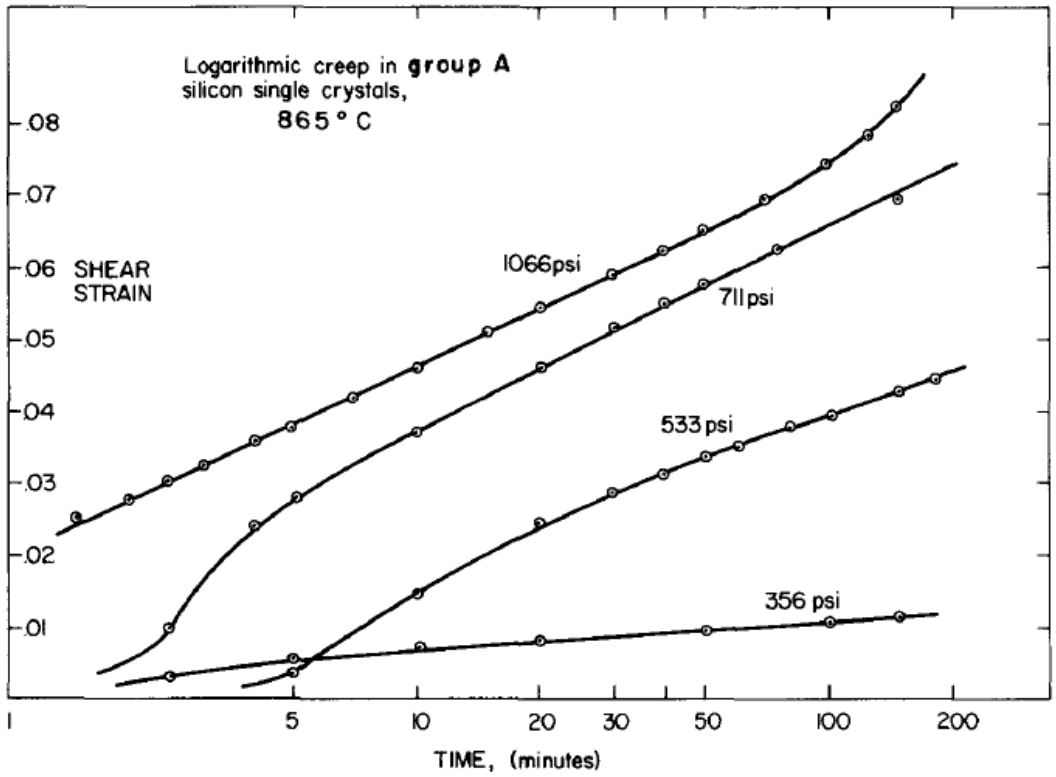

Figure 2- 20 Creep strain v. log time for single crystal silicon tested at 865°C (356 psi= 2.4MPa, 533 psi=3.7MPa, 711 psi=4.9MPa, 1066psi=7.3MPa) [2-52]

In order to optimize the design of the micro-engine, Walters and Spearing performed creep experiment on single-crystal silicon in four-point bending test [2-53]. Compared

with the compressive tests, this configuration avoids the problems of gripping and buckling of the specimen [2-54]. The maximum strain is only dependent on the load-point deflections. Therefore, the experiment is easily conducted. The tests were run at temperatures between 600ºC and 850ºC for a given bending stress ranging from 50MPa to 202MPa. The creep rate was found to be governed by Arrhenius's law:

$$\dot{\varepsilon} = A\sigma^{n} \exp\left(-\frac{Q}{RT}\right)$$

where the activation energy Q is found to be 224kJ/mol. A typical displacement-time curve obtained at 973K with the constant load of 45N is shown in Figure 2- 21(a). The load was increased from 0N at about 80s after the data acquisition, and was held at 45N from 125s to 730s. The creep curve showed a pronounced primary regime and a steady state regime. The micrograph of the side of the specimen around the inner load point is shown in Figure 2- 21(b). The slip bands appeared as dark lines after the specimen was polished and etched in a strong oxidizing acid solution. It can be seen that the slip bands are orientated parallel to the <111> directions and are dense at the loading point.

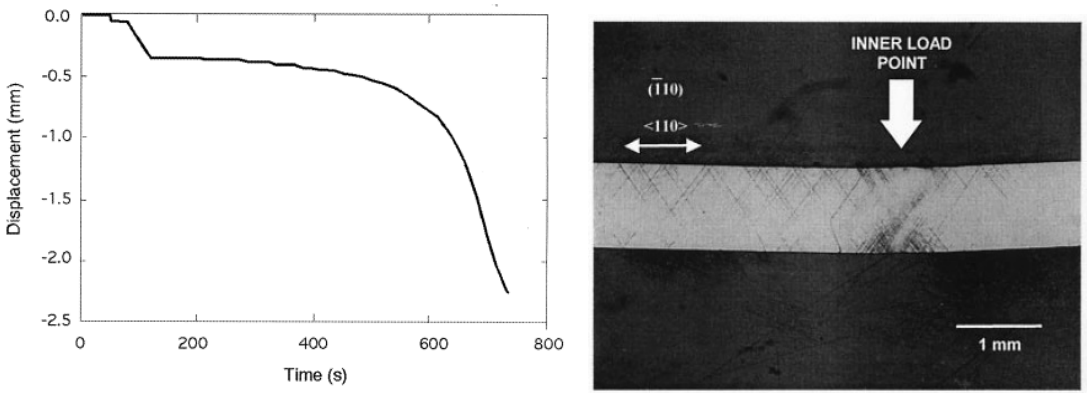

(a) (b)

Figure 2- 21 (a) A typical displacement-time data (973K, 45N); (b) SEM micrograph of a deformed specimen (The dark lines are slip bands as revealed by etching) [2-53]

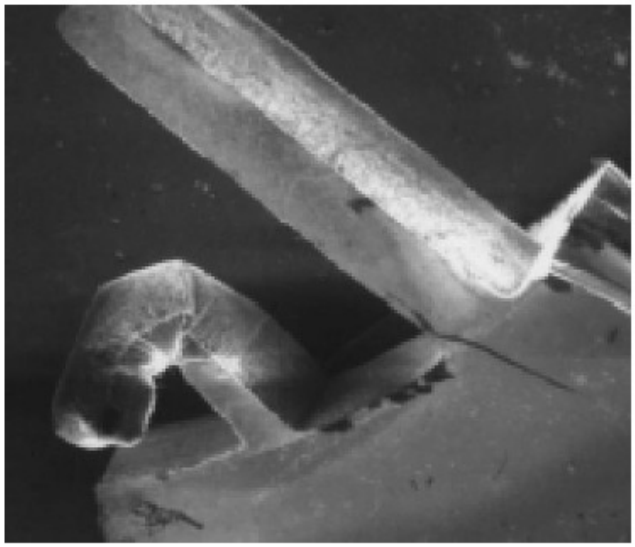

Figure 2- 22 SEM of the fingers of the combustor plate after combustion (the left finger shows the creep failure) [2-55]

From the literature review, it can be seen that bulk silicon structures which are working in conditions of high stresses and elevated temperature are prone to creep.

Creep of silicon has also been observed in the finger-like structures of a micromachined combustor, as shown in Figure 2- 22 [2-55]. However, the creep effect in real MEMS structures has seldom been studied. Therefore, the creep characterization of micromachined silicon components is necessary.

2.6 *Conclusions*

MEMS pressure sensors which can operate in harsh environment are increasingly demanded by the industries. Traditional MEMS sensors employ silicon diaphragms as the sensing element. The excellent properties of SCS guarantee the proper performance of the micromachined pressure sensor at normal temperatures. However, since the electrical and mechanical properties of SCS deteriorate at elevated temperatures, it is only possible for Si-based pressure sensors to function in high temperature environments by applying proper packaging techniques or thermal isolation methods. Some researchers have employed new materials, such as silicon carbide as sensing material in MEMS sensors in order to extend the application of the devices to a temperature range above 500°C. The micro-fabrication processes for SiC is not mature and SiC sensors are very expensive. Therefore, the development of high temperature low-cost pressure sensor based on silicon micromachining technology is always desirable.

Using silicon diaphragms to sense the pressure in high temperature environment is possible. It has been shown that a piezeoresistive pressure sensor which is based on the silicon diaphragm exhibited very low pressure hysteresis at 500°C [2-34]. This means a well designed SCS diaphragm is capable of operating at very high temperature without creep or plastic deformation. So it is worth investigating the elevated temperature behaviour of the silicon diaphragms in order to prevent the diaphragms from being plastically deformed, and to minimize the effect of the creep deformation.

The yield strength and the creep properties of the bulk silicon and the SCS micro components are reviewed along with the mechanical testing methods which have been applied. The plastic behaviour of nanometric SCS wires or micron-sized SCS film is very different from that of bulk silicon or wet-etched silicon membranes due to the differences in the fabrication routes and the scale of the structures. At the same time, creep tests have been carried out for bulk SCS for various stress and temperature combinations. However the creep in SCS MEMS devices has seldom been studied. It is therefore important to characterize the high temperature behaviour of

micromachined SCS diaphragms in this project. The characterization work is valuable to the development of MEMS devices for harsh environments.

List of References

[2-1] Jack WJ, Microelectromechanical systems (MEMS): fabrication, design and applications. SMART MATER AND STRUCT 2001; 10(6): 1115

[2-2] Eddy DS and Sparks DR, Application of MEMS technology in automotive sensors and actuators. P IEEE 1998; 86(8): 1747

[2-3] Northrup MA, Gonzalez C, Hadley D, Hills RF, Landre P, Lehew S, et al. A MEMS-based miniature DNA analysis system. Proc. 8th International Conference on Solid-State Sensors and Actuators (Transducers '95) Stockholm, Sweden (25–29 June 1995), 764–767.

[2-4] Ziaie B, Baldi A, Lei M, Gu Y, and Siegel RA, Hard and soft micromachining for BioMEMS: review of techniques and examples of applications in microfluidics and drug delivery. ADV DRUG DELIVER REV 2004; 56(2): 145

[2-5] Miller LM, MEMS for space applications. P SPIE 1999; 3680(2): 2-11

[2-6] Cheng J and Wise KD, A high-resolution silicon monolithic nozzle array for inkjet printing. Electron Devices, IEEE Transactions on 1997; 44(9): 1401

[2-7] Hornbeck J, Digital Light Processing™ for high-brightness, high-resolution applications. In: Electronic Imaging, EI '97, Projection Displays III. February 10–12, San Jose*, CA* (1997), 27–40.

[2-8] Madhab GB, Intelligent Microsystems: an Overview. in Engineering, Sciences and Technology, Student Conference On. 2004.

[2-9] Marinis TF, The Future of Microelectromechanical systems (MEMS). STRAIN 2009; 45:208-220

[2-10] Stauffer JM, Current Capabilities of MEMS Capacitive Accelerometers in a Harsh Environment. Aerospace and Electronic Systems Magazine, IEEE 2006; 21(11): 29-32

[2-11] Beeby S, Ensell G, and Kraft M, et al. MEMS Mechanical Sensors. Norwood, Artech House, Inc. 2004

[2-12] Greenwood JC, Silicon in mechanical sensors. J PHYS E SCI INSTRUM, 1988; 21: 1114-1128

[2-13] Madou MJ. Fundamentals of Microfabrication: the science of miniaturization. New York: CRC Press; 1997

[2-14] Hase Y, Bessho M, Ipposhi T. SOI type pressure sensor for high temperature pressure measurement, SAE Technical Paper 940634, 1994

[2-15] Mehregany M, Zorman CA, Rajan N, and Wu CH, Silicon carbide MEMS for harsh environments. P IEEE 1998; 86(8): 1594-1610

[2-16] Ko WH and Wang Q, Touch mode capacitive pressure sensors. SENSOR ACTUATOR A-PHYS 1999; 75(3): 242

[2-17] Moe ST, Schjølberg-Henriksen K, Wang DT, Lund E, Nysæher J, Furuberg L, et al. Capacitive differential pressure sensor for harsh environments. SENSOR ACTUATOR A-PHYS 2000; 83(1-3): 30

[2-18] Clark SK and Wise KD, Pressure sensitivity in anisotropically etched thin-diaphragm pressure sensors. Electron Devices, IEEE Transactions on 1979; 26(12): 1887

[2-19] Aravamudhan S and Bhansali S, Reinforced piezoresistive pressure sensor for ocean depth measurements. SENSOR ACTUATOR A-PHYS 2008; 142(1): 111

[2-20] Stemme G, Resonant silicon sensors. J MICROMECH MICROENG 1991; 1(2): 113

[2-21] Elwenspoek M, Blom FR, Bouwstra S, Lammerink TSJ, Pol van de FCM, Tilmans HAC, et al., Transduction mechanisms and their applications in micromechanical devices, in IEEE Micro Electro Mechanical Systems, MEMS. 20-22 Feb. 1989, IEEE: Salt Lake City, UT.

[2-22] Howe RT, Resonant microsensors. Proceedings of the 4th International Conf. on Solid-State Sensors and Actuators, Tokyo, 1987: 843

[2-23] Harris CM and Crede CE, Shock and Vibration handbook, 3rd ed. MeGraw-Hill, New York, 1988

[2- 24] Christen M, Air and gas damping of quartz tuning forks. SENSOR ACTUATOR 1983; 4:(555-64)

[2- 25] Beeby S, Ensell G, Kraft M and White N, MEMS Mechanical Sensors, Norwood: Artech House, Inc; 2004

[2-26] Greenwood JC, Etched silicon vibrating sensor. J PHYS E SCI INSTRUM 1984; 17(8): 650

[2-27] Kroetz GH, Eickhoff MH, and Moeller H, Silicon compatible materials for harsh environment sensors. SENSOR ACTUAT A-PHYS 1999; 74(1-3): 182

[2-28] Ned AA, Okojie RS, and Kurtz AD, 6H-SiC pressure sensor operation at 600°C. In: High Temperature Electronics Conference, HITEC. 1998 Fourth International. 14-18 Jun 1998, Albuquerque, NM, USA.

[2-29] Wu CH, Stefanescu S, Kuo HI, Zorman CA and Mehregany M. Fabrication and testing of single crystalline 3C-SiC piezoresistive pressure sensors. The 11th International Conference on Solid-State Sensors and Actuators, 2001, Munich, Germany.

[2-30] Young DJ, Du J, Zorman CA and Ko WH, High-temperature single-crystal 3C-SiC capacitive pressure sensor. Sensors Journal, IEEE 2004; 4(4): 464

[2-31] Azevedo RG, Zhang J, Jones DG, Myers DR, Jog AV, Jamshidi B et al. Silicon carbide coated MEMS strain sensor for harsh environment applications. In: Micro Electro Mechanical Systems, 2007. MEMS. IEEE 20th International Conference on. 21-25 Jan 2007, 643

[2-32] Zhang H, Guo H, Wang Y, Zhang G and Li Z, Study on a PECVD SiC-coated pressure sensor. J MICROMECH MICROENG 2007; 17(3): 426

[2-33] Volinsky AA, Kravchenko G, Waters P, Reddy JD, Locke C, Frewin C et al. Residual Stress in CVD-grown 3C-SiC Films on Si Substrates. MRS PROC 2008; 1069, 1069-D03-05

[2-34] Quo S, Eriksen H, Childress K, Fink A, and Hoffman M, High temperature high accuracy piezoresistive pressure sensor based on smart-cut soi. In: Micro Electro Mechanical Systems, 2008. MEMS 2008. IEEE 21st International Conference on. 13-17 Jan 2008. Tucson, AZ. 892-895

[2-35] Zhao Y, Zhao L, and Jiang Z, A novel high temperature pressure sensor on the basis of SOI layers. SENSOR ACTUAT A-PHYS 2003; 108(1-3): 108

[2-36] Spearing SM, Materials issues in microelectromechanical systems (MEMS). ACTA MATER 2000; 48(1): 179-196

[2-37] Nakao S, Ando T, Shikida M, and Sato K, Effect of temperataure on fracture toughness in a single-crystal-silicon film and transition in its fracture mode. J MICROMECH MICROENG 2008; 18(1), 015026

[2- 38] Bonnotte E, Delobelle P, Bornier L, Trolard B, Tribillon G, Two interferometric methods for the mechanical characterization of thin films by bulging tests. Application to silicon single crystal. J MATER RES 1997; 12(9): 2234-2248

[2-39] Schindel DW, Hutchins DA, and Smith ST, A study of materials at high temperature using miniaturized resonant tuning forks and noncontact capacitance transducers. J ACOUST SOC AM 1997; 102(3): 1296

[2- 40] Samuel J, Roberts SG, The Brittle-Ductile Transition in Silicon. I. Experiments. P ROY SOC LOND A MAT 1989; 421: 1-23

[2-41] Patel JR, Chaudhuri AR, Macroscopic Plastic Properties of Dislocation - Free Germanium and Other Semiconductor Crystals. I. Yield Behavior. J APPL PHYS 1968; 34(9): 2788

[2-42] Pearson GL, Read WT, Feldmann WL, Deformation and fracture of small silicon crystals. ACTA METALL MATER 1957; 5(4): 181-191

[2-43] Sumino, K, Deformation behavior of silicon. METALL MATER TRANS A 1999; 30(6): 1465-1479

[2- 44] Huff MA, Nikolich AD, and Schmidt MA, Design of sealed cavity microstructures formed by silicon wafer bonding. J MICROELECTROMECH S 1993; 2(2): 74

[2-45] Frühauf J, Gärtner E, Jänsch E, New aspects of the plastic deformation of silicon–prerequisites for the reshaping of silicon microelements. APPL PHYS A 1999; 68(6): 673-679

[2-46] Namazu T, Isono Y, Tanaka T, Plastic deformation of nanometric single crystal silicon wire in AFM bending test at intermediate temperatures. J MICROELECTROMECH S 2002; 11(2): 125-135

[2-47] Nakao S, Ando T, Shikida M and Sato K, Mechanical properties of a micron-sized SCS film in a high-temperature environment. J MICROMECH MICROENG 2006; 16(4): 715

[2-48] Agrawal BK Introduction to engineering materials. Delhi: Tata McGraw-Hill Education; 1988

[2-49] John V. Introduction to Egnineering Materials. 3rd edition, Hampshire and London: MACMILLAN PRESS LTD; 1992, P414

[2-50] Reppich B, Haasen P, Llschner B, Kriechen von Silizium-Einkristallen. ACTA METALL MATER 1964; 12(11): 1283-1288

[2-51] Myshlyaev MM, Nikitenko VI, and Nesterenko VI, Dislocation Structure and Macroscopic Characteristics of Plastic Deformation at Creep of Silicon Crystals. PHYS STATUS SOLIDI (b) 1969; 36(1): 89-96

[2-52] Taylor TA and Barrett CR, Creep and recovery of silicon single crystals. MATER SCI ENG 1972; 10: 93-102.

[2-53] Walters DS and Spearing SM, On the flexural creep of single-crystal silicon. SCRIPTA MATER 2000; 42(8): 769

[2-54] Hollenberg GW, Terwilliger GR and Gordon RS, Calculation of Stresses and Strains in Four-Point Bending Creep Tests. J AM CERAM SOC 1971; 54(4): 156-159

[2-55] Mehra A, Ayon AA, Waitz IA, and Schmidt MA, Microfabrication of high-temperature silicon devices using wafer bonding and deep reactive ion etching. J MICROELECTROMECH S 1999; 8(2): 152

3 SIMULATION OF THE BEHAVIOUR OF SILICON DIAPHRAGMS

3.1 *Introduction*

The aim of this chapter is to predict the mechanical behaviour of the pressurized silicon diaphragms both at room temperature and high temperature (600-1000°C) environments. The fundamental principles that are necessary for understanding the silicon diaphragm behaviour are summarized at first. Based on the test structure which is going to be used for the creep experiment, the elastic deflection of the silicon diaphragms is simulated with both isotropic properties and orthotropic properties. Finally, the occurrence of the plastic deformation at elevated temperatures is predicted by taking advantage of the finite element method.

3.2 *Basic principles and test sample design*

3.2.1 Elastic properties of SCS

Single crystal silicon is an orthotropic material due to its unique crystal structure. As shown in Figure 3- 1, silicon has the basic diamond cubic structure. It can be considered as two interpenetrating FCC (face-cantered-cubic) diamond structures. The lattice parameter is 5.43095Å. Each silicon atom has four nearest neighbours. The chemical bonds between the atoms are purely covalent. Due to the asymmetrical crystal structure and the nonuniform interatomic spacing, the elastic properties of silicon at a point are different in three mutually perpendicular directions.

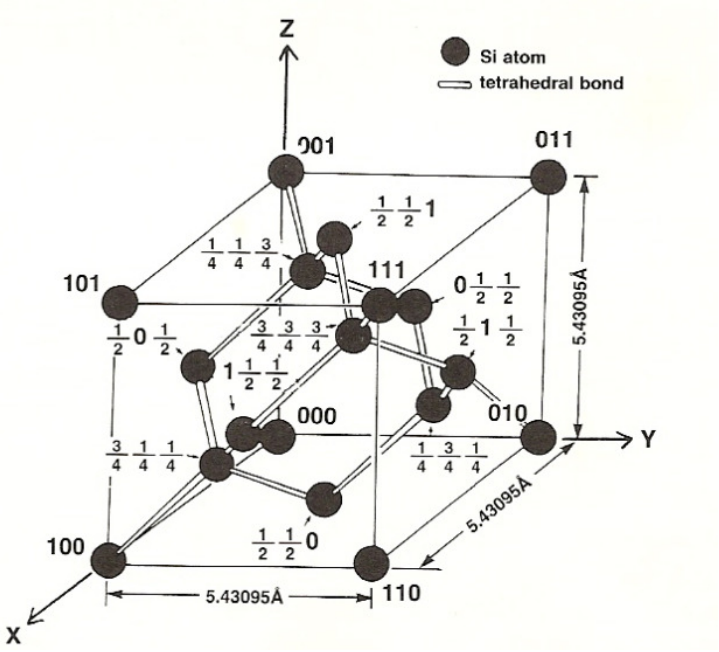

Figure 3- 1 Schematic diagram of the crystal structure of silicon [3-1]

The relationship between stress and strain in a coordinate system with axes equivalent to the axes of the unit cell can be expressed as [3-2]:

Equation 3- 1

$$\begin{bmatrix} \sigma_x \\ \sigma_y \\ \sigma_z \\ \tau_{xy} \\ \tau_{xz} \\ \tau_{yz} \end{bmatrix} = \begin{bmatrix} c_{11} & c_{12} & c_{12} & 0 & 0 & 0 \\ c_{12} & c_{11} & c_{12} & 0 & 0 & 0 \\ c_{12} & c_{12} & c_{11} & 0 & 0 & 0 \\ 0 & 0 & 0 & c_{44} & 0 & 0 \\ 0 & 0 & 0 & 0 & c_{44} & 0 \\ 0 & 0 & 0 & 0 & 0 & c_{44} \end{bmatrix} \times \begin{bmatrix} \varepsilon_x \\ \varepsilon_y \\ \varepsilon_z \\ \gamma_{xy} \\ \gamma_{xz} \\ \gamma_{yz} \end{bmatrix}$$

where c_{11}=165.7GPa, c_{12}=63.9GPa, c_{44}=79.6GPa. The elastic constants in any direction can be calculated by coordinate transformation of the stiffness coefficient matrix in Equation 3- 1 [3-3]. The graphical representations of Young's modulus, shear modulus and Poisson's ratio in (100) plane as a function of direction are shown in Figure 3- 2 (a), (b) and (c). It can be seen that the Young's modulus varies from 130.2GPa to 168.9GPa with a minimum in the <100> directions and a maximum in the <110> directions. The shear modulus and Poisson's ratio are in the range from

50.92GPa to 79.37GPa and from 0.0642 to 0.2786, separately, with a minimum in the <110> directions and a maximum in the <100> directions.

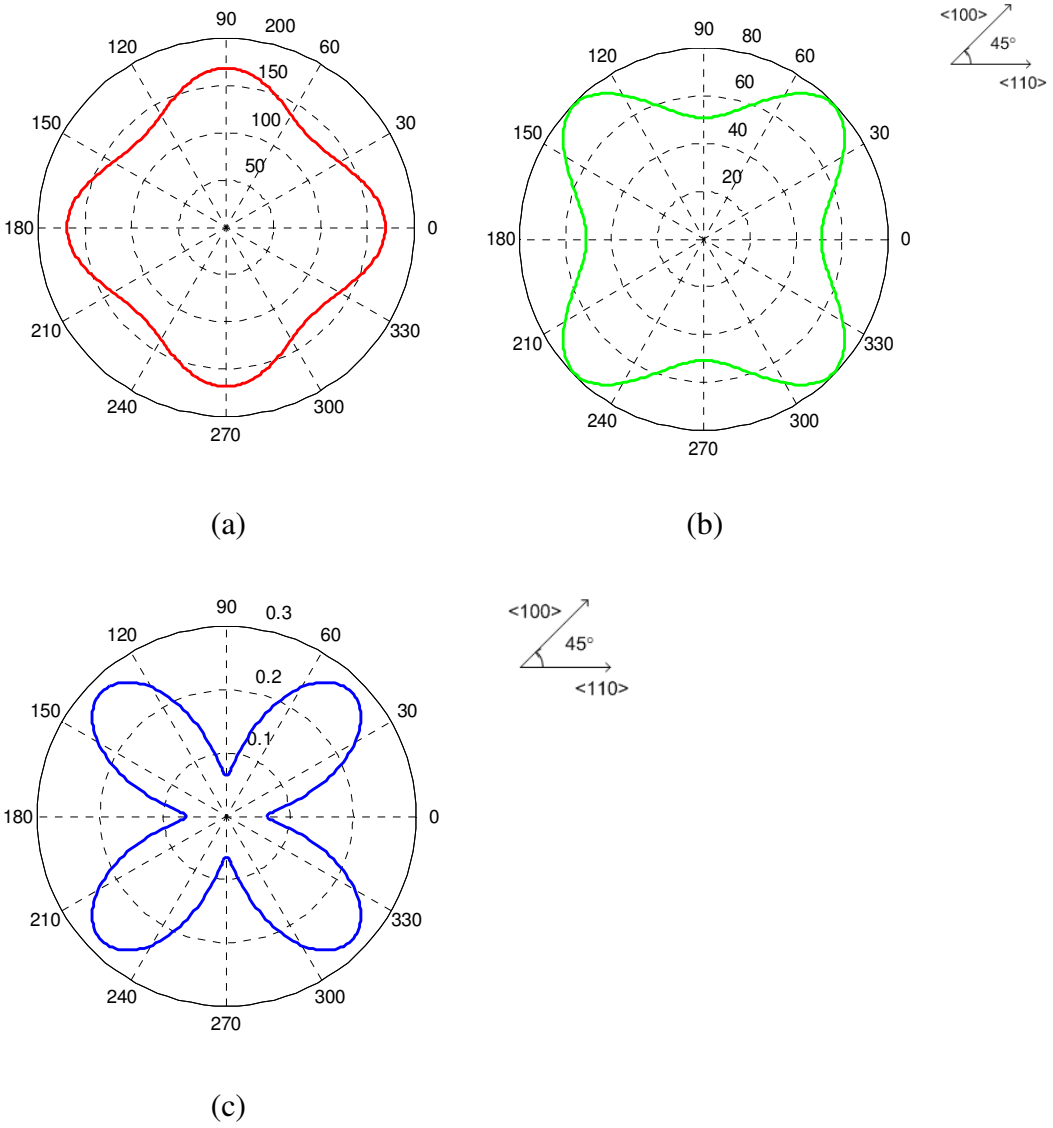

Figure 3- 2 Elastic properties of silicon as a function of direction in the (100) plane (GPa) (a) Young's Modulus; (b) Shear Modulus; (c) Poisson's ratio

In addition, the inverse of the stiffness coefficient can be obtained from the elastic constants defined in three mutual perpendicular directions x, y and z:

$$C^{-1} = \begin{bmatrix} \frac{1}{E_x} & -\frac{\nu_{yx}}{E_y} & -\frac{\nu_{zx}}{E_z} & 0 & 0 & 0 \\ -\frac{\nu_{xy}}{E_x} & \frac{1}{E_y} & -\frac{\nu_{zy}}{E_z} & 0 & 0 & 0 \\ -\frac{\nu_{xz}}{E_x} & -\frac{\nu_{yz}}{E_y} & \frac{1}{E_z} & 0 & 0 & 0 \\ 0 & 0 & 0 & \frac{1}{G_{xy}} & 0 & 0 \\ 0 & 0 & 0 & 0 & \frac{1}{G_{yz}} & 0 \\ 0 & 0 & 0 & 0 & 0 & \frac{1}{G_{xz}} \end{bmatrix}$$

where E, ν and G are Young's modulus, Poisson's ratio and shear modulus. The elastic constants for the condition that x and y axis coincide with <110> directions in (100) plane are listed in Table 3- 1.

Table 3- 1 Elastic constants of silicon (x and y axis coincide with <110> directions in (100) plane)

E_x	168.9GPa	E_y	168.9GPa	E_z	130.2GPa
ν_{xy}	0.0642	ν_{yz}	0.0642	ν_{xz}	0.2786
G_{xy}	50.9GPa	G_{yz}	50.9GPa	G_{xz}	79.37GPa

At the same time, silicon exhibits reductions in the stiffness coefficients with increasing temperature. Table 3- 2 shows the temperature coefficients of the stiffness coefficients.

Table 3- 2 Temperature coefficients of the stiffness coefficients of silicon [3-4]

Stiffness coefficient (GPa)	Temperature coefficient of stiffness coefficient (K^{-1})
C_{11}=164.8±0.16	$(dC_{11}/dT)/C_{11}= -122\times10^{-6}$
C_{12}=63.5±0.3	$(dC_{12}/dT)/C_{12}= -162\times10^{-6}$
C_{44}=79.0±0.06	$(dC_{44}/dT)/C_{44}= -97\times10^{-6}$

3.2.2 Fracture strength of SCS

Failure of brittle silicon is governed by the maximum principal tensile stress presented in the complex stress system. The presence of internal cracks, flaws or the discontinuities of the structure can lead to stress concentrations in brittle silicon. When the maximum principal stress caused by the stress concentration exceeds the fracture strength, the interatomic bonds in the crystal would break and the elastic failure of the material occurs. The SEM image of a pressure sensitive silicon diaphragm and the consequent fracture surface caused by back loading are shown in Figure 3- 3. This failure mode is common to micromachined sensors which are designed for high pressure environment at low temperature.

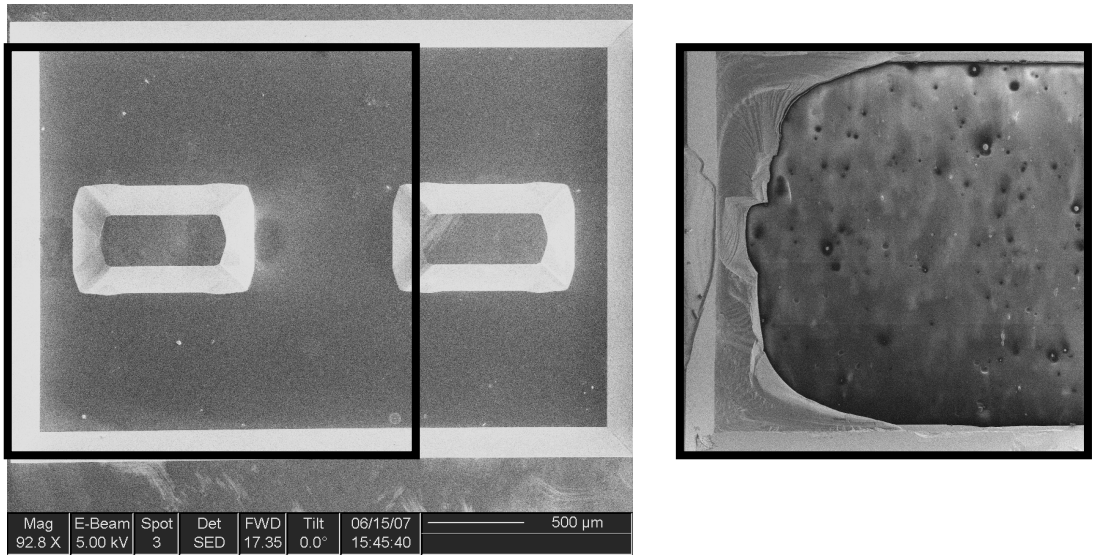

(a) (b)

Figure 3- 3 SEM micrograph of (a) a pressure sensitive silicon diaphragm and (b) fracture surface of broken diaphragm due to back loading (samples are provide by Druck)

The measured strength for various orientations of silicon crystal is in the range from 0.6GPa to 17.53GPa by using a tensile test or a beam-bending test [3-5]. Since the size of the flaw usually decreases with the dimension of the structure, the statistical

data shows that small specimens are usually stronger than large specimens. Moreover, the fracture strength of micromachined silicon is also related to the fabrication process. Yi et al. studied the strength of <110> oriented silicon beams which are prepared by different wet etchants [3-6]. Because the samples etched by EDP (an aqueous solution of ethylene diamine and pyrocatechol) etchant showed smoother sidewalls, the average strength of the samples prepared by EDP is higher than those of the samples prepared by the XeF_2 (xenon difluoride), TMAH (tetramethylammonium hydroxide) and KOH (potassium hydroxide) etchants, respectively. (The average strength of the samples prepared by EDP, XeF_2, TMAH and KOH are 1.24GPa, 1.01GPa, 0.83GPa and 0.63GPa, respectively.)

Due to the anisotropy of silicon structure, the fracture strength and the fracture path are dependent on the crystallographic orientation. The research conducted by Li et al. showed that cracks in single crystal silicon propagate predominantly on {111} and {110} planes, and the fracture path is significantly affected by the inclination of the cleavage planes relative to the crack orientation [3-7].

3.2.3 Coefficient of thermal expansion of SCS

Thermal stresses in silicon may arise from the mechanical constraints or mismatch of the coefficient of thermal expansion (CTE) with the mating component. Due to the temperature dependence of the lattice parameter, above room temperature, silicon expands when it is heated and contracts when it is cooled. The amount of expansion or contraction is proportional to the temperature change and the coefficient of thermal

expansion. Okada and Tokumaru proposed the CTE of silicon for the temperature range from 300K to 1500K [3-8]:

$$\alpha(T) = (3.725\{1-\exp[-5.88\times10^{-3}(T-124)]\}+5.548\times10^{-4}T)\times10^{-6}\,K^{-1}$$

T is the absolute temperature. The CTE obtained from the expression is plotted in Figure 3- 4.

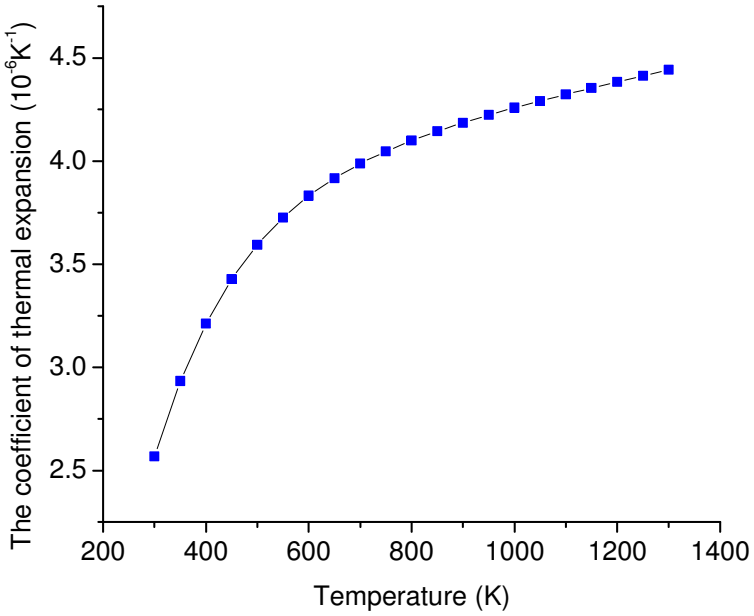

Figure 3- 4 The coefficient of thermal expansion for silicon from 300K to 1300K

3.2.4 Calculation of resolved shear stress in SCS

Dislocation glide (or slip) means the movement of dislocation along a crystallographic direction. The plastic deformation in single crystal silicon is caused by the dislocation slip which is initiated by the shearing stress resolved on the slip plane in the slip direction. Wherever the acting resolved shear stress obtained from the operating temperature field exceeds the critical value (yield strength), the crystallographic slip begins. Due to the face-cantered-cubic structure of silicon, the dislocations glide along

<011> directions on the dense atomic planes {111}. So there are totally 12 primary slip systems. For each slip system, the orientation of the slip planes and the slip directions are listed in Table 3- 3.

Table 3- 3 The primary slip systems of single crystal silicon [3-9]

S	1	2	3	4	5	6
n^s (Crystallographic orientation of the plane)	111	111	111	$1\,\bar{1}1$	$1\,\bar{1}1$	$1\,\bar{1}1$
l^s (Direction of gliding system S)	$\bar{1}\,01$	$0\,\bar{1}1$	$\bar{1}\,10$	$\bar{1}\,01$	011	110
S	7	8	9	10	11	12
n^s(Crystallographic orientation of the plane)	$\bar{1}\,11$	$\bar{1}\,11$	$\bar{1}\,11$	$11\,\bar{1}$	$11\,\bar{1}$	$11\,\bar{1}$
l^s (Direction of gliding system S)	$0\,\bar{1}1$	110	101	$\bar{1}\,10$	101	011

The resolved shear stress on a system S is the scalar product (double dot product) between the orientation tensor, m^s, and the macroscopic stress tensor, σ [3-10]:

Equation 3- 2

$$\tau^s = m^s : \sigma$$

where m^s is given by:

$$m_{ij}^s = \frac{1}{2}(n_i^s l_j^s + n_j^s l_i^s)$$

3.2.5 Structure of the test samples

The test samples are designed specially in order to be compatible with the micromachining process. As shown in

Figure 3- 5(a), a silicon diaphragm with a thickness of 50 μm is fixed to a silicon substrate. The cavity with a depth of 300 μm under the diaphragm is sealed in vacuum. The region of the circular diaphragm is determined by the shape of the cavity, as shown in

Figure 3- 5(b). The radius of the diaphragm is in the range of 0.5mm to 2.5mm in order to study the size effect on the diaphragm behaviour. The edges of the die are along <110> directions in the (100) plane. The test samples are expected to be exposed to the pressure of about 101, 325Pa (1atm) at room temperature (20°C) and elevated temperatures (600°C-900°C). All the following simulations are based on the designed sample structure and the proposed operating conditions.

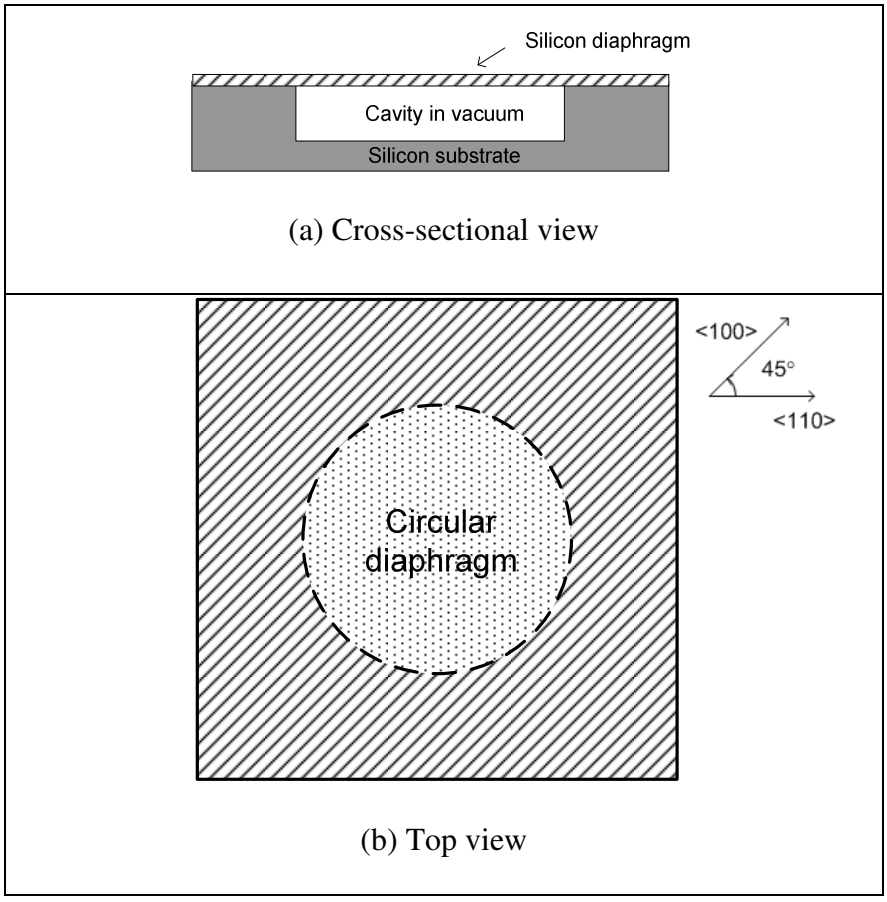

Figure 3- 5 The structure of test samples

3.3 *Elastic behaviour analysis of SCS diaphragms*

Silicon is brittle material at room temperature. So the deformation of the SCS diaphragms under applied pressure is elastic. The load-deflection behaviour of both isotropic and orthotropic diaphragms has been well studied by Timoshenko [3-11].

3.3.1 Theoretical analysis of isotropic diaphragms

The elastic properties of the material for isotropic diaphragms are the same in all directions. When the deflection is small, the lateral loads are carried by a bending action of the diaphragm only and the strain of the middle plane can be neglected. For a rigidly clamped circular diaphragm with small deflection, the deformation under a uniformly distributed pressure (P) is given by [3-11]:

Equation 3- 3

$$w(r) = \frac{P}{64D}(a^2 - r^2)^2$$

where r, a are the radial coordinate and the diaphragm radius, respectively. D is the flexural rigidity and is given as:

Equation 3- 4

$$D = \frac{Eh^3}{12(1-\nu^2)}$$

where h, E and ν are diaphragm thickness, Young's modulus and Poisson's ratio, respectively. It can be seen that the amount of defection is directly proportional to the applied pressure.

However, if the lateral deflection increases beyond 30% of diaphragm thickness, the force produced by the stretching of the middle surface plays an important role in resisting the lateral load. Therefore the strain of the middle plane needs to be taken into account in predicting the diaphragm deformation using large deflection theory. The deflection of the diaphragm is approximated as [3-11]:

Equation 3- 5

$$w(r) = w_0(1-\frac{r^2}{a^2})^2$$

where w_0 is the maximum displacement and is expressed as:

Equation 3- 6

$$w_0 = \frac{Pa^4}{64D}\frac{1}{(1+0.488\frac{w_0^2}{h^2})}$$

The effect of the stretching at the middle surface on the maximum deflection is represented by the last factor on the right-hand side of Equation 3- 6.

3.3.2 Theoretical analysis of orthotropic diaphragms

The small deflection solution for a clamped circular diaphragm with orthotropic properties is given by [3-11]:

Equation 3- 7

$$w(x,y) = \frac{P}{64D'}(a^2 - x^2 - y^2)^2 .$$

where the flexural rigidity D' is given by :

Equation 3- 8

$$D' = \frac{1}{8}(3D_x + 2H + 3D_y) .$$

where D_x and D_y are the flexural rigidities along x, y directions, respectively and are given by:

$$D_x = \frac{E_x}{1-\nu_x\nu_y}\frac{h^3}{12} \quad \text{and} \quad D_y = \frac{E_y}{1-\nu_x\nu_y}\frac{h^3}{12}.$$

where E_x, E_y, ν_x, ν_y are the moduli of elasticity and Poisson's ratios in the x and y directions, respectively. H is given by:

$$H = D_1 + 2D_{xy}.$$

In which D_1 and D_{xy} are torsional rigidities and are given by:

$$D_1 = \frac{E_x\nu_y}{1-\nu_x\nu_y}\frac{h^3}{12} \quad \text{and} \quad D_{xy} = \frac{G_{xy}h^3}{12}.$$

where G_{xy} is the shear modulus. The solution gives a good prediction for the deflection of the orthotropic diaphragms. However, the expression for the flexural rigidity D´ involves the elastic properties in different directions, thus making the calculation very complicated.

In order to simplify the calculation, the equivalent Young's modulus E_e and Poisson's ratio ν_e of the anisotropic diaphragms have been derived [3-12]:

$$E_e = (1-\nu_e^2)\left(\frac{3E_x}{1-\nu_x\nu_y} + \frac{3E_y}{1-\nu_x\nu_y} + \frac{2E_x\nu_y}{1-\nu_x\nu_y} + 4G_{xy}\right)/8.$$

$$\nu_e = \frac{\frac{E_x}{1-\nu_x\nu_y} + \frac{E_y}{1-\nu_x\nu_y} + \frac{6E_x\nu_y}{1-\nu_x\nu_y} - 4G_{xy}}{\frac{3E_x}{1-\nu_x\nu_y} + \frac{3E_y}{1-\nu_x\nu_y} + \frac{2E_x\nu_y}{1-\nu_x\nu_y} + 4G_{xy}}$$

So the small deflection of an anisotropic diaphragm can be approximated by applying the equivalent elastic properties in the solutions for isotropic diaphragms (Equation 3-3 and Equation 3- 4).

Table 3- 4 The elastic properties for (100) oriented silicon wafer [3-13]

Young's modulus	Shear modulus	Poisson's ratio	Equivalent value
E_x =168.9 [GPa] E_y =168.9 [GPa]	G_{xy}=50.9 [GPa]	ν_{xy}=0.0642 ν_{yx}=0.0642	E_{100}=151.3 [GPa] ν_{100}=0.1615

The equivalent elastic properties for (100) oriented silicon wafer are shown in Table 3- 4. The x-y plane coincides with the wafer surface. The x axis aligns with the <110> direction on the plane.

3.3.3 Simulation results of analytical models

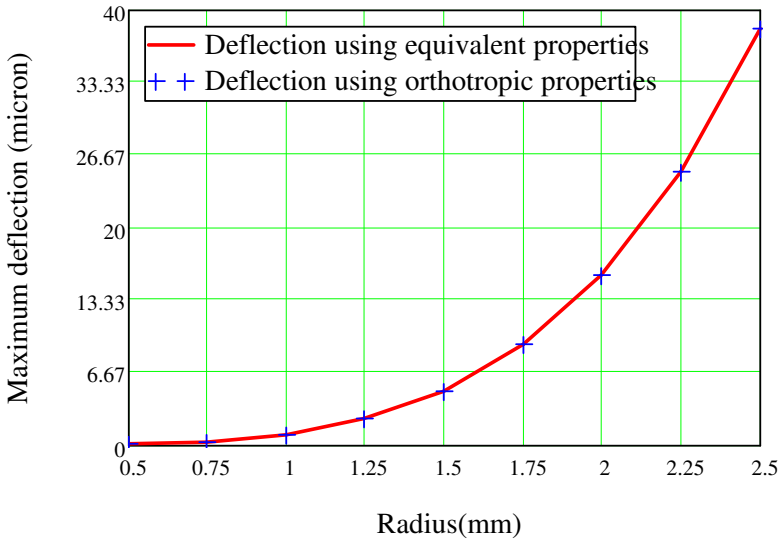

Figure 3- 6 Maximum deflection of the SCS diaphragms using small deflection theory

The small deflection of the circular silicon diaphragms is shown in Figure 3- 6. The diaphragms are under one atmospheric pressure (101.3kPa) at room temperature. The data which are represented by the red line is obtained by applying the equivalent properties of silicon in Equation 3- 3 and Equation 3- 4. The data which are represented by blue cross is obtained by applying the orthotropic properties of silicon in Equation 3- 7 and Equation 3- 8. It can be seen that the solutions which are based on the equivalent properties are very close to the results which are obtained from the orthotropic properties. Therefore, using the equivalent properties of silicon in the isotropic diaphragm solutions is an effective way to approximate the deflection of the orthotropic SCS diaphragms.

According to Figure 3- 6, the maximum deflection increases with the diaphragm radius under a given pressure. However, when the radius is in the range of 2mm-2.5mm, the maximum deflection is larger than 30% of the diaphragm thickness (15μm). So the use of the small deflection theory is not appropriate for the diaphragms with the radius from 2mm to 2.5mm.

3.3.4 FEA simulation using 2D axisymmetrical model

Finite element analysis (FEA) is a valuable tool for the diaphragm study since it is able to model the complex test sample structure. The elastic behaviour of the test structures are simulated using finite element method with the COMSOL Multiphysics 3.5a.

A simplified model with isotropic material properties is built in 2D axisymmetrical space. This equivalent elastic properties for (100) oriented silicon wafer (Table 3- 4) **are used. A simplified geometry of the test structure and the simulation results are shown in**

Figure 3- 7. The diaphragm radius is 2.5mm. The pressure is applied on the upper surface. The boundaries at the bottom and the sidewall of the substrate are rigidly fixed. The maximum displacement is at the centre of the diaphragm and is about 33.45μm. Figure 3- 8 shows that the maximum stress induced by the atmospheric pressure is around 174MPa at the upper corner of the diaphragm edge.

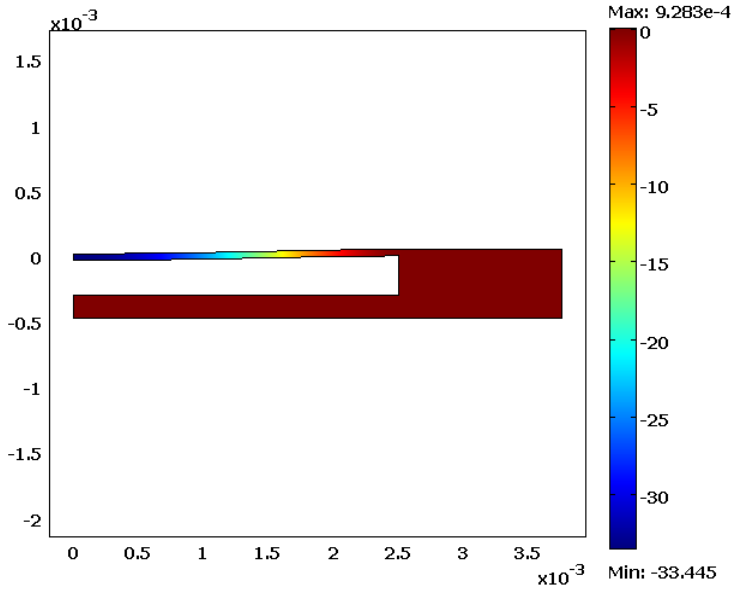

Figure 3- 7 The displacement of the test sample under atmospheric pressure in 2D axisymmetrical model (μm)

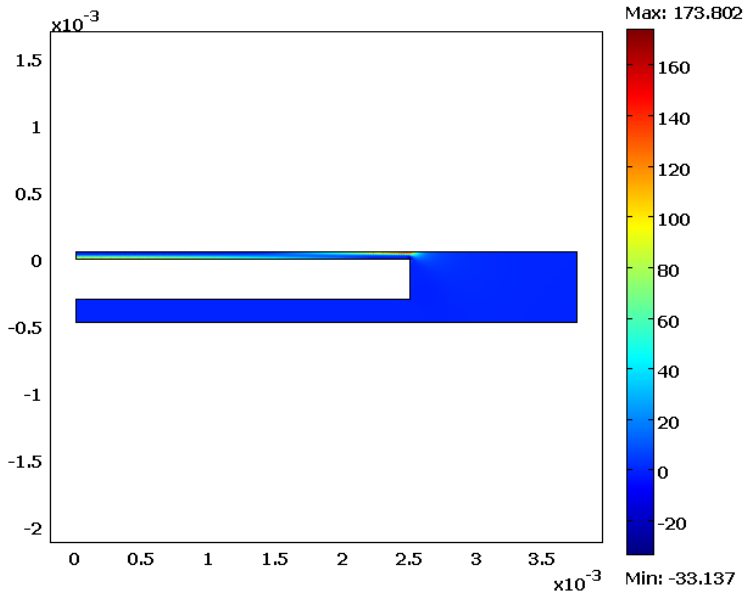

Figure 3- 8 The first principal stress of the test sample under atmospheric pressure in 2D axisymmetrical model (MPa)

3.3.5 FEA simulation using 3D orthotropic model

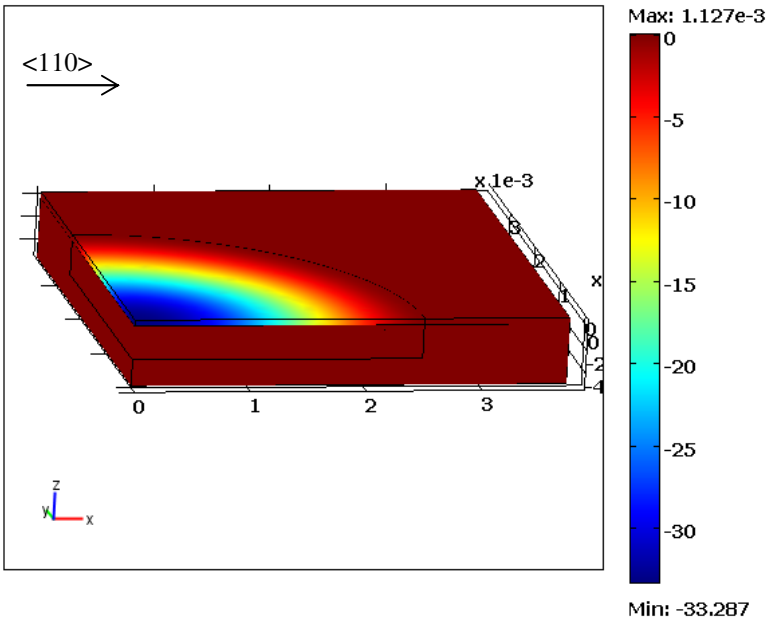

Figure 3- 9 The displacement of the test sample under atmospheric pressure in a quarter sample model (µm)

Since the test structure has two planes of symmetry, only a quarter of the test sample is modelled in 3-dimensional domain using orthotropic properties of silicon (elastic constants listed in Table 3- 1). In comparison with the model of the whole structure, this quarter model is able to reduce the memory used in the computation, and therefore reduces the computational time greatly. A quarter of the test structure and the simulation results are shown in Figure 3- 9. The diaphragm radius is 2.5mm. The x-axis of the model coordinate system aligns with crystallographic direction <110> in the (100) wafer plane. The pressure is applied on the upper surface of the sample. The boundaries at the bottom and the sidewall of the substrate are rigidly fixed (the same as those of the 2D axisymmetrical model). The results show that the diaphragm displacement is axisymmetrical with a maximum of 33.29μm at the centre. In Figure 3- 10, the first principal stress field is not axisymmetrical. The maximum value is predicted as 189MPa at the diaphragm edge and in the <110> direction.

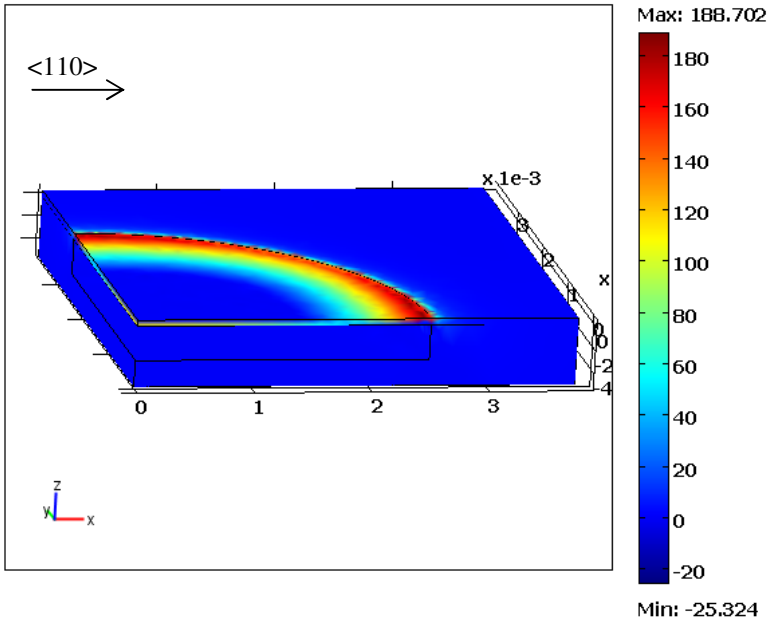

Figure 3- 10 The first principal stress of the test sample under atmospheric pressure in a quarter sample model (MPa)

3.3.6 Simulation results of FEA models

The simulation results of FEA models for all the test samples are listed in Table 3- 5. The 2D axisymmetrical model makes a good estimation of the diaphragm displacement because its predictions are very close to the simulation results obtained from the 3D orthotropic model. However, assuming the diaphragm to be isotropic leads to the underestimation of the maximum stress. For all diaphragm radiuses, the maximum first principal stresses are under the minimum fracture strength (600MPa) of single crystal silicon. Therefore, the micromachined silicon diaphragms are able to withstand the atmospheric pressure at room temperature.

Table 3- 5 List of FEA simulation results

	2D axisymmetrical model		3D orthotropic model	
Radius (mm)	Maximum deflection (μm)	Maximum stress (MPa)	Maximum deflection (μm)	Maximum stress (MPa)
0.50	0.08	6.18	0.08	7.78
0.75	0.37	14.8	0.36	16.8
1.00	1.11	27.2	1.08	29.2
1.25	2.65	43.7	2.57	47.0
1.50	5.39	64.1	5.24	69.3
1.75	9.75	88.5	9.54	96.2
2.00	16.0	116	15.7	126
2.50	33.4	174	33.3	189

3.4 *Prediction of the occurrence of plastic deformation*

3.4.1 The FEA model

The occurrence of the plastic deformation for single crystal silicon can be predicted by evaluating the magnitude of the resolved shear stress in the silicon structure. The plastic deformation begins when the resolved shear stress from the operating temperature field reaches the yield strength. Because the shear stress resolved on a slip system is related to the macroscopic stress tensor (Equation 3- 2 in section 3.2.4), the key point of the simulation is to calculate the pressure induced stress in the test structures. This can be done by the aid of COMSOL Multiphysics 3.5a. Because the definitions in section 3.2.4 are referred to the [100] crystal orientation, the geometry of the quarter FEA model needs to be aligned to the way that both the x and y directions of the model coordinate system are along <100> directions on the (100) plane, as shown in Figure 3- 11. Here the longest edge of the geometry is one edge of the test structure.

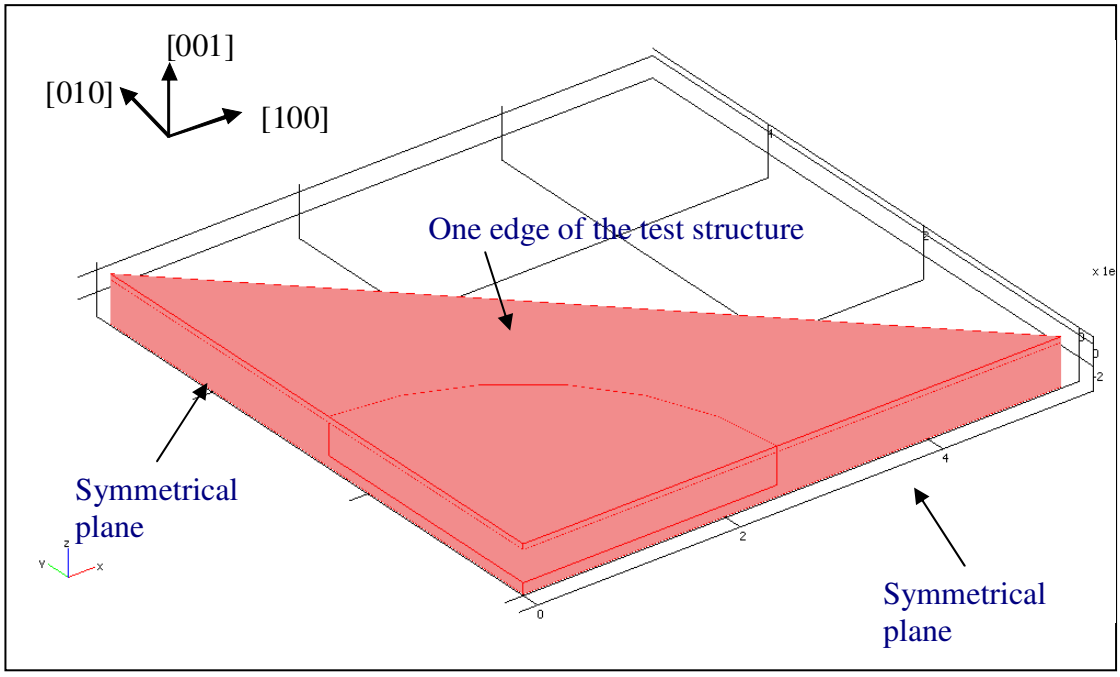

Figure 3- 11 A quarter FEA model defined along <100> directions

In this model, the elastic properties given by Equation 3- 1 are applied. Since the test samples are free to expand in the high temperature environment (this is because the silicon wafers are free to expand during high temperature annealing) and the structure is made of pure silicon, there is no thermally induced stress. At the same time, the temperature dependence of the elastic properties of silicon (Table 3- 2) is ignored in the analysis. This is because its effect on the stress field is very small compared with the effect of the applied pressure. The resolved shear stress for all the slip systems can then be obtained by applying the Cauchy stress in Equation 3- 2 :

Equation 3- 9

$$\tau^1 = \tau_{yz} - \tau_{xy} - \sigma_x + \sigma_z$$

$$\tau^2 = \tau_{xz} - \tau_{xy} - \sigma_y + \sigma_z$$

$$\tau^3 = \sigma_y - \tau_{xz} - \sigma_x + \tau_{yz}$$

$$\tau^4 = \tau_{xy} - \sigma_x - \tau_{yz} + \sigma_z$$

$$\tau^5 = \tau_{xy} + \tau_{xz} - \sigma_y + \sigma_z$$

$$\tau^6 = \sigma_x + \tau_{xz} - \sigma_y + \tau_{yz}$$

$$\tau^7 = \tau_{xy} + \tau_{xz} - \sigma_y + \sigma_z$$

$$\tau^8 = \tau_{xz} - \sigma_x + \sigma_y + \tau_{yz}$$

$$\tau^9 = \tau_{xy} - \sigma_x + \tau_{yz} + \sigma_z$$

$$\tau^{10} = \tau_{xz} - \sigma_x + \sigma_y - \tau_{yz}$$

$$\tau^{11} = \sigma_x + \tau_{xy} + \tau_{yz} - \sigma_z$$

$$\tau^{12} = \tau_{xy} + \tau_{xz} + \sigma_y - \sigma_z$$

3.4.2 Simulation results and prediction for plastic deformation

Figure 3- 12 shows the resolved shear stress in the silicon diaphragm for each slip system. The radius of the pressurized diaphragm is 2.5mm. Due to the orthotropic properties of single crystal silicon, the stress field for one slip system is different from that for another. It can be seen that the highest resolved shear stress is about 200MPa and occurs at the edge of the diaphragm for slip system 11 and 12.

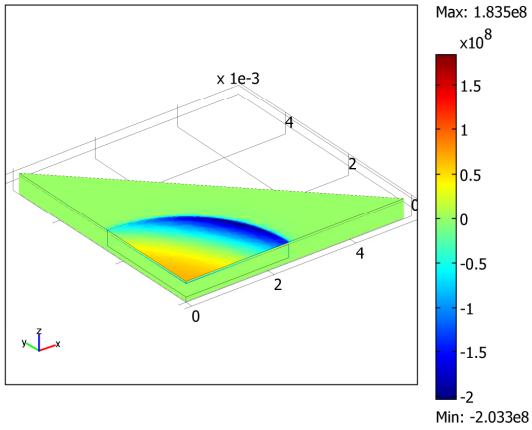

a) Slip system 1 [$\bar{1}$01] on (111)

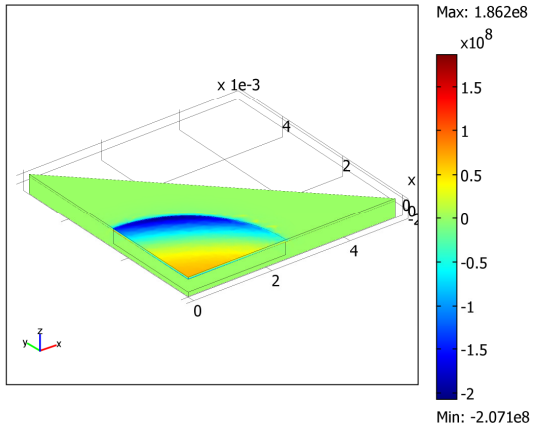

b) Slip system 2 [0$\bar{1}$1] on (111)

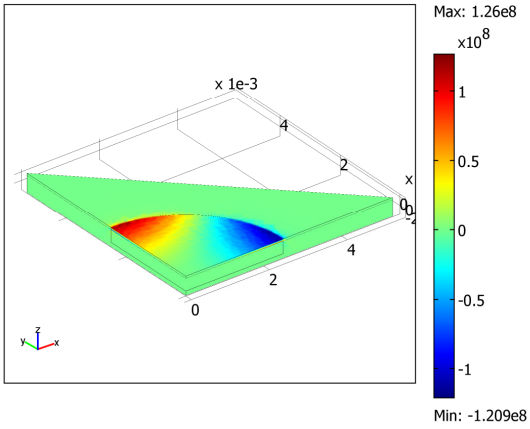

c) Slip system 3 [$\bar{1}$10] on (111)

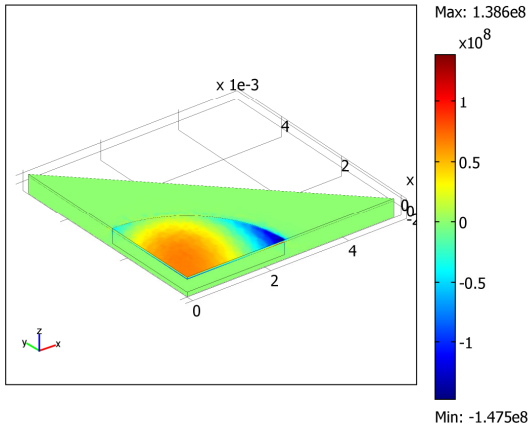

d) Slip system 4 [$\bar{1}$01] on (1$\bar{1}$1)

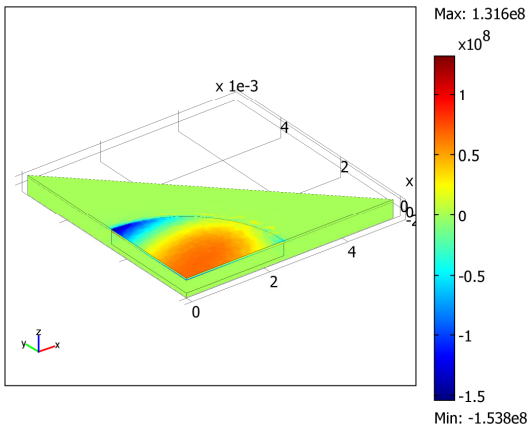

e) Slip system 5 [011] on (1$\bar{1}$1)

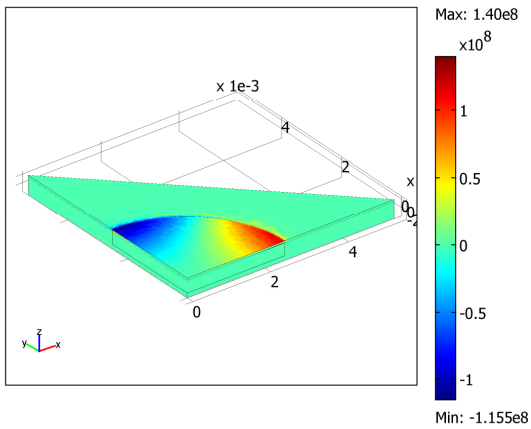

f) Slip system 6 [110] on (1$\bar{1}$1)

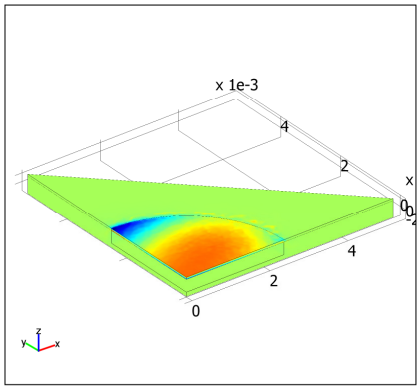

g) Slip system 7 [0$\bar{1}$1] on ($\bar{1}$11)

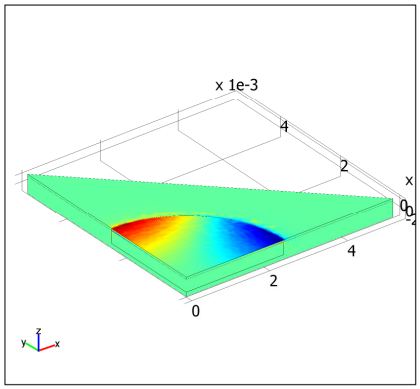

h) Slip system 8 [110] on ($\bar{1}$11)

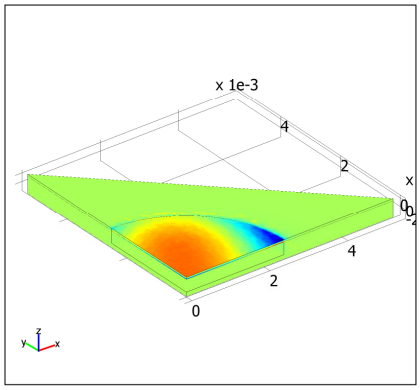

i) Slip system 9 [101] on ($\bar{1}$11)

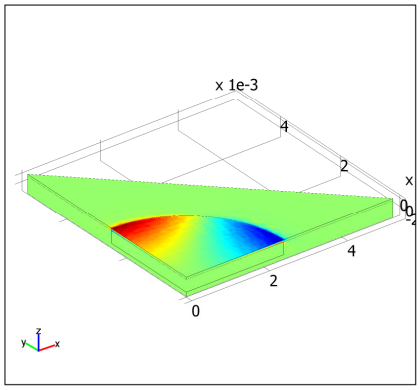

j) Slip system 10 [$\bar{1}$10] on (11$\bar{1}$)

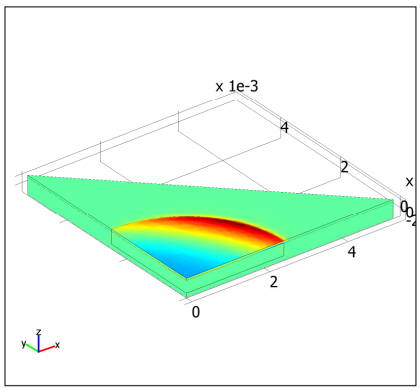

k) Slip system 11 [101] on (11$\bar{1}$)

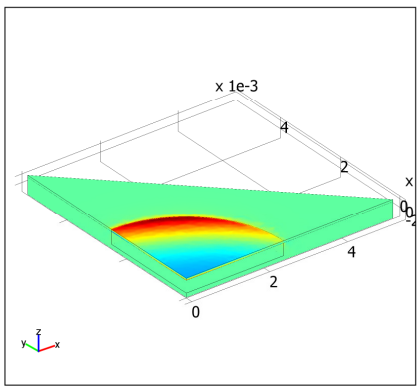

l) Slip system 12 [011] on (11$\bar{1}$)

Figure 3- 12 FEM simulation image of resolved shear stress [Pa]

At above 500°C, single crystal silicon becomes ductile, and the slip of dislocation begins when the resolved shear stress reaches the yield strength at the operating temperature. The yield strength for the dislocation-free silicon which was obtained at a strain rate of 5×10^{-3}cm/min (Figure 2- 10(b)) is used in this simulation [3-14]. Because the temperature dependence of the stiffness coefficients (Table 3- 2) is ignored in the model, the simulated elastic stress in the test structure is independent of the operating temperatures. Therefore, the magnitude of the resolved shear stress at elevated temperature fields remains the same.

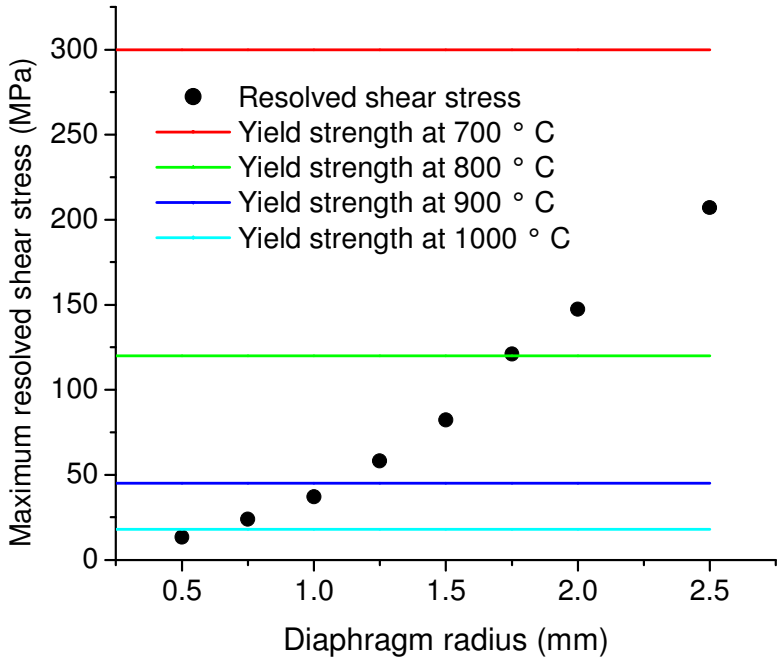

Figure 3- 13 Plot of maximum resolved shear stress in diaphragm as a function of diaphragm radius (comparison of resolved shear stress with yield strength)

The mechanical behaviour of the silicon diaphragm can be predicted by comparing the highest resolved shear stress with the yield strength at the operating temperature, as shown in Figure 3- 13. At 700°C, the yield strength is about 300MPa. The maximum resolved shear stresses for all the diaphragms are in the range from 13MPa

to 207MPa. Therefore, all the silicon diaphragms deform elastically when the temperature is less than 700°C. When the operating temperature increases to 800°C, the yield strength decreases to about 120MPa. The resolved shear stress is greater than the yield strength when the diaphragm radius is from 1.75mm to 2.5mm. So these diaphragms are likely to deform plastically. At 900°C, the plastic deformation is likely to occur for the diaphragms with a radius in the range of 1.25mm-2.5mm. When the operating temperature increases to 1000°C, the yield strength decreases dramatically to 18MPa so that most diaphragms would deform plastically.

The mechanical behaviour of the test samples is predicted in Figure 3- 14 for each diaphragm radius and operating temperature. It can be seen that the higher the operating temperature and the larger the diaphragm radius, the more likely the plastic deformation occurs.

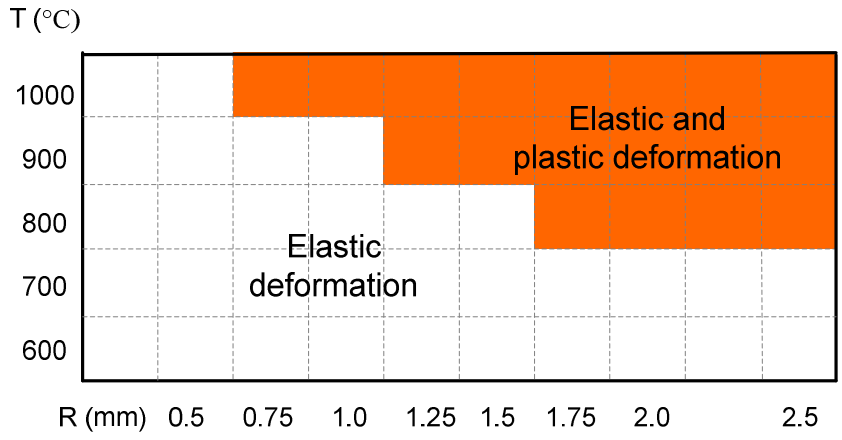

Figure 3- 14 Prediction of the diaphragm behaviour at high temperatures

In addition, the plastic region can also be predicted by the FEA model, as illustrated by

Figure 3- 15. The area where the resolved shear stress is larger than the yield strength for any slip system is demonstrated by the red colour. It can be seen that at 800°C, the slip of dislocations might occur at the region close to the diaphragm edge. When the temperature increases to 900°C, the whole diaphragm seems to deform plastically.

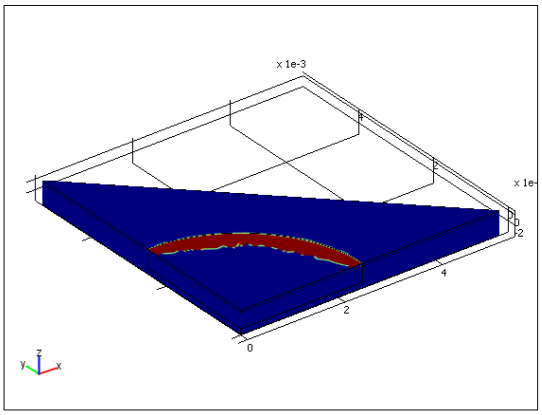

a) at 800 °C | b) at 900 °C

Figure 3- 15 Plastic zones in the diaphragm with a radius of 2.5mm (illustrated by red) predicted by FEA model

3.5 *Conclusions*

The small deflections of the circular SCS diaphragms are predicted by the analytical models. Since the elastic properties of silicon are orthotropic, the theoretical analysis of the diaphragm deformation under pressure is complicated. By applying the equivalent elastic properties of the orthotropic diaphragm in the isotropic diaphragm solutions, the calculation is simplified, and the small deflection is well approximated.

Moreover, the elastic deformation and the stress field of the test samples under pressure are simulated using finite element method. Both the 2D axisymmetrical model and the 3D orthotropic model make a good estimation of the diaphragm displacement. However, assuming the diaphragm to be isotropic leads to an underestimation of the induced stress in the diaphragm.

By comparing the resolved shear stress in the diaphragm with the yield strength, the occurrence of the plastic deformation is predicted for each diaphragm radius and each operating temperature. It is found that the higher the operating temperature and the larger the diaphragm radius, the more likely the plastic deformation occurs. However, this model can not predict the amount of the plastic deformation.

List of References

[3-1] Shimura F. Semiconductor silicon crystal technology. San Diego: Academic Press; 1989, P46

[3-2] Mason WP. Physical Acoustics and the Properties of Solids. New York: D.Van Nostrand Company; 1958

[3-3] Wortman JJ and Evans RA, Young's Modulus, Shear Modulus, and Poisson's Ratio in Silicon and Germanium, J APPL PHYS 1965; 36(1): 153-156

[3-4] Metzger H and Kessler FR. Der Debye-Sears-Effect zur Bestimmung de elastischen konstanten von Silicium. Z. Naturf. A 1970; 25: 904-906

[3-5] Korvink JG and Paul O, MEMS: a practical guide to design, analysis and applications. NY: William Andrew, Inc.; 2006.

[3-6] Yi T, Li L, and Kim C-J, Microscale material testing of single crystalline silicon: process effects on surface morphology and tensile strength. SENSOR ACTUAT A-PHYS 2000; 83(1-3): 172-178

[3-7] Li X, Kasai T, Nakao S, Ando T, Shikida M, Sato K, et al. Anisotropy in fracture of single crystal silicon film characterized under uniaxial tensile condition. SENSOR ACTUAT A-PHYS 117 (1):143-150, 2005.

[3-8] Okada Y and Tokumaru Y, Precise determination of lattice parameter and thermal expansion coefficient of silicon between 300 and 1500 K. J APPL PHYS (USA) 1984; 56: 314

[3-9] Cacho F, Orain S, Cailletaud G, and Jaouen H, A constitutive single crystal model for the silicon mechanical behavior: Applications to the stress induced by

silicided lines and STI in MOS technologies. MICROELECTRON RELIAB 2007; 47(2-3): 161-167

[3-10] Mandel J. Plasticité classque et viscoplasticité. Cours CISM, Udinc, Springer Verlag 1971; 97

[3-11] Timoshenko SP, and Woinowski-Krieger S, Theory of plates and shells, New York: McGraw-Hill; 1983

[3-12] Yasukawa A, Shimada S, Matsuoka Y, Kanda Y. Design Considerations for Silicon Circular Diaphragm Pressure Sensors. JPN J APPL PHYS 1982; 21: 1049-1052.

[3-13] Turley J and Sines G, The anisotropy of Young's modulus, shear modulus and Poisson's ratio in cubic materials. J PHYS D APPL PHYS 1971; 4(2): 264

[3-14] Patel JR, Chaudhuri AR, Macroscopic Plastic Properties of Dislocation - Free Germanium and Other Semiconductor Crystals. I. Yield Behavior. J APPL PHYS 1968; 34(9): 2788

4 THE MECHANICAL BEHAVIOUR OF SILICON DIAPHRAGMS AT HIGH TEMPERATURES

4.1 *Introduction*

It has been reported in section 2.3.1 that single crystal silicon becomes ductile and is susceptible to creep at elevated temperatures. So the silicon diaphragms might deform plastically or creep in the high temperature environment. The direct observation of the diaphragm behaviour during annealing is experimentally very difficult because elevated temperature is involved. However, both the plastic deformation and creep deformation are permanent, and the surface profiles of the test samples will be changed for ever. So the permanent deformation can be detected by studying the evolution of the surface profile with annealing process. Based on this concept, an experiment is designed to investigate the mechanical behaviour of micromachined silicon diaphragms at high temperatures.

The testing samples were fabricated by advanced MEMS technologies. The microfabrication process is presented at first, and then followed by the experimental procedures and settings. Since the test samples were exposed to the atmospheric pressure at room temperature after they are made, the resultant initial elastic deformation was investigated.

The mechanical behaviour of silicon diaphragms was studied using heavily doped silicon diaphragms at a temperature of 600°C, 800°C and 900°C, respectively. The maximum deflections for the diaphragms with radii from 0.5mm to 2.5mm are

reported with respect to the anneal time. Based on the evolution of the measured profiles, the effect of size and temperature on the diaphragm behaviour is discussed. The effect of the implanted argon ions on the diaphragm behaviour was investigated using lightly doped silicon diaphragms at a temperature of 800°C.

4.2 *Microfabrication of the test samples*

4.2.1 Overview of the fabrication process

The structure of the test samples has been illustrated in section 3.2.5. The fabrication process of the test samples is briefly illustrated in Figure 4- 1. The process starts with a 4-inch-diameter boron-doped <100> prime silicon wafer and a 4-inch-diameter <100> bond-and-etch-back-silicon-on-insulator (BESOI) wafer (step 1). The silicon wafers were provided by Si-mat^{TM} [4-1]. The prime silicon wafer is 525+/-25µm thick and double side polished, with a resistivity of 1-30 ohm-cm. The BESOI wafer has 50+/-0.5µm thick single crystal silicon (SCS) device layer and 0.5µm+/-5% thick silicon dioxide layer on a 400+/-5µm thick SCS handle wafer. The SCS device layer is <100> oriented silicon with boron doping resistivity of 0.001-0.002 ohm-cm. The handle wafer is <100> oriented silicon wafer with boron doping resistivity of 1-20 ohm-cm.

In step (2), a thin layer of photoresist is deposited at the front side of the prime silicon wafer, and the photoresist is then patterned using the designed mask. After that, the front side of the patterned wafer is etched using deep reactive-ion etching (DRIE) in step (3). In step (4), the silicon substrate is bonded to a (100) oriented BESOI wafer by silicon fusion bonding method [4-2]. Then, the silicon handle layer of the BESOI

wafer was totally etched away by KOH wet-etching process (step 5). Finally, the samples were made ready for the subsequent tests after the wet etching of the silicon dioxide layer in an HF solution (step 6).

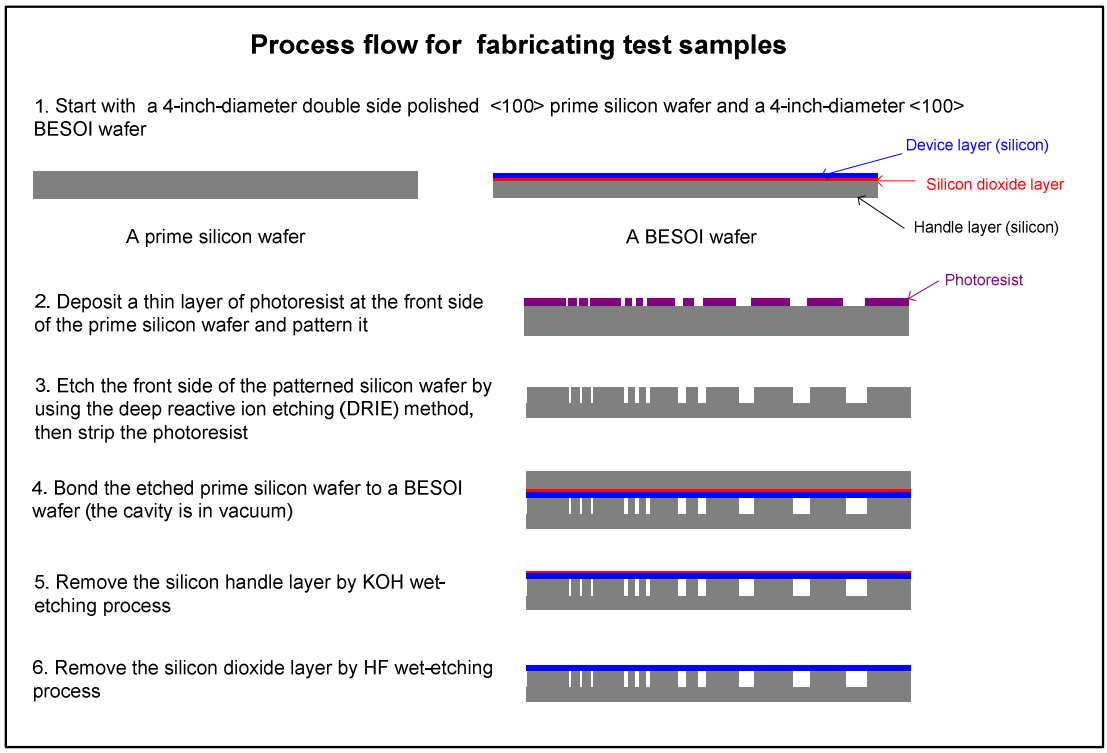

Figure 4- 1 Process flow for fabricating test samples

4.2.2 Lithography

Lithography is a special printing process used to transfer the detailed patterns to a photosensitive material by selective exposure to a radiation source. The process for the sample fabrication utilizes MEGAPOSIT^{TM} SPR^{TM} 220-7.0 positive photoresist [4-3]. Exposure to the UV light breaks the chemical chains of SPR220-7.0 so that the exposed resist becomes more soluble in the developer. The advantage of this resist is that thick layer of the resist can be achieved at relatively low spin speed. The silicon structure can therefore be protected from chemical attack during the etch process.

In the first step, the wafers are chemically cleaned to remove any particles and impurities using isopropyl alcohol (IPA) and acetone. Then the wafer is coated uniformly with SPR220-7.0 and spun for 40 seconds at 2000rpm. The thickness of the photoresist is about 9µm. The wafers are then 'soft baked' at 115°C for 90s using a hotplate. This soft bake reduces the remaining solvent content in the resist in order to improve resist adhesion to the wafer and anneal the shear stresses introduced during the spin-coating.

The photoresist was then exposed to a UV light source at a dose of 700mJ/cm^2 for 45s on a hard contact mode using Canon mask aligner PLA-501FA. The mask for the exposure consists of arrays of circular patterns which define the planar geometry of the cavity. After exposure, the resist is placed in developer MF 26A for approximately 2 minutes. The irradiated region of the resist is etched away in the developer. As shown in Figure 4- 2, the circular pattern is transferred to the resist for each cell. The photolithography is then completed with a hard bake at 95°C for 45 minutes on a hotplate in order to increase the stability of the remaining photoresist for subsequent processes.

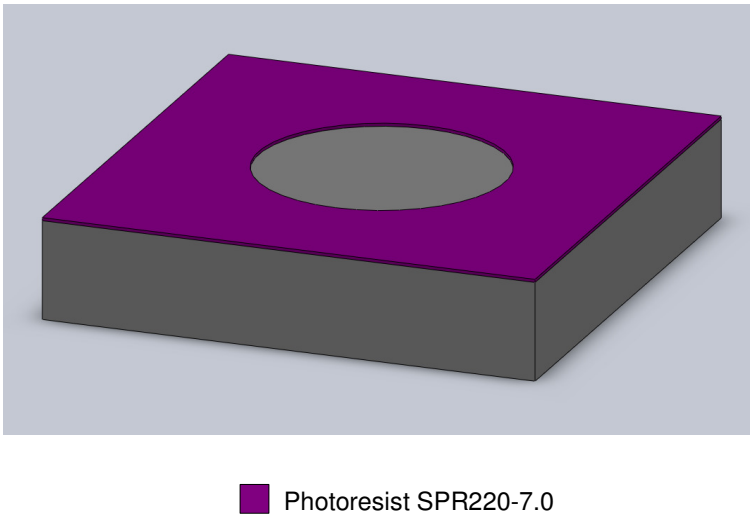

Figure 4- 2 One cell with a layer of photoresist after development

4.2.3 **DRIE**

The etching process transfers the pattern of the photoresist into the silicon wafer. After photolithography, the prime silicon wafer was etched using STS Multiplex ICP (inductively coupled plasma) etcher in order to form the cavity [4-4]. For MEMS application, DRIE is usually employed to make small trenches with high aspect ratios [4-5]. This process consists of sequential etching and passivating steps in order to achieve anisotropic etching [4-6], as shown in Figure 4- 3. In step (b), the etch proceeds in the high density inductively coupled SF_6 plasma. The selectivity to the photoresist is around 100:1. The passivation is achieved by deposition of a thin polymer on the wafer surface using C_4F_8 as a source gas, as illustrated by Figure 4- **3** (c). In the following etch step (d), the polymer on the bottom of the trench is then removed by energetic ions and silicon is etched. The polymer on the sidewall prevents the lateral etching and therefore the vertical sidewall profile is maintained. By repeating the etching and passivating cycles, the designed depth of the structure can be obtained.

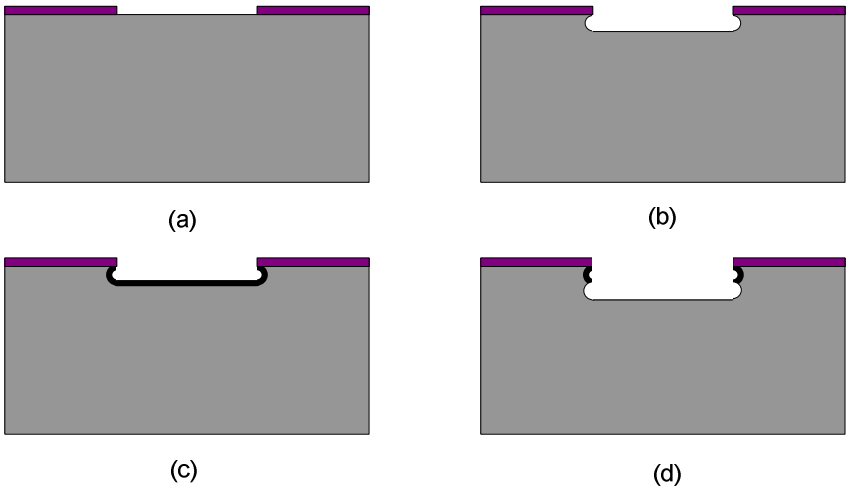

Figure 4- 3 schematic presentation of DRIE sequence [4-6]:
(a) Patterned photoresist on the prime silicon wafer, (b) Etching silicon in SF6 plasma,
(c) Passivation cycle to deposit a layer of polymer,
(d) The following etch step to remove the polymer at the base and to etch the exposed silicon

Since DRIE permits the fabrication of deep structures with the depth up to 500μm, it is a good tool to etch the silicon cavity with the depth of 300μm. The cavity radius ranges from 0.5mm to 2.5mm. The exposed area was estimated at 6%. The operating conditions of the STS were: 130sccm of SF6 (12W electrode power and 600W of coil power), 100sccm of C_4F_8 (0W electrode power and 600W of coil power), the APC set at 67.5°.

The wall profile is mainly controlled by the etching to deposition step time ratio in this case [4-7]. Insufficient passivation leads to an increase in lateral etching. Insufficient etching results in incomplete removal of the passivation and the formation of grass-like residues. The passivation and the etching must therefore be in balance to maintain profile anisotropy. Figure 4- 4 shows the SEM image of the cross section of an etched cavity. The etching to passivation step times ratio is 8s/5s. The grass-like structure at the cavity base shows that the protective polymer layer is not removed effectively in the etching process. The etching time in a cycle is then increased to 10s. However, the grass near the sidewall can be seen clearly in Figure 4- 5. So the duration of the etching is optimized to 12s with the average etch rate of 2.5μm/min.

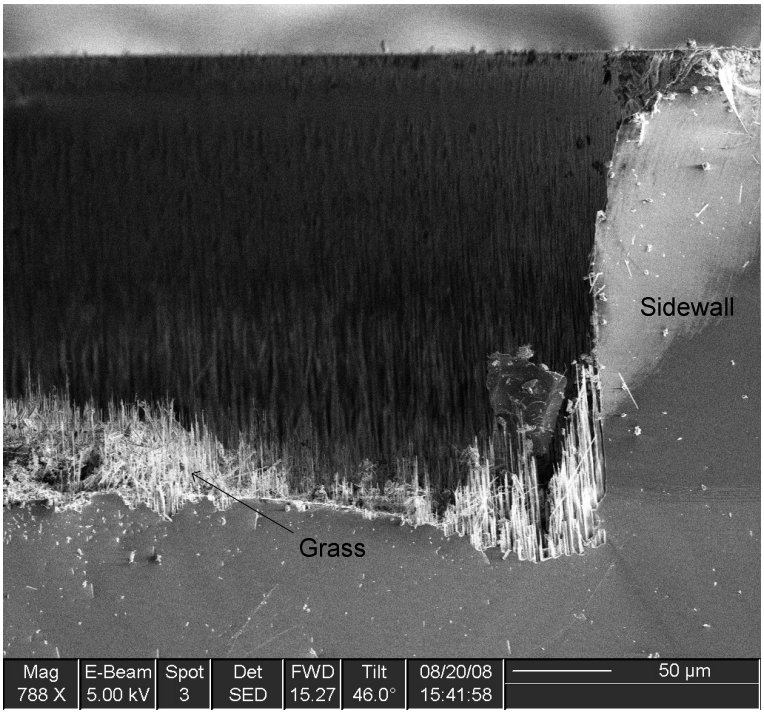

Figure 4- 4 SEM image of the grass with the etching over passivation time of 8s/5s

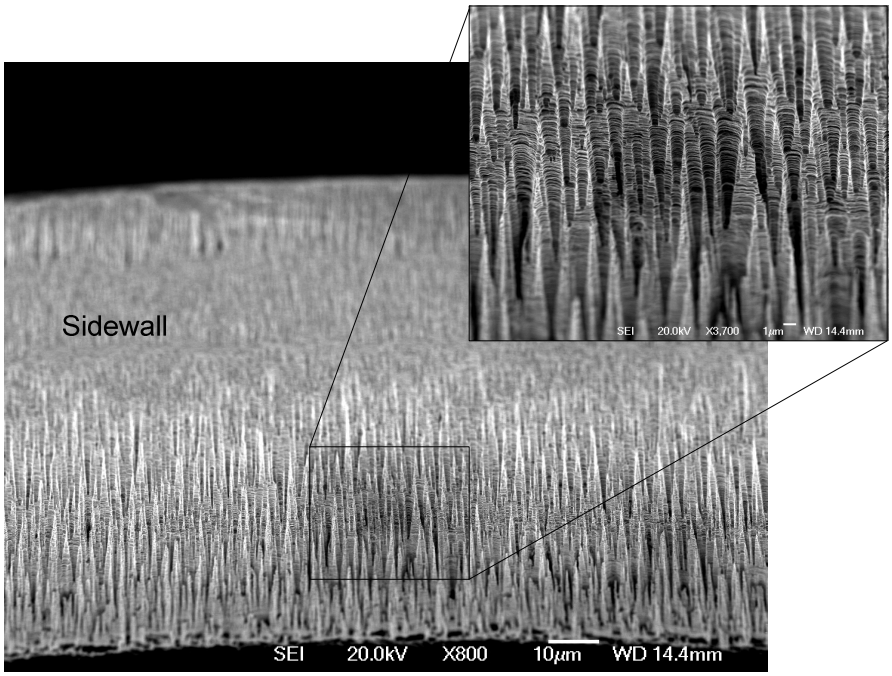

Figure 4- 5 SEM image of the grass with the etching over passivation time of 10s/5s

4.2.4 Wafer bonding

Silicon fusion bonding is a direct silicon-to-silicon bonding technique which creates high strength bonds between silicon wafers. The technology has been widely applied in the fabrication of silicon sensors, actuators and other microstructures [4-8]. Prior to bonding, both prime wafer and BESOI wafer went through a cleaning step to remove particles and to create two hydrophilic surfaces. The two wafers were then aligned and joined together at room temperature in a vacuum. A bonding force of 1.5kN was applied by the piston in order that an electrostatic bond can be formed between the surfaces. A high temperature anneal was then performed at 1100°C for 1 hour in a furnace filled with nitrogen gas. This process allowed a permanent diffusion bond to form between the device layer of the BESOI wafer and the silicon substrate of the prime silicon wafer. According to the study by Tada et al., the CTE of silicon is much higher than the CTE of silicon dioxide at high temperatures [4-9]. Therefore, when back to the room temperature, the tensile stress was induced in the silicon layer while the compressive stress was induced in the silicon dioxide layer. The schematic drawing of the test sample after silicon fusion bonding is shown in Figure 4- 6.

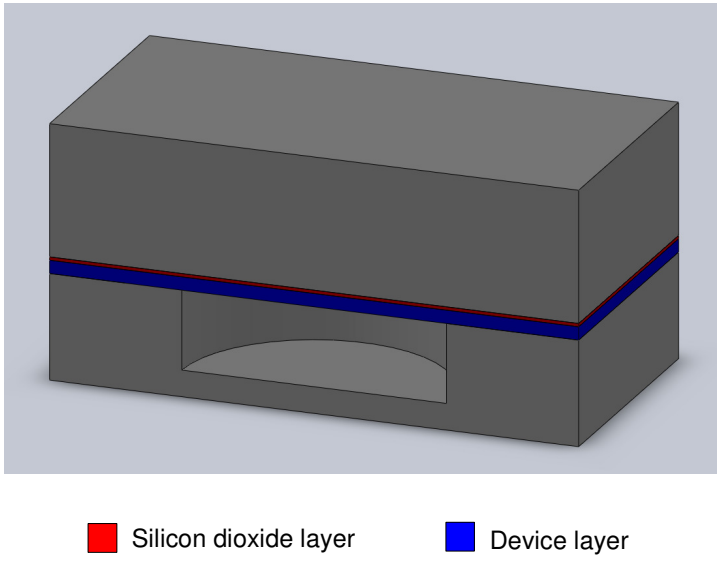

Figure 4- 6 Schematic drawing of test sample after silicon fusion bonding (cross-sectional view)

4.2.5 Wet etching

The wet chemical etching method used here aimed to remove the backside of the BESOI wafer, leaving the thin device layer on the silicon substrate. KOH is usually used as crystal orientation-dependent etchants of silicon [4-10]. The slowest etching planes are the {111} planes because those planes have the most dense atomic packing. Because the etch rate for (100) planes is much faster than for {111} planes, the etching creates the sidewalls at 54.74° to the wafer's surface for (100) silicon wafer. However, the whole handle layer of silicon was removed by this process.

Silicon dioxide is an amorphous material which etches equally well in all directions. Hydrofluoric acid (HF) solutions are used in the MEMS technology to etch the silicon dioxide film on top of the bulk silicon [4-11]. Because HF solutions etch silicon only very slowly, it can be assumed that the etching process stops on the silicon of the device layer. Therefore, the thickness of the silicon diaphragms could be controlled accurately.

The schematic drawing of the formed silicon diaphragm is shown in Figure 4- 7. Because the silicon dioxide layer was totally removed, the thermal stress which was induced in the silicon layer during the wafer bonding process was released. Therefore, there was no thermal stress in the ready-made silicon specimens.

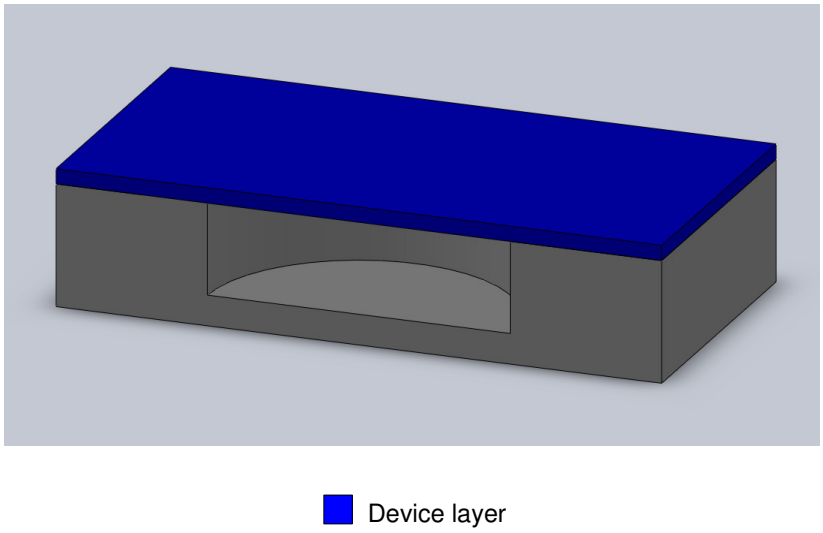

Figure 4- 7 Schematic drawing of formed silicon diaphragm sample (cross-sectional view)

4.2.6 Discussion of the micromachined test samples

The combination of lithography, deep reactive ion etching (DRIE) and silicon fusion bonding (SFD) produced vacuum cavities between bonded wafers. A photograph of the fabricated test samples on a wafer is shown in Figure 4- 8. A silicon diaphragm with the radius of 2.5mm is depicted in the rectangular box. The diaphragms deformed toward the substrate due to the atmospheric pressure. Since the wafer surface was highly reflective, only a few of the deformed diaphragms can be seen clearly.

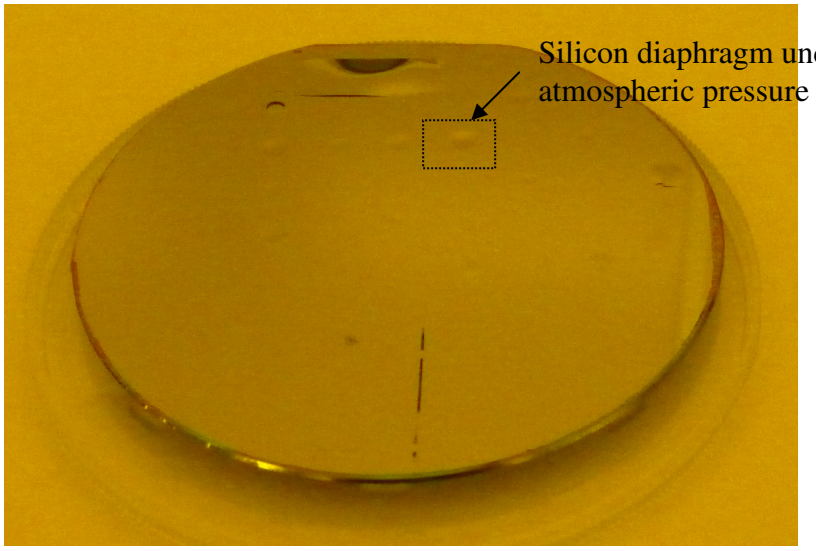

Figure 4- 8 Photograph of a silicon wafer with the test samples (The photos were taken in the clean room lithography area where the light appeared yellow)

The availability of the wet etching method and the BESOI wafers allowed good control over diaphragm thickness. Figure 4- 9 shows the SEM micrograph of the cross section for a microfabricated test sample. It can be seen that the thickness of the silicon device layer is uniform; the sidewall of the etched cavity is nearly vertical.

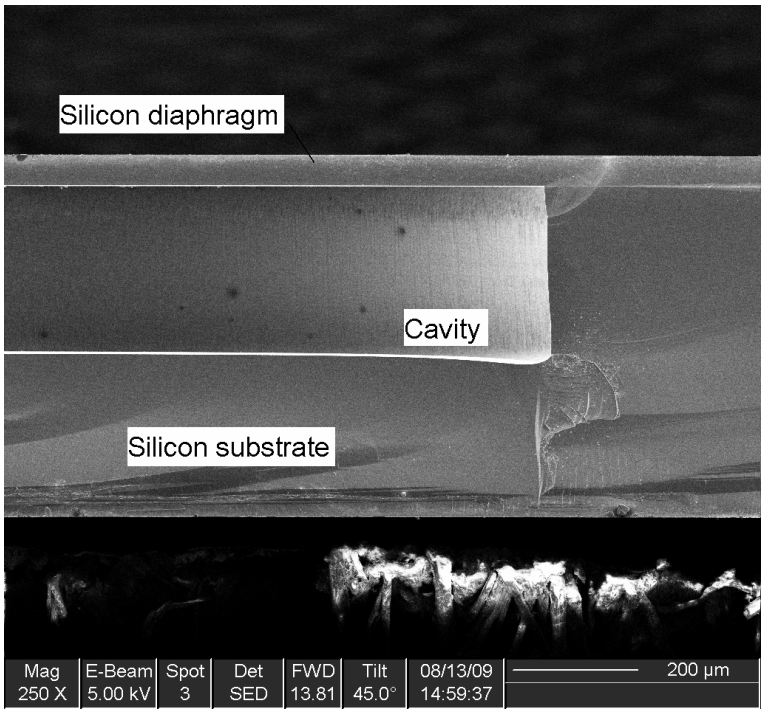

Figure 4- 9 SEM image of a microfabricated test sample (cross-sectional view)

However, the manufacturing processes are not ideal. The boron dopant would introduce internal stress in the silicon diaphragms [4-12]. The air may be trapped inside the cavities during the wafer bonding process. And the temperature may not be evenly distributed during the high temperature anneal. These fabrication imperfections could have an effect on the mechanical behaviour of the silicon diaphragms. Therefore, they need to be considered when the experimental data is evaluated.

4.3 *The experimental procedures and settings*

The mechanical behaviour of silicon diaphragms depends on the properties of single crystal silicon as a function of temperature, as shown in Figure 4- 10. At low temperature, silicon is brittle. So silicon diaphragms deform elastically under external load before fracture. Since single crystal silicon becomes ductile and is susceptible to

creep at elevated temperatures, silicon diaphragms are likely to deform plastically under external load.

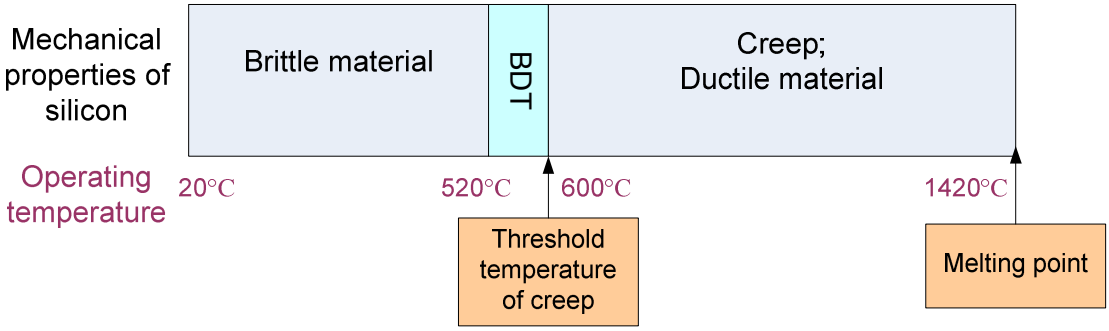

Figure 4- 10 mechanical properties of single crystal silicon as a function of temperature (BDT stands for brittle ductile transition) [4-13]

The experiment takes advantage of the diaphragm behaviour at different temperatures. The schematic representation of the experimental procedure is shown in Table 4- 1. The diaphragm behaviour at each step is also predicted according to silicon properties. After the test samples were made, they were exposed to atmosphere. So the surface profiles were firstly measured by Zygo NewView 5000^{TM}, a non-contact scanning white light interferometer [4-14]. The samples were imaged by using 5× objective lens, acquiring images in a grid array, which were subsequently stitched together. The resolution of the measurement system was set to 'high' when the maximum diaphragm deflection was in the range from 0 to 100μm. If the maximum deflection of the diaphragm was over 100μm, the resolution of the measurement system was set to 'low'. The Talymap software was then employed for the analysis of the profile data [4-15]. The measurement was conducted at a laboratory temperature of 20°C in the Wolfson School of Mechanical and Manufacturing Engineering at Loughborough University.

Table 4- 1 Schematic representation of experimental procedure

Procedures	Schematic drawing of test samples	Diaphragm behaviour
i)Surface profile measurement 1: Atmospheric pressure at 20°C;	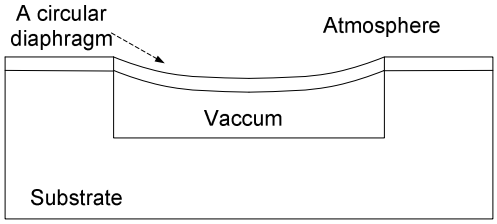	Elastic deformation;
ii)Anneal stage A: One atmospheric pressure at anneal temperature for designated anneal time*	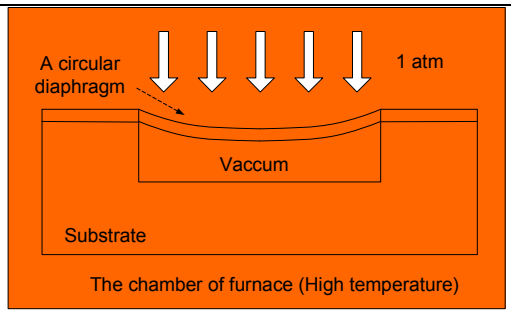	Elastic deformation; Possible plastic deformation**; Creep
iii) Surface profile measurement 2: Atmospheric pressure at 20°C;	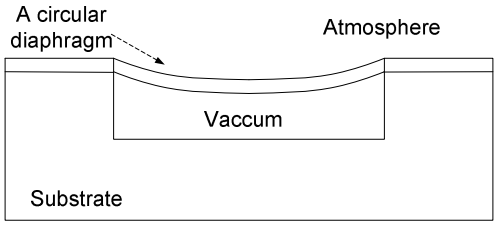	Elastic deformation; Possible permanent deformation in anneal stage A;
iv) Anneal stage B: One atmospheric pressure at anneal temperature for designated anneal time*	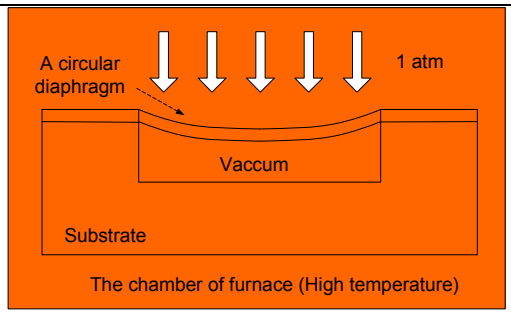	Elastic deformation; Possible plastic deformation** ; Creep; Possible permanent deformation in anneal stage A;
v) Surface profile measurement 3: Atmospheric pressure at 20°C;	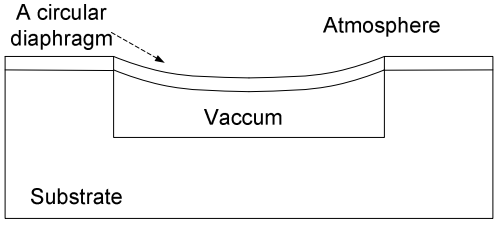	Elastic deformation; Possible permanent deformation in anneal stage A and B;

vi) Anneal stage C: One atmospheric pressure at anneal temperature for designated anneal time*	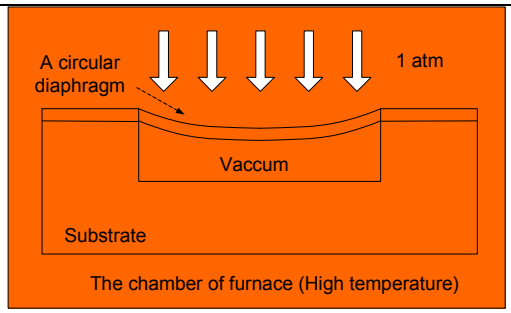	Elastic deformation; Possible plastic deformation** ; Creep; Possible permanent deformation in anneal stage A and B;
vii) Surface profile measurement 4: Atmospheric pressure at 20°C;	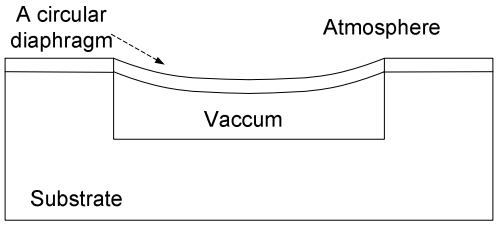	Elastic deformation; Possible permanent deformation in anneal stage A, B and C;

*The anneal temperature and time are specified in Table 4- 2 .

**Plastic deformation occurs if the resolved shear stress in the diaphragm exceeds the critical value.

Table 4- 2 Anneal time and temperatures

Anneal temperature	Anneal time (hour)		
	Stage A	Stage B	Stage C
600°C	1	68	68
800°C	1	15	15
900°C	1	10	10

The test samples were then placed in the furnace tube and were annealed under one standard atmospheric pressure. The anneal time for each stage is dependent on anneal temperature, and is specified in Table 4- 2. After anneal stage A, the surface profiles

of test samples were measured again under the atmospheric pressure at 20°C (surface profile measurement 2). Because single crystal silicon becomes brittle again during the measurement, the silicon diaphragms deform elastically under the applied pressure. However, the plastic deformation and creep deformation is permanent. The measured deformation will consist of any plastic deformation which has occurred in anneal stage A.

Therefore, it is possible to determine the diaphragm behaviour during the anneal stage A by comparing the surface profiles obtained from the measurement 2 with those obtained from the measurement 1. For each silicon diaphragm, if the surface profile 2 is the same as the surface profile 1, it can be concluded that no plastic deformation occurs during the anneal stage A; if the surface profile 2 is different from the surface profile 1, it can be concluded that plastic deformation or creep occurs during the anneal stage A, and the magnitude of the deformation can be obtained by subtracting the surface profile 1 from the surface profile 2.

In addition to the anneal stage A, the test samples had to go through the anneal stages B and C in order to investigate the effect of the anneal time. The surface profiles of the test samples were measured after each annealing process (surface profile measurement 3 and 4). Therefore, the diaphragm behaviour during annealing can be obtained by comparing the surface profiles before and after annealing.

4.4 *The mechanical behaviour of silicon diaphragms under atmospheric pressure*

After the test samples were made, the surface profiles of the silicon diaphragms were firstly measured under atmospheric pressure at 20°C. For each diaphragm size, three test samples were measured on each silicon wafer. So twelve surface profiles were obtained from four silicon wafers with the silicon resistivity of 0.001ohm-cm, while fifty surface profiles were obtained from five wafers with the silicon resistivity over 1000ohm-cm. The surface profile of a lightly doped silicon diaphragm (resistivity of 0.001ohm-cm) under the air pressure of 100, 840 Pa is plotted in Figure 4- 11. It can be seen that the deflection profile is axisymmetrical. The maximum deformation is found to be 37.41μm at the diaphragm centre.

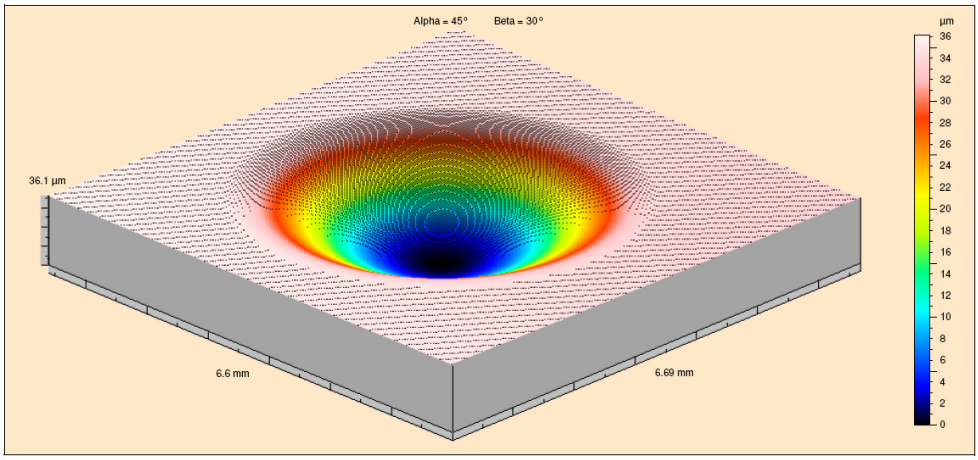

Figure 4- 11 3D surface profile of a silicon diaphragm (resistivity of 0.001ohm-cm) with the radius of 2.5mm

The diaphragm deflection is linearly proportional to the applied pressure (Equation 3-3 in section 3.3.1). The magnitude of the atmospheric pressure relates to the weather and varies from day to day. According to the recorded data in Figure 4- 12, the pressure fluctuation is as small as 3%. So it would not make a big difference in the

diaphragm behaviour. However, in order to analyze the data precisely, all the measured results were adjusted to the condition of one standard atmospheric pressure (101, 325Pa).

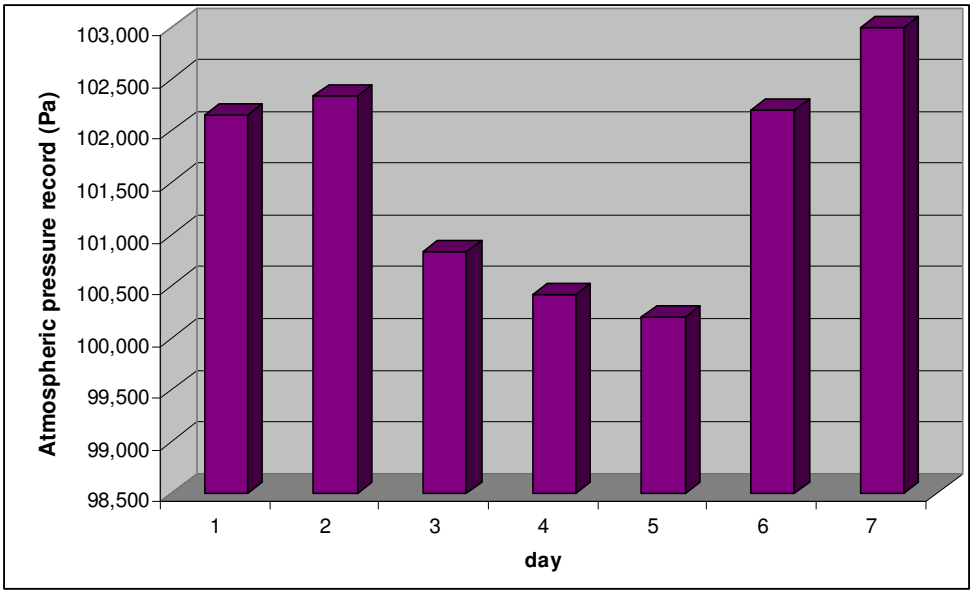

Figure 4- 12 Atmospheric pressure record

The diaphragm deflections are studied statistically and are plotted as a function of the diaphragm radius in Figure 4- 13. The maximum deformation for the diaphragm with a radius of 0.5mm is about 100nm. With increasing radius, the diaphragm deflection increases. When the radius is 2.5mm, the average maximum deflection is 36.71μm for highly doped silicon diaphragms, while it is 34.83μm for lightly doped silicon diaphragms.

The deformation predicted by the 3D orthotropic FEA model (Table 3-5 in section 3.3.6) is also plotted in Figure 4- 13. It can be seen that the measured deformations are very close to the predicted values. Since the mechanical properties of pure silicon

are used in the FEA model, the predictions slightly underestimate the deflections of the boron doped silicon diaphragms.

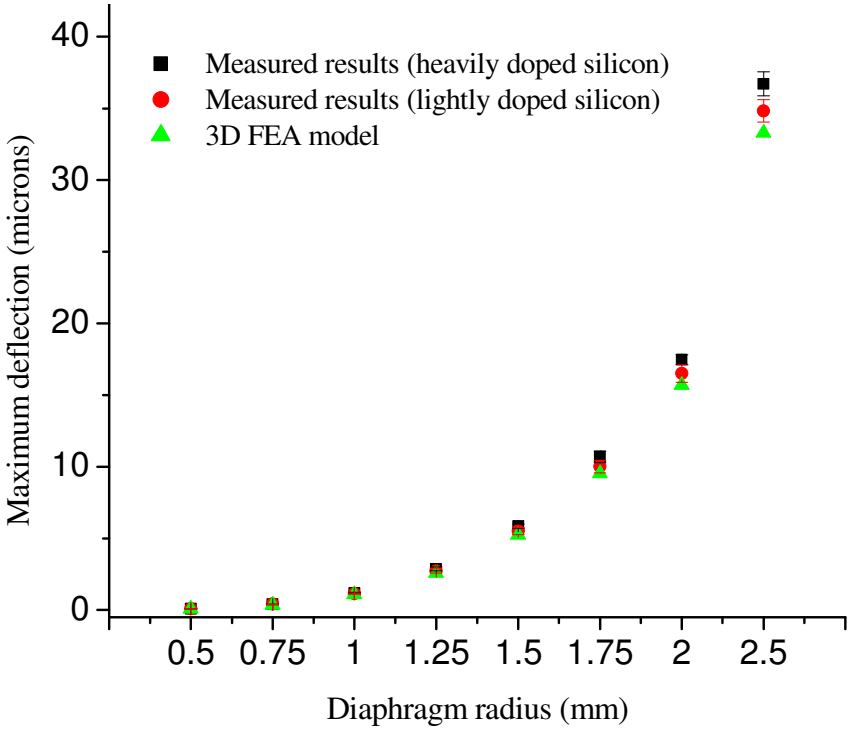

Figure 4- 13 Maximum deflection as a function of diaphragm radius

4.5 *The mechanical behaviour of silicon diaphragms at elevated temperatures*

For the heavily doped silicon diaphragms (the resistivity of 0.001ohm-cm), the mechanical behaviour at 600°C, 800°C and 900°C is reported here.

4.5.1 The mechanical behaviour at 600℃

One silicon wafer with test samples was annealed at 600°C. There was no temperature ramp in the furnace, and nitrogen gas at atmospheric pressure was applied to the

silicon diaphragms. Each sample was annealed for 1 hour (stage A), 68 hours (stage B) and 68 hours (stage C) separately, as illustrated in Figure 4- 14. So after the anneal stage B, the test samples had been annealed for 69 hours; and after the anneal stage C, the test samples had been annealed totally for 137 hours. The test samples on one wafer after anneal stage A is shown in Figure 4- 15.

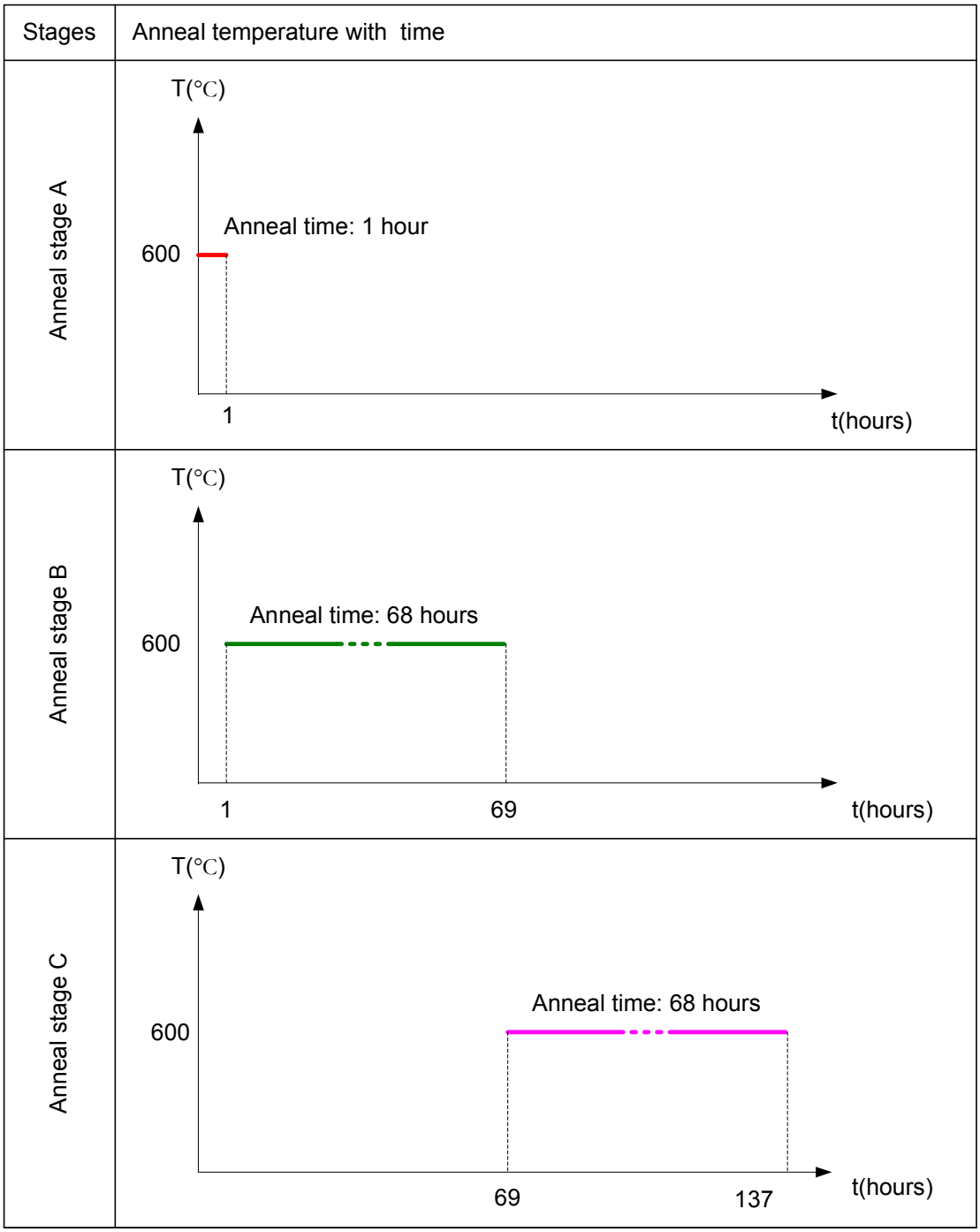

Figure 4- 14 The annealing temperature at 600°C as a function of time

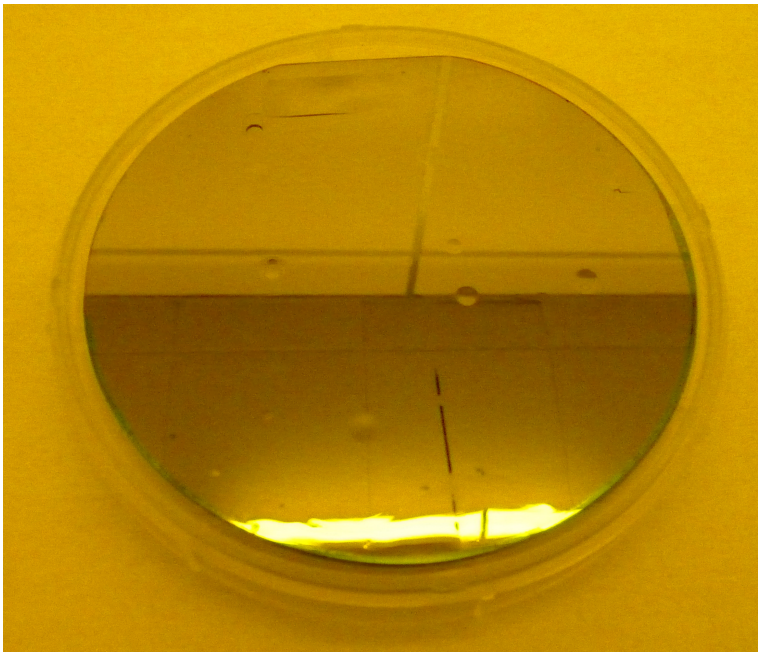

Figure 4- 15 The photo of the test samples on one wafer after anneal stage A at 600°C

Figure 4- 16 Top view optical microscope photo of a test sample (sample 2) with a radius of 2.5mm after annealing at 600°C for 137 hours

The shape of the distorted diaphragms after annealing for 137 hours can be seen clearly with the microscope. The surface of the test sample 2 for the diaphragm with a radius of 2.5mm is shown in Figure 4- 16. Unlike the axisymmetrical surface profile

before anneal (see Figure 4- 11), the deformed shape after long time annealing appeared to be unsymmetrical.

The surface profiles along the diameter of the deformed diaphragms were measured. The data of three test samples was taken for each diaphragm radius. When the radius is equal to 2.5mm, the three test samples showed three different behaviours. The cross section of the surface profiles are shown in Figure 4- 17. For the test sample 1, the maximum deflection changed continuously from 37.51μm before anneal, to 44.41μm after the anneal stage C; but showed a noticeable increase during the anneal stage B. For the test sample 2, the maximum deflection changed slightly from 36.02μm to 41.55μm during the anneal stage B, but increased dramatically to 78.37μm after the anneal stage C. For the test sample 3, the maximum deflection increased slightly during the anneal stage A, then changed noticeably from 36.89μm to 101.30μm during the anneal stage B, and almost kept the same during the anneal stage C.

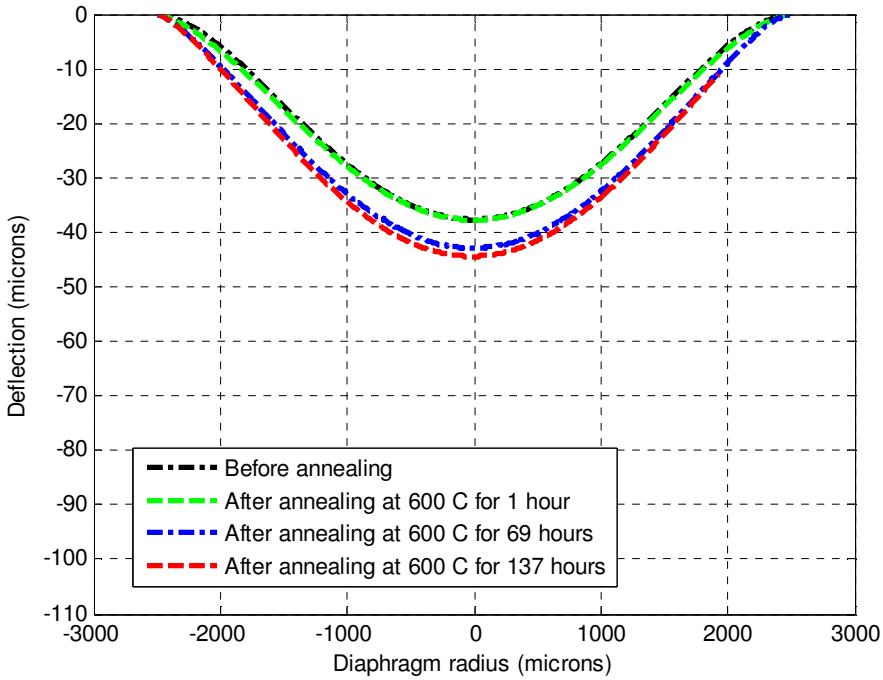

(a) Test sample 1

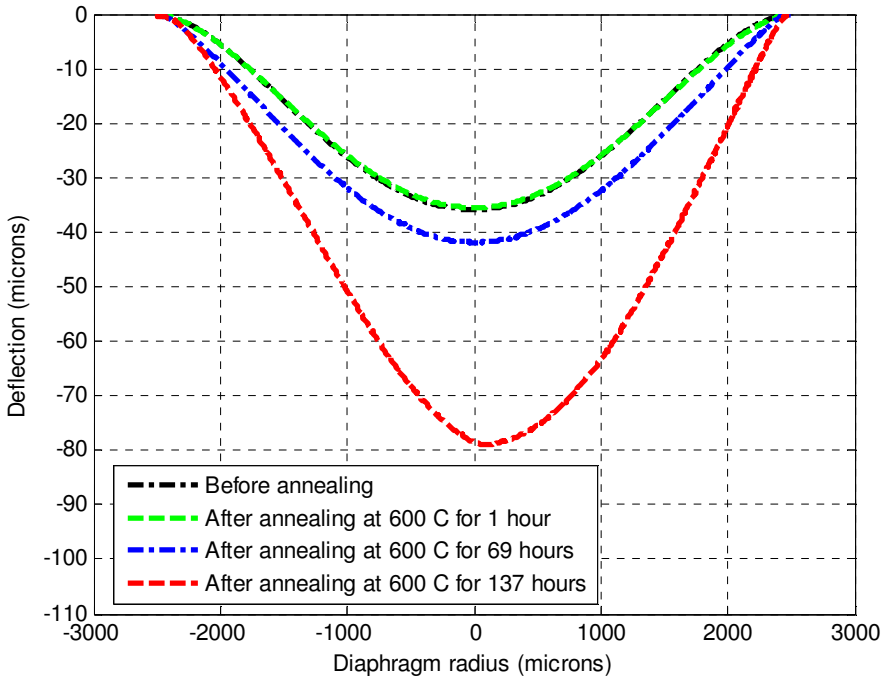

(b) Test sample 2

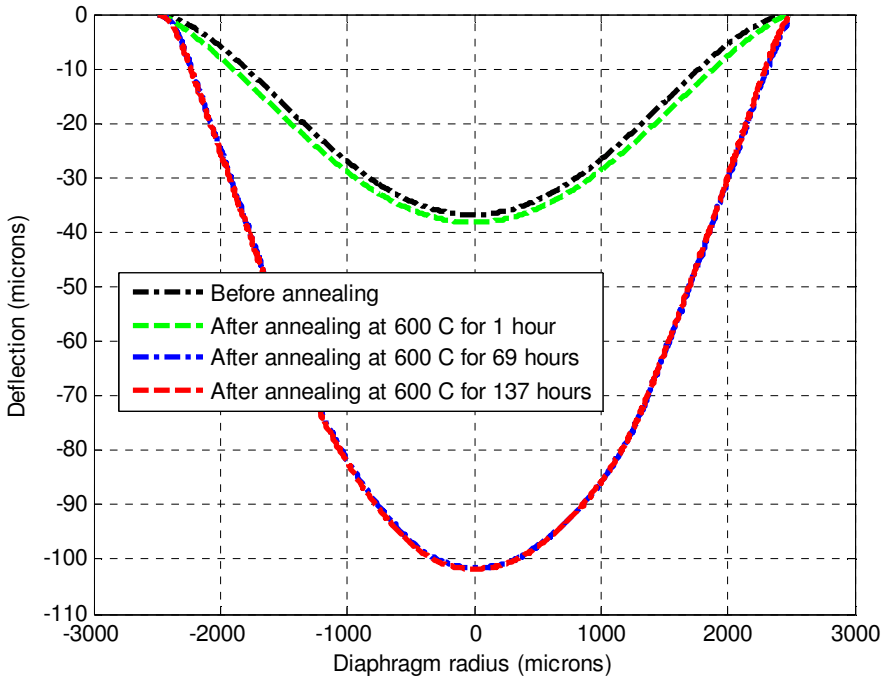

(c) Test sample 3

Figure 4- 17 the cross section of the surface profiles for the diaphragms with a radius of 2.5mm with respect to the annealing processes at 600°C: after anneal stage A (after annealing for 1 hour), after anneal stage B (after annealing for 69 hours), and after anneal stage C (after annealing for 137 hours) .

For the three tested samples with a radius of 2.5mm, the deformations before anneal are quite similar, and there was no apparent increase for the deflections in the anneal stage A. So the deformation at later anneal stage is caused by creep. However the creep rate is very different. When all the three samples are located close to the wafer centre, the variation of the creep rate can be caused by the annealing temperature and the manufacturing imperfections (as discussed in section 4.2.6). According to Figure 4- 10, the annealing temperature of 600°C is just at the creep threshold temperature of silicon. Therefore, any differences among the samples which are caused by the manufacturing imperfections could either speed up or slow down the process of creep.

It is known from section 4.4 that the magnitude of the diaphragm deflection decreases with the diaphragm radius. In order to analyse the data precisely, the measured diaphragm deflections were adjusted to the condition that one standard atmospheric pressure is applied. The maximum deflections with respect to the anneal time are listed in Table 4- 3.

Table 4- 3 The maximum deflections with respect to the anneal time (the anneal temperature: 600°C)

Radius (mm)		**Maximum deflections (μm)**			
		Before annealing	After annealing A	After annealing B	After annealing C
	Total annealing time	0 hour	1 hours	69 hours	137 hours
0.50	Sample 1	0.099	0.090	0.094	0.087
	Sample2	0.093	0.101	0.097	0.093
	Sample 3	0.089	0.101	0.095	0.091
	Average	0.094	0.097	0.095	0.090
0.75	Sample 1	0.378	0.386	0.378	0.380
	Sample2	0.392	0.395	0.385	0.386
	Sample 3	0.373	0.412	0.402	0.404
	Average	0.381	0.398	0.388	0.390
1.00	Sample 1	1.258	1.231	1.217	1.215
	Sample2	1.227	1.213	1.193	1.195
	Sample 3	1.258	1.233	1.206	1.215
	Average	1.247	1.226	1.205	1.208
1.25	Sample 1	2.845	2.803	2.781	2.748
	Sample2	2.810	2.817	2.802	2.788
	Sample 3	2.871	2.902	2.881	2.898
	Average	2.842	2.841	2.822	2.811
1.50	Sample 1	5.762	5.797	5.759	5.795
	Sample2	5.825	5.784	5.805	5.755
	Sample 3	5.820	5.831	5.777	5.775
	Average	5.803	5.804	5.780	5.775
1.75	Sample 1	10.717	10.787	10.725	10.654
	Sample2	10.753	10.815	10.731	10.654
	Sample 3	10.649	10.666	10.588	10.555
	Average	10.706	10.756	10.681	10.621
2.00	Sample 1	17.232	17.354	17.326	17.426
	Sample2	17.408	17.695	18.207	18.421
	Sample 3	17.457	17.578	17.967	18.123
	Average	17.366	17.542	17.833	17.990
2.5	Sample 1	37.514	38.345	42.597	44.410
	Sample2	35.748	36.022	41.552	78.365
	Sample 3	36.893	38.004	101.303	101.566
	Average	36.718	37.457	61.817	74.780

In order to compare the deflections obtained from different anneal stages, the data is averaged and is plotted in Figure 4- 18 (a) and (b). It can be seen that when the radius

is 2mm and under, there is no measurable differences among the diaphragm deflections. So the deformation under the atmospheric pressure at 600°C is elastic, and the creep deformation can be ignored when the anneal time is less than 137 hours. When the radius is 2.5mm, creep deformation occurred, and the amount of the creep deformation could be significant.

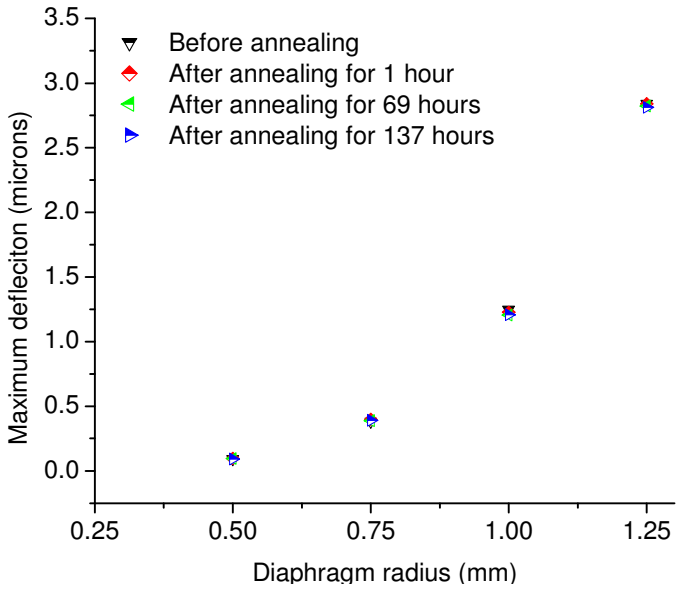

Figure 4- 18 (a) average of the maximum deflections with respect to anneal time (anneal temperature: 600°C, diaphragm size: 0.5mm-1.25mm)

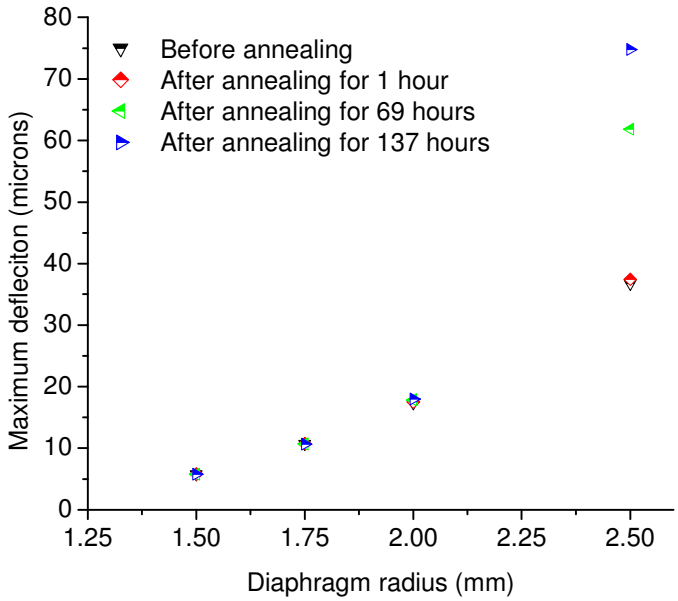

Figure 4- 18 (b) Average of the maximum deflections with respect to anneal time (anneal temperature: 600°C, diaphragm size: 1.5mm-2.5mm)

4.5.2 The mechanical behaviour at 800°C

One silicon wafer with test samples was annealed at 800°C. Nitrogen gas at atmospheric pressure was applied to the silicon diaphragms. Each sample was annealed for 1 hour (stage A), 15 hours (stage B) and 15 hours (stage C) separately, as shown in Figure 4- 19. At each anneal stage, the furnace temperature rose from 600°C with the ramp-up rate of temperature 5°C/min, and then was maintained at 800°C for the desired anneal time, After that the furnace was cooled down gradually to 600°C with the ramp-down rate of temperature -5°C/min. Therefore, the test samples had been annealed at 800°C for 16 hours after the anneal stage B, and had been annealed at 800°C for 31 hours after the anneal stage C.

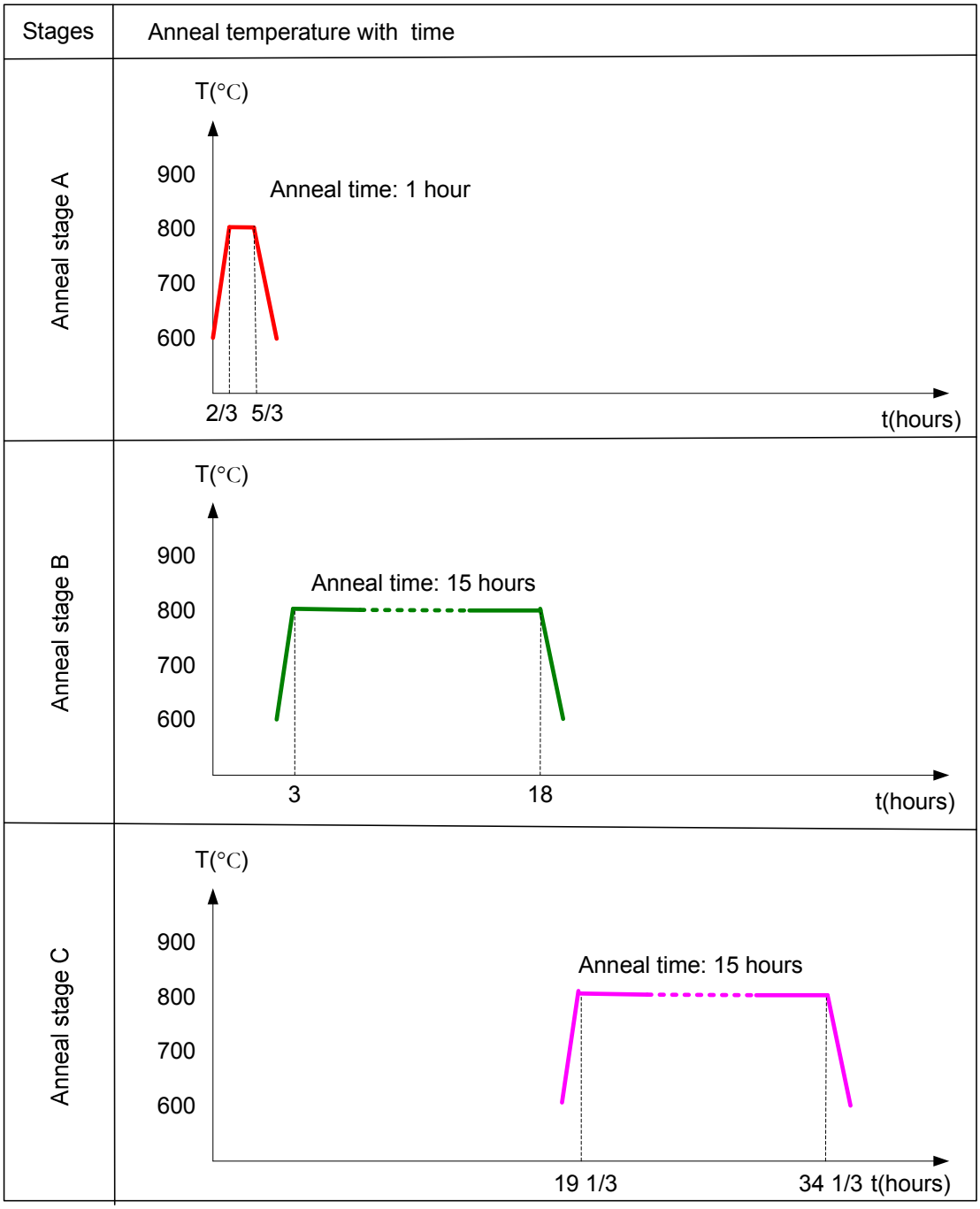

Figure 4- 19 The temperature as a function of time when anneal at 800°C

The test samples on one wafer after anneal stage A is shown in Figure 4- 20. Unlike the test samples before anneal (see Figure 4- 8), the deformed shape of some large diaphragms is clear.

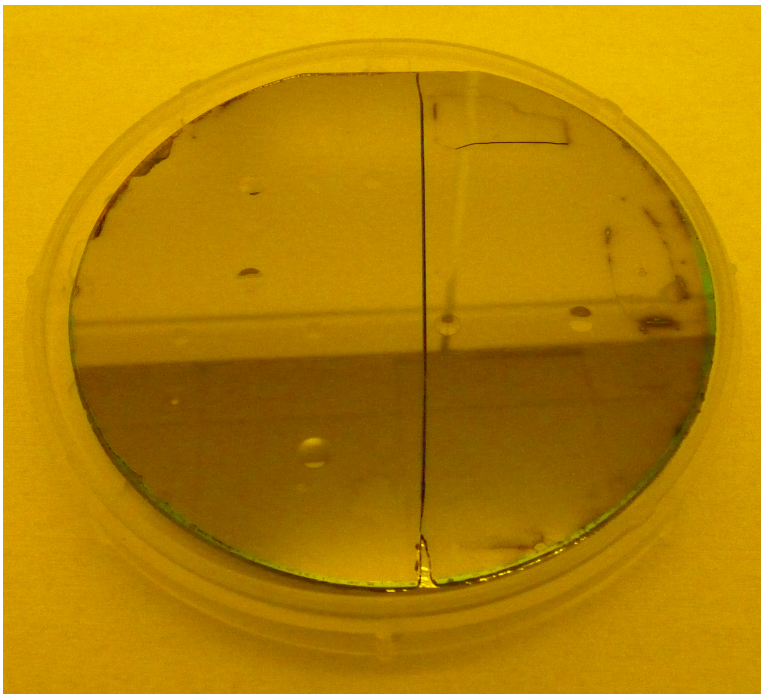

Figure 4- 20 The photo of the test samples after anneal stage A at 800°C

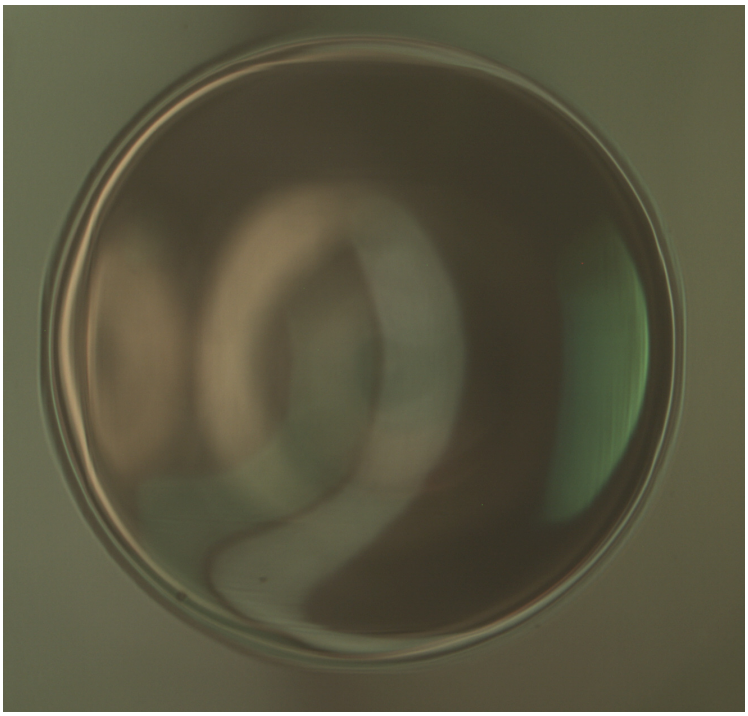

Figure 4- 21 Top view optical microscope photo of diaphragm with a radius of 2.5mm after anneal 800°C for 31 hours (sample 1)

The shapes of the deformed diaphragms after anneal stage C can be seen clearly by the microscope. The surface of the test sample 1 for the diaphragm with a radius of 2.5mm is shown in Figure 4- 21**.** The edge of the diaphragm is somewhat distorted due to the slip of the dislocations under stress.

The cross sections of the surface profiles with respect to the anneal stages are shown in Figure 4- 22. It can be seen that the diaphragm deflection increased noticeably from 36.59μm to 107μm during the anneal stage A, and then stayed almost the same during the anneal stage B and C (the small differences are caused by the measurement error). It is known that the anneal period of the stage A is very short compared with the total anneal time. So it is the plastic deformation that primarily contributes to the deflection increase, and the creep effect at later anneal stages is not obvious.

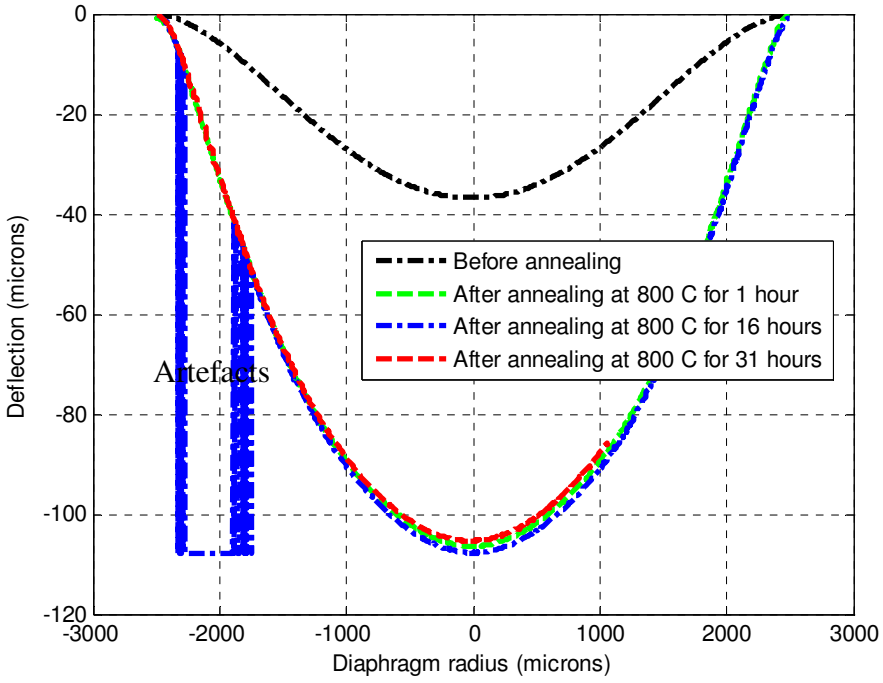

Figure 4- 22 the cross section of the surface profiles for the diaphragms with a radius of 2.5mm with respect to the anneal stages at 800°C (sample 1): after anneal stage A (after annealing for 1 hour), after anneal stage B (after annealing for 16 hours), and after anneal stage C (after annealing for 31 hours) .

In Figure 4- 22, the deformed shape after anneal stage B was so steep that the slope of the surface profile went beyond the measurement limit of the white light interferometer. As a result, artefacts appeared in the data as sharp valleys at the steepest region near the diaphragm edge (illustrated by the blue line). In order to avoid invalid measurement data, only half of the surface profile was measured for the sample after anneal stage C (red line). However, the data is adequate to identify the evolution of the diaphragm deflection through annealing processes.

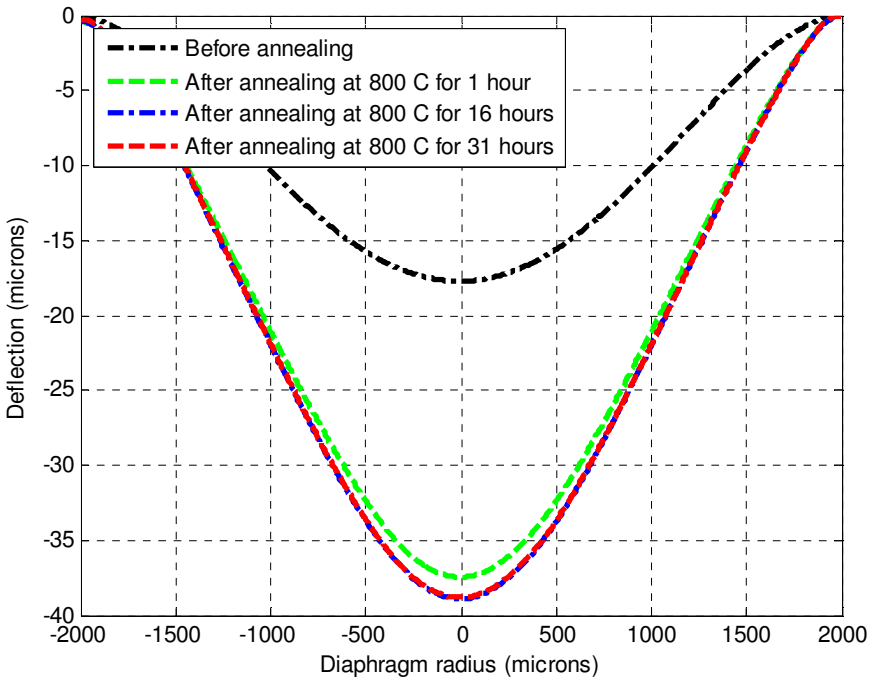

Figure 4- 23 the cross section of the surface profiles for the diaphragm with a radius of 2.0mm with respect to the annealing process at 800°C (sample 2): after anneal stage A (after annealing for 1 hour), after anneal stage B (after annealing for 16 hours), and after anneal stage C (after annealing for 31 hours) .

The evolution of the diaphragm profiles for the test samples with a radius of 2mm and 1.75mm are shown in the Figure 4- 23 and Figure 4- 24. For the diaphragm with a radius of 2mm (sample 2), the deflection increased noticeably from 17.6μm to 37.9μm during the anneal stage A. The diaphragm deformed slightly during the anneal stage B,

and hardly deflected during the anneal stage C. For the diaphragm with a radius of 1.75mm (sample 3), the deflection increased slightly during the anneal stage A and increased noticeably from 12.4μm to 15.5μm during the anneal stage B. Similar to the sample 2 with a radius of 2mm, the test sample 3 with a radius of 1.75mm hardly deflected during the anneal stage C.

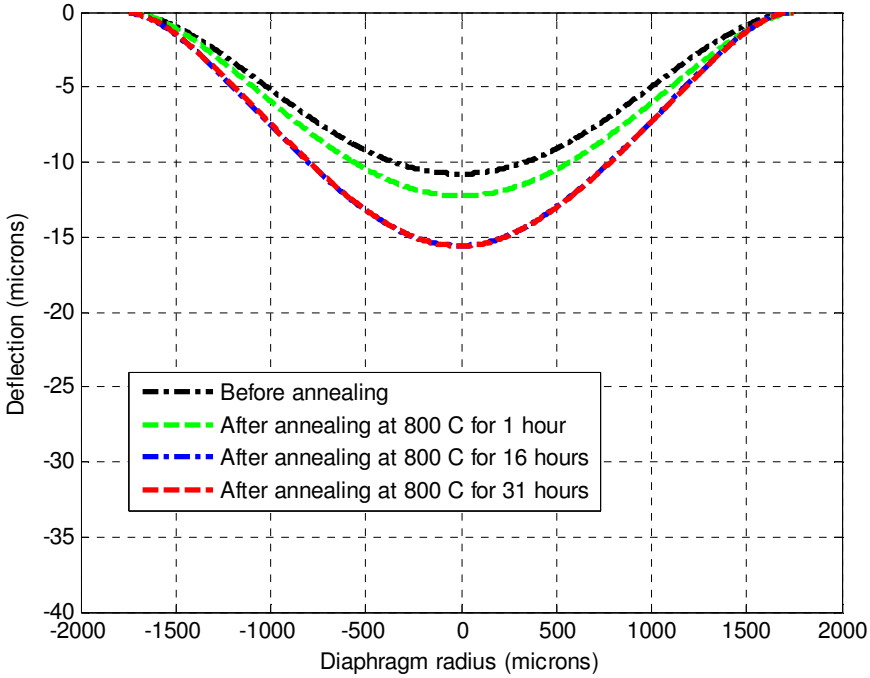

Figure 4- 24 the cross section of the surface profiles for the diaphragm with a radius of 1.75mm with respect to the annealing process at 800°C (sample 3): after anneal stage A (after annealing for 1 hour), after anneal stage B (after annealing for 16 hours), and after anneal stage C (after annealing for 31 hours) .

The maximum deflections for each diaphragm radius with respect to the anneal time are listed in Table 4- 4.

Table 4- 4 The maximum deflections with respect to the anneal time

(the anneal temperature: 800°C)

Radius		**Maximum deflections (μm)**			
(mm)		Before annealing	After annealing A	After annealing B	After annealing C
	Total annealing time	0 hour	1 hours	16 hours	31 hours
0.50	Sample 1	0.091	0.087	0.085	0.087
	Sample2	0.078	0.075	0.073	0.077
	Sample 3	0.092	0.094	0.094	0.100
	Average	0.087	0.086	0.084	0.088
0.75	Sample 1	0.388	0.392	0.382	0.379
	Sample2	0.357	0.375	0.380	0.388
	Sample 3	0.380	0.367	0.388	0.392
	Average	0.375	0.378	0.383	0.386
1.00	Sample 1	1.151	1.150	1.157	1.164
	Sample2	1.149	1.146	1.149	1.154
	Sample 3	1.148	1.132	1.162	1.174
	Average	1.149	1.143	1.156	1.164
1.25	Sample 1	2.947	2.941	2.892	2.905
	Sample2	2.919	2.814	2.913	2.915
	Sample 3	2.820	2.843	2.827	2.836
	Average	2.895	2.866	2.877	2.886
1.50	Sample 1	5.940	5.996	6.055	6.090
	Sample2	5.961	6.145	6.147	6.169
	Sample 3	5.806	5.863	5.879	5.910
	Average	5.902	6.001	6.027	6.056
1.75	Sample 1	10.433	11.493	12.030	12.040
	Sample2	11.227	11.910	12.960	13.035
	Sample 3	10.710	12.376	15.482	15.522
	Average	10.790	11.926	13.491	13.532
2.00	Sample 1	17.622	38.030	38.655	38.607
	Sample2	17.591	37.859	38.705	38.706
	Sample 3	17.339	37.816	38.194	38.209
	Average	17.517	37.902	38.518	38.507
2.50	Sample 1	36.591	107.089	107.682	107.462
	Sample2	35.219	57.881	57.946	58.209
	Sample 3	37.588	111.412	112.510	112.437
	Average	36.466	92.127	92.713	92.703

In order to compare the deflections obtained from different anneal stages, the data is averaged and are plotted in Figure 4- 25. It can be seen that when the radius is 1.5mm and under, there is no measurable difference among the diaphragm deflections at each anneal stage. So the plastic deformation and the creep effect can be ignored when the anneal time is less than 31 hours. For the diaphragms with the radius of 1.75mm and above, the deflections increased apparently during the annealing process A for 1 hour. Because the annealing duration of the anneal stage A is very short comparing with the

total anneal time (31 hours), it can be concluded that it is the plastic deformation that contributes to the dramatic increase of the deflection. The creep deformation was noticed for the diaphragm with a radius of 1.75mm when the anneal time is less than 16 hours. For all the specimens, no measurable creep occurred when the anneal time is from 16 hours to 31 hours.

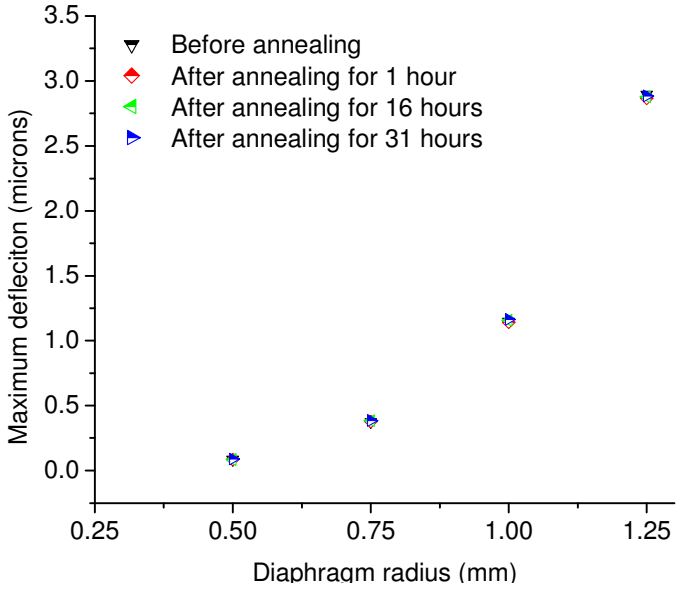

Figure 4- 25 (a) average of the maximum deflections with respect to the anneal time (the annealing temperature: 800°C, diaphragm size: 0.5mm-1.25mm)

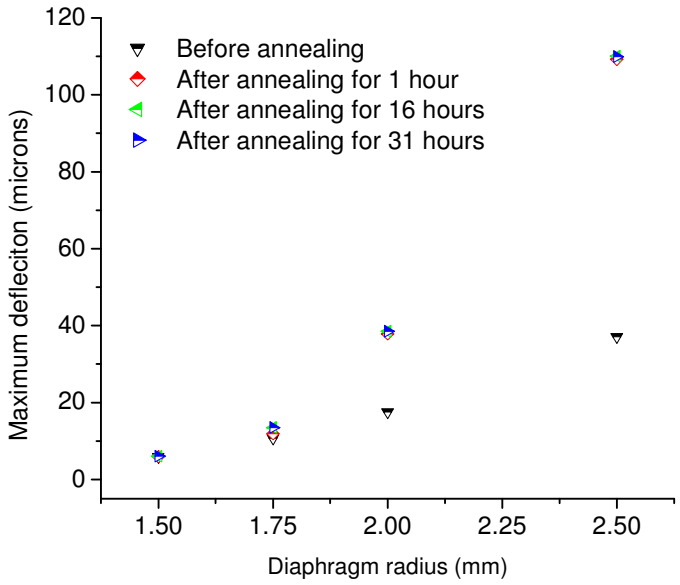

Figure 4- 25 (b) Average of the maximum deflections with respect to the anneal time (the annealing temperature: 800°C, diaphragm size: 1.5mm-2.5mm)

4.5.3 The mechanical behaviour at 900°C

One silicon wafer with test samples was annealed at 900°C. Nitrogen gas at atmospheric pressure was applied to the silicon diaphragms. Each sample was annealed for 1 hour (stage A), 10 hours (stage B) and 10 hours (stage C), as shown in Figure 4- 26. At each anneal stage, the furnace temperature rose from 600°C with the ramp-up rate of temperature 5°C/min, and then was maintained at 900°C for the desired anneal time, After that the furnace was cooled down gradually to 600°C with the ramp-down rate of temperature -5°C/min. Therefore, the test samples had been annealed at 900°C for 11 hours after the anneal stage B, and had been annealed at 900°C for 21 hours after the anneal stage C.

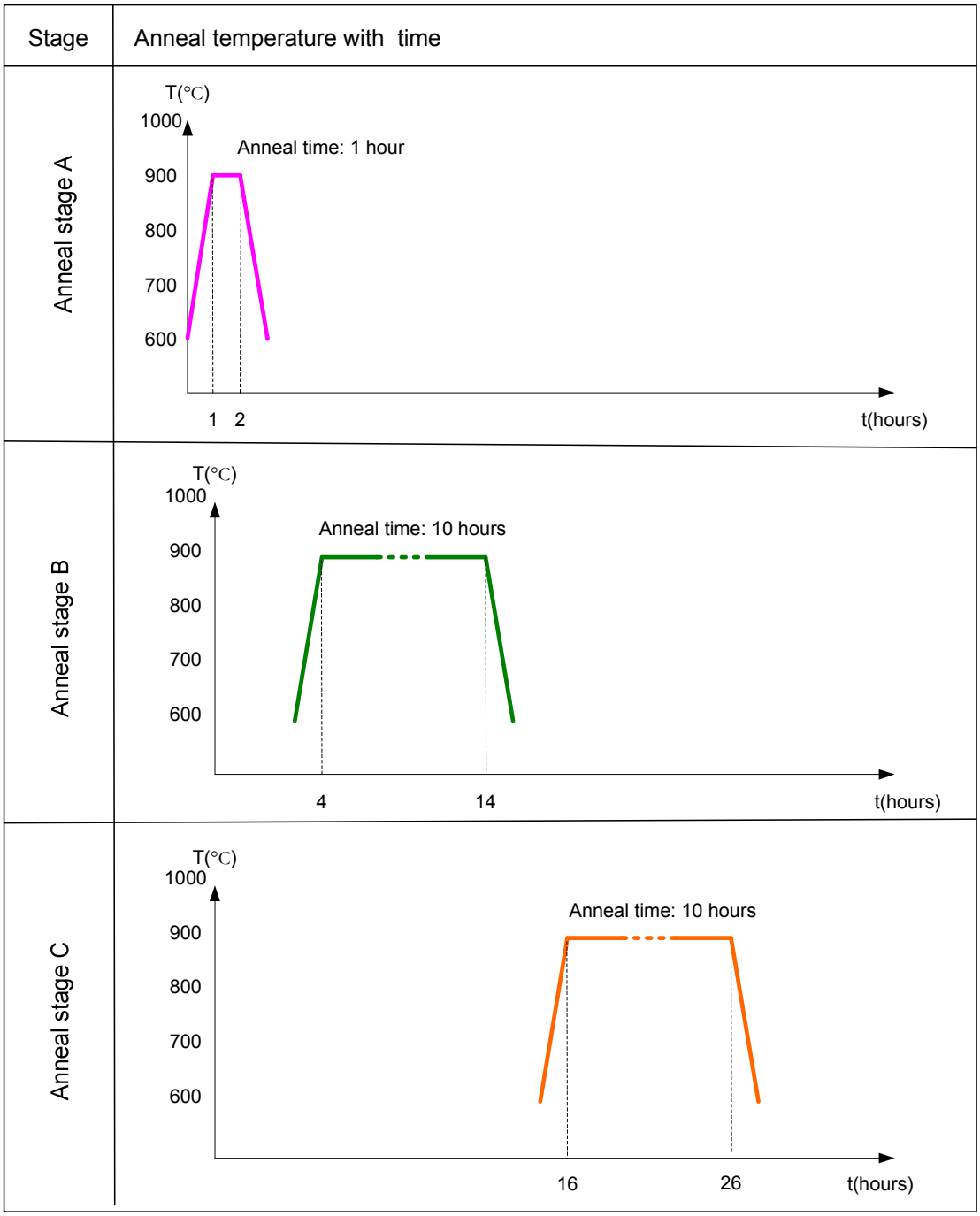

Figure 4- 26 The temperature as a function of time when annealing at 900°C

The test samples on one wafer after anneal stage A is shown in Figure 4- 27. Unlike the test samples before anneal (see Figure 4- 8), the deformed shapes of some large diaphragms are clear.

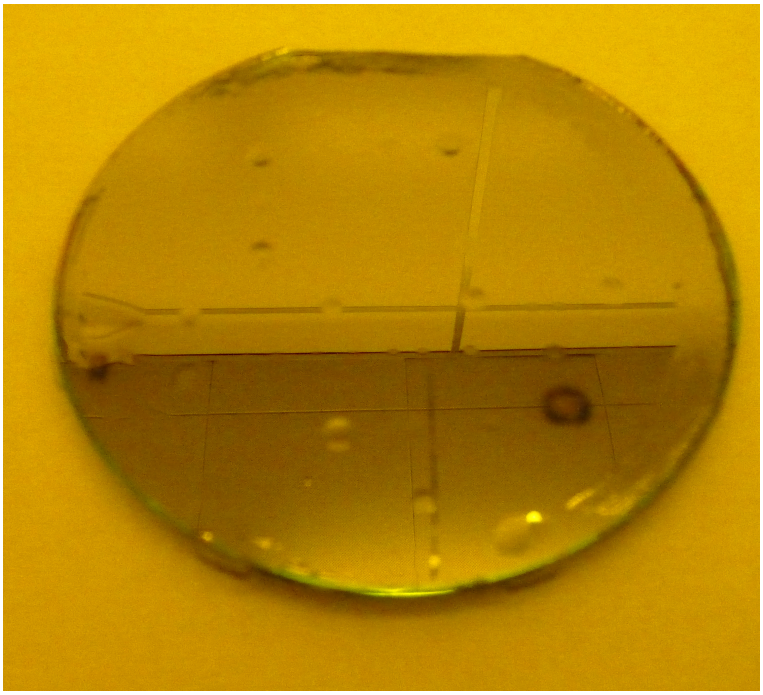

Figure 4- 27 The photo of the test samples after anneal stage A at 900°C

The microscopic photo of a deformed diaphragm (with a radius of 2.5mm) after being annealed for 21 hours is shown in Figure 4- 28. The slip bands on the diaphragm surface appear as bright or dark coloured lines by reflecting some of the light from the light source above the specimen, as shown in the enlarged photos (b) and (c). In the region a), a high density of the visible lines are oriented parallel to the [110] direction. In the region b), the visible lines are oriented parallel and perpendicular to the [110] direction. The different arrangement of the slip bands between the region a) and b) is caused by a different number of working slip systems. From section 3.2.4, it is known that there are 12 primary slip systems ({111} <110>) in silicon. The slip system would be activated wherever the resolved shear stress exceeds the critical value. Because silicon is orthotropic, the direction and the magnitude of the induced stress close to the side of the specimen (the region a)) are different from those close to the corner (the region b)). The photos suggest that the induced stress activates more slip systems on the diaphragm surface in the region b) than those in the region a).

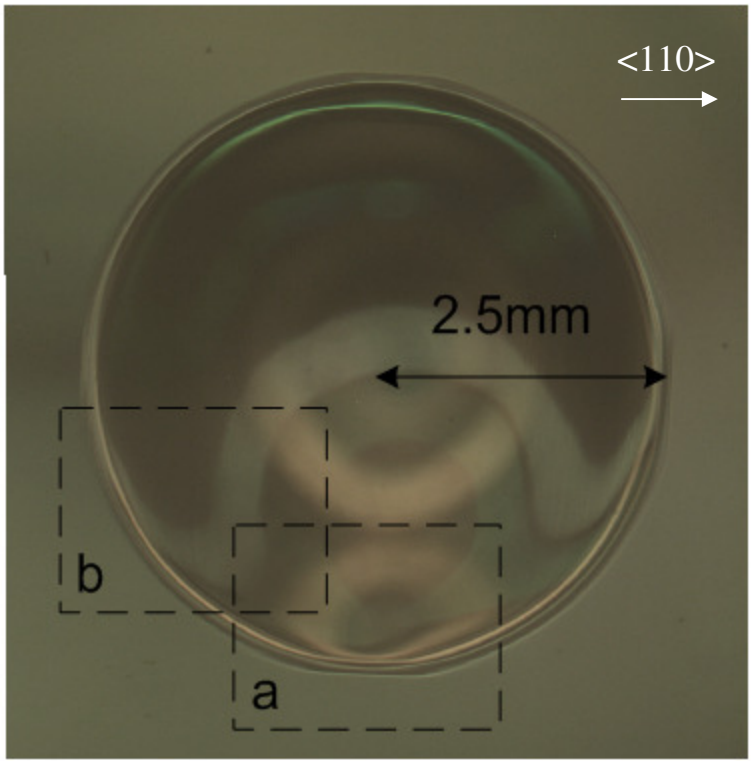

Figure 4- 28(a) Top view optical microscope photo of diaphragm with a radius of 2.5mm after annealing 900°C for 21 hours

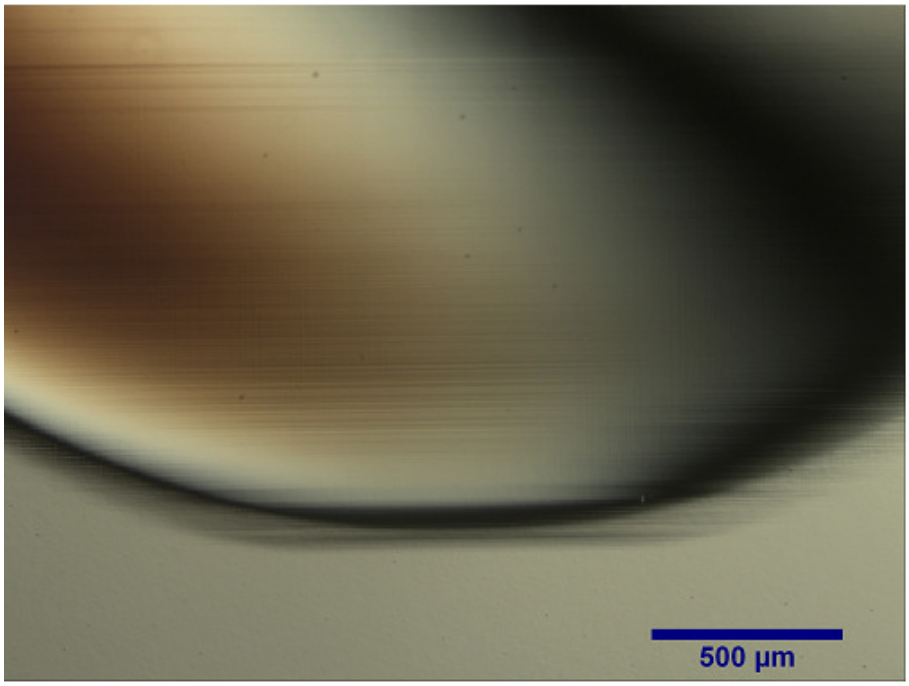

Figure 4- 28(b) Enlarged photo in the region a)

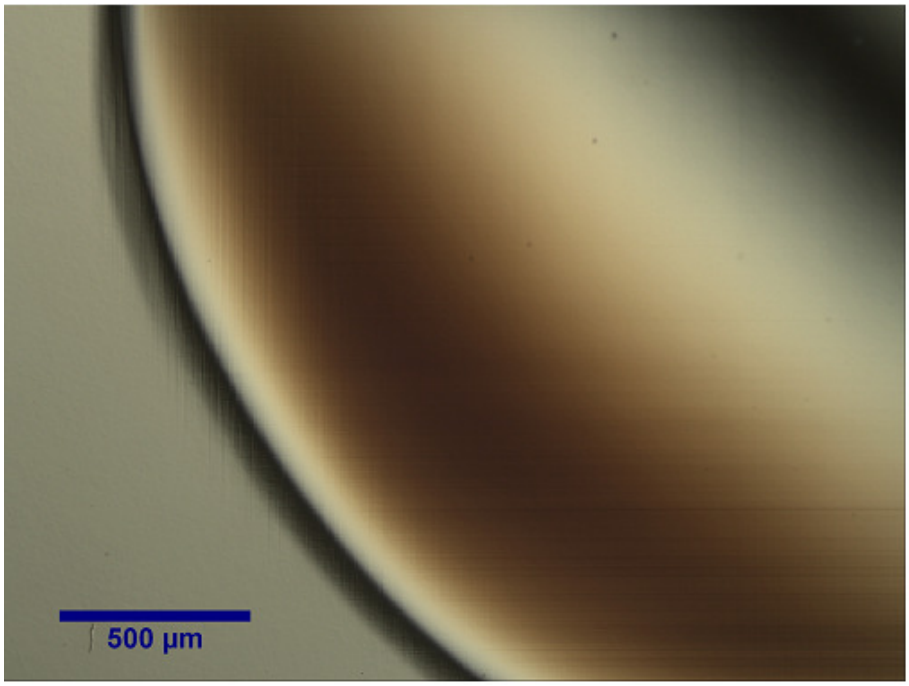

Figure 4- 28(c) Enlarged photo in the region b)

For the specimen shown in the Figure 4- 28, the cross sections of the surface profiles with respect to the anneal stages are shown in Figure 4- 29. The maximum elastic deformation before the anneal stage A was 36.35µm at the diaphragm centre. In the anneal stage A, the maximum deflection increased dramatically to 109.7µm. The average deformation rate was relatively high. This was because the number of the dislocations increased rapidly by Frank-Read sources [4-16], and the dislocation mobility was high. The Frank-Read mechanism is the most important mechanism for the generation of dislocations in the bulk of a crystal. It supposes that both ends of a dislocation line are firmly pined. Then when the shear force is applied on the slip plane, the dislocation line will bow out. And the movement of the dislocation line will form a complete dislocation loop and a new dislocation line between the pinned ends. The Frank-Read process can repeat again and again under sufficient load. Thus the dislocations could multiply rapidly in a very short time.

As the diaphragm deformed further in the anneal stage B, the interaction of the dislocations resisted the plastic flow. Therefore, the average deformation rate slowed down. Only an increase in deflection of 23.6μm was obtained in 10 hours. In the anneal stage C, the profiles show that the diaphragm deformation decreased about 3.7μm. Because the deflections after anneal stages B and C were greater than 100μm, the measurement resolution was set to 'low'. Only half of the surface profiles were obtained.

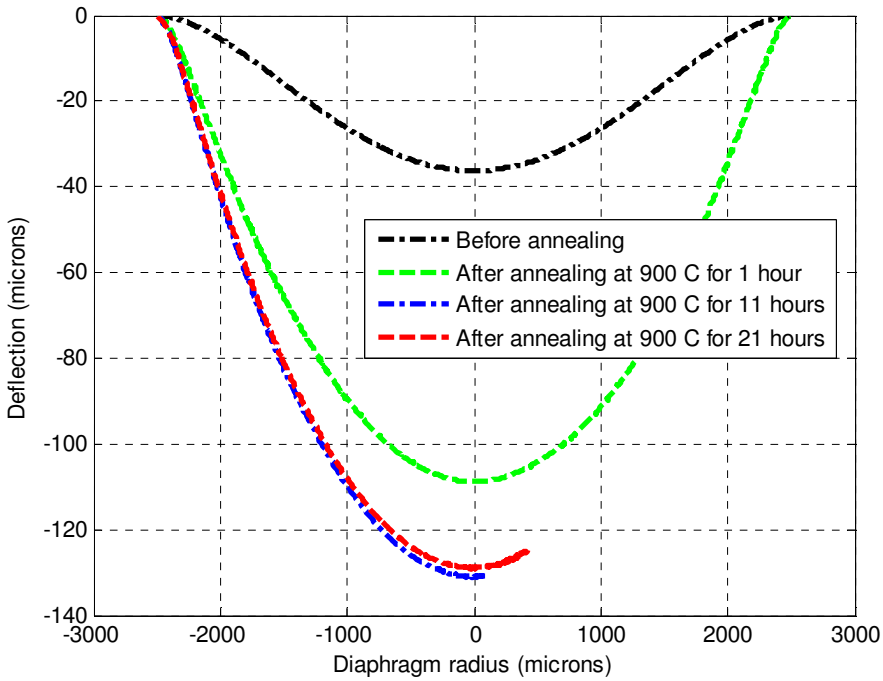

Figure 4- 29 the cross section of the surface profiles for the diaphragms with a radius of 2.5mm with respect to the annealing process at 900°C (sample 1): after anneal stage A (after annealing for 1 hour), after anneal stage B (after annealing for 11 hours), and after anneal stage C (after annealing for 21 hours) .

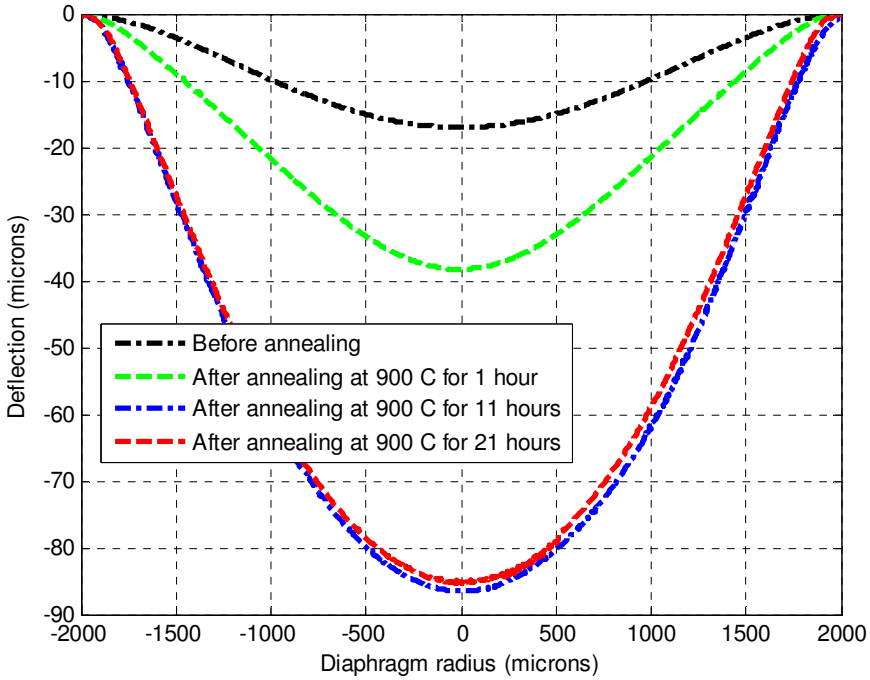

Figure 4- 30 the cross section of the surface profiles for the diaphragms with a radius of 2.0mm with respect to the annealing process at 900°C (sample 1): after anneal stage A (after annealing for 1 hour), after anneal stage B (after annealing for 11 hours), and after anneal stage C (after annealing for 21 hours) .

For the diaphragm with a radius of 2mm (Figure 4- 30) and 1.75mm (Figure 4- 31), the maximum deflections increased during the anneal stage A for 1 hour, and then the diaphragms deformed noticeably in the following anneal stage B for 10 hours. During the anneal stage C, the deformation decreased slightly for the diaphragm with a radius of 2mm, and the surface profile was maintained for the diaphragm with a radius of 1.75mm.

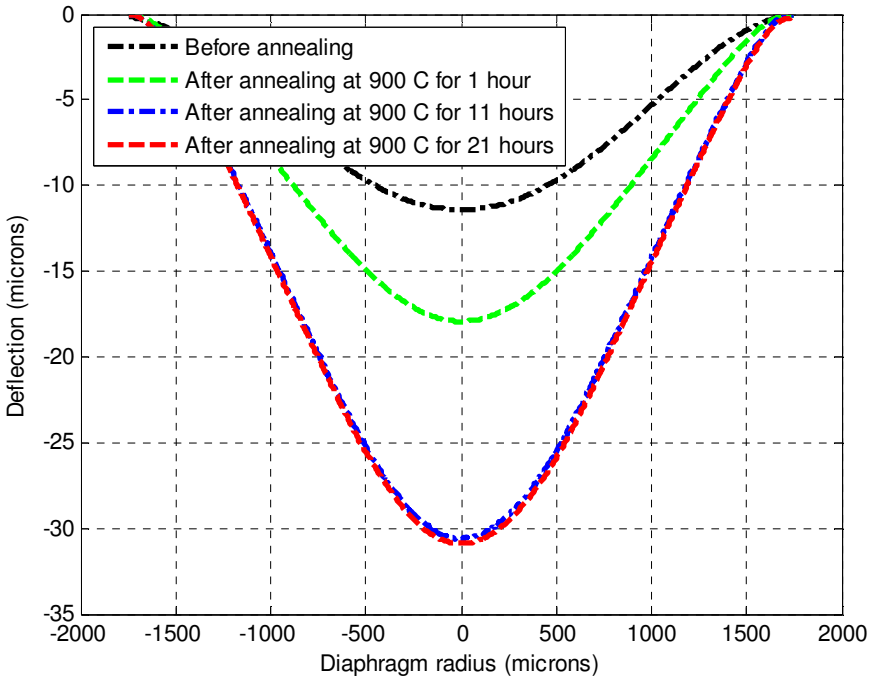

Figure 4- 31 the cross section of the surface profiles for the diaphragms with a radius of 1.75 mm with respect to the annealing process at 900°C (sample 1): after anneal stage A (after annealing for 1 hour), after anneal stage B (after annealing for 11 hours), and after anneal stage C (after annealing for 21 hours) .

The maximum deflections for each diaphragm radius with respect to the anneal time are listed in Table 4- 5.

Table 4- 5 The maximum deflections with respect to the anneal time

(the annealing temperature: 900°C)

Radius		**Maximum deflections (μm)**			
(mm)		Before annealing	After annealing A	After annealing B	After annealing C
	Total annealing time	0 hour	1 hours	11 hours	21 hours
0.50	Sample 1	0.082	0.083	0.080	0.079
	Sample2	0.095	0.097	0.094	0.089
	Sample 3	0.095	0.095	0.094	0.087
	Average	0.091	0.092	0.089	0.085
0.75	Sample 1	0.393	0.412	0.411	0.430
	Sample2	0.397	0.399	0.395	0.414
	Sample 3	0.393	0.399	0.395	0.405
	Average	0.394	0.403	0.400	0.416
1.00	Sample 1	1.151	1.161	1.170	1.185
	Sample2	1.169	1.176	1.174	1.191
	Sample 3	1.171	1.178	1.185	1.194
	Average	1.164	1.172	1.176	1.190
1.25	Sample 1	2.860	2.886	3.097	3.108
	Sample2	3.011	3.084	3.518	3.537
	Sample 3	2.781	2.837	2.960	3.013
	Average	2.884	2.936	3.192	3.220
1.50	Sample 1	5.859	6.320	10.282	10.364
	Sample2	6.123	6.672	12.353	12.447
	Sample 3	5.681	6.035	9.360	9.436
	Average	5.887	6.342	10.665	10.749
1.75	Sample 1	11.507	18.135	30.566	30.838
	Sample2	10.496	18.436	44.200	43.907
	Sample 3	10.262	16.077	31.067	31.601
	Average	10.755	17.549	35.278	35.449
2.00	Sample 1	17.150	38.606	86.585	85.458
	Sample2	17.744	40.234	86.575	85.484
	Sample 3	17.031	38.566	87.176	86.997
	Average	17.308	39.135	86.778	85.980
2.50	Sample 1	36.565	109.689	133.195	129.497
	Sample2	37.839	110.178	134.007	135.606
	Sample 3	37.231	110.456	136.837	126.445
	Average	37.211	110.107	134.680	130.516

In order to compare the deflections obtained from different anneal stages, the data is averaged and is plotted in Figure 4- 32. Neither plastic deformation nor creep effect was visible when the diaphragm radius is 1mm and under. The deformation increased noticeably during the anneal stage A and B for the diaphragms with the radius of 1.25mm and above. During the anneal stage C, no measurable creep occurred for the diaphragms with radii of 1.25mm to 1.75mm, while negative creep occurred for the diaphragms with a radius of 2mm and 2.5mm.

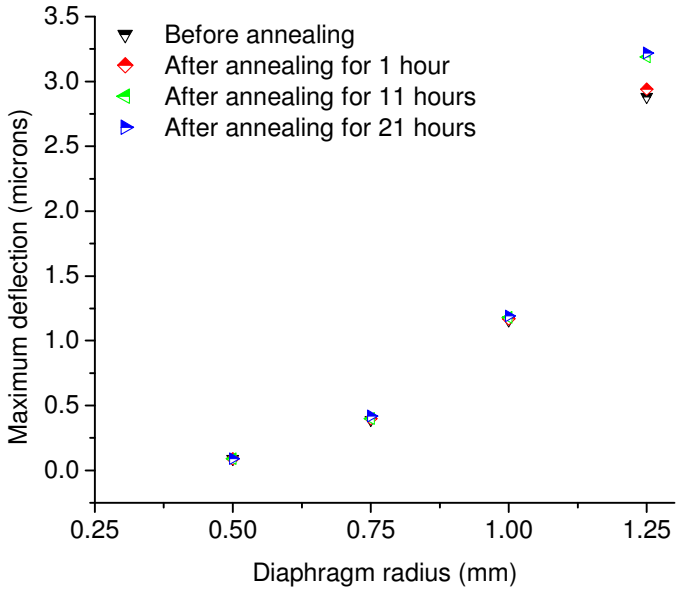

Figure 4- 32(a) The average of the maximum deflections with respect to the anneal time (the annealing temperature: 900°C, diaphragm size: 0.5mm-1.25mm)

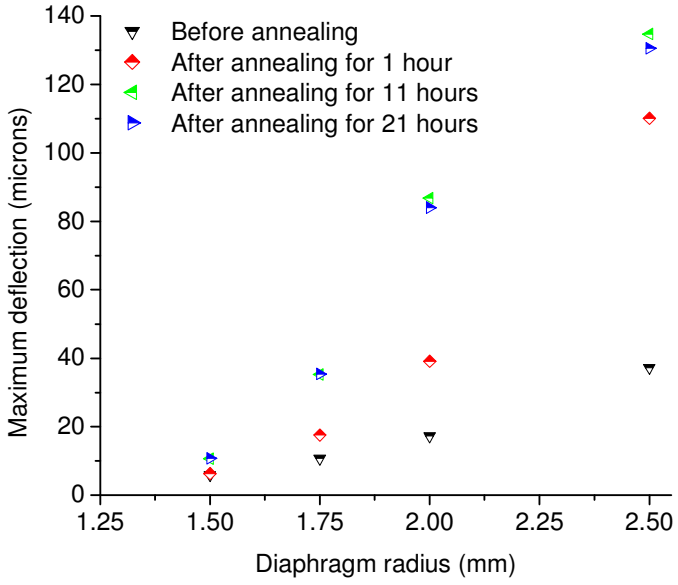

Figure 4- 32(b) The average of the maximum deflections with respect to the anneal time (the annealing temperature: 900°C, diaphragm size: 1.5mm-2.5mm)

For the sample 3 with a radius of 2.5mm, the decrease of the deflection during anneal stage C was up to 10μm. So the effect of the negative creep can not be ignored.

Negative creep has been observed during the bending of the boron-doped silicon due to the redistribution of vacancies and impurities in the transverse field of mechanical stress [4-17]. For the circular diaphragms with a radius of 2mm and 2.5mm, the elastic deformation under the atmospheric pressure is large deformation. The middle surface of the diaphragm is appreciably strained in order to resist the lateral load. So it is very likely that the vacancies and the impurities redistributed under the transverse stress during anneal at 900°C when the thermal energy is high enough. As a result, the vertical displacement of the diaphragm decreased.

4.5.4 **Discussion of the temperature effect and the size effect**

The advantage of the experiment is its simplicity. The influence of the pressure fluctuation on the measured profiles has been eliminated by adjusting the results to one standard atmospheric pressure. By comparing the surface profiles obtained before and after a number of annealing processes, the trend of the diaphragm deformations are obtained, and the results are fairly good for engineering applications.

However, the experiment doses not monitor the diaphragm deflections during annealing processes. So the stages of the creep deformation are not revealed. Meanwhile, due to the error of the measurement system, the profile changes for some diaphragms may be too small to be measured even with high vertical resolution. When the diaphragm is relatively large, the deflections after anneal can be larger than 100μm. So the resolution of the measurement system is set to low.

The experimental results revealed the size effect and the temperature effect on the elevated temperature behaviour. The radius of the diaphragm is designed from 0.5mm to 2.5mm. It was observed that larger diaphragms have a higher risk of creep and plastic deformation. At 600°C, dramatic creep deformations were observed for the largest diaphragms (radius of 2.5mm) over a long period (137 hours). When the operating temperature rises to 800°C, more diaphragms with smaller sizes (the radius of 1.75mm and above) deformed plastically. At 900°C, all the diaphragms larger than 1.25mm showed plastic deformation. For the smaller diaphragms, there were no measurable differences among the deflections obtained after the anneal stages.

When it comes to the plastic deformation, the influence of the diaphragm radius on the diaphragm behaviour is actually the influence from the stress level. Once the pressure applied on the silicon diaphragm is determined, the larger the diaphragm radius, the higher the induced stress. So the induced shear stress is more likely to reach the critical value and yields the slip of the dislocations.

The measurement results also indicate that high temperature increases the risk of creep and plastic deformation of the pressurized diaphragms. Figure 4- 33 shows the evolution of the deflections at three temperature levels for the diaphragms with a radius of 2.5mm. It is apparent that the largest deformation occurred at the highest temperature (900 °C), and both the plastic deformation and creep are noticed. Plastic deformation did not occur at 600°C. However, creep occurred over long period of time (69 hours) with very low rate. At 800°C, the creep was not measured in 31 hours after a dramatic deformation increase caused by plasticity.

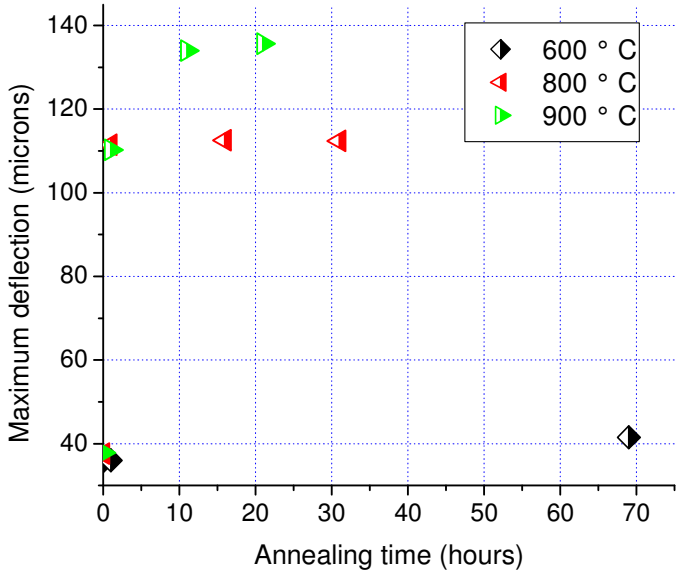

Figure 4- 33 Measured maximum deflections for the diaphragms with a radius of 2.5mm

For single crystal silicon, creep occurs when the annealing temperature is 600°C and above. Increasing temperature will increase the diffusion rate of the silicon atoms in the pressurized diaphragms, therefore, speeds up the progressive process of creep. When it comes to the plastic deformation, increasing temperature will decrease the value of the critical resolved shear stress (CRSS). So the pressurized diaphragms are more likely to deform plastically in a high temperature environment.

4.6 The elevated temperature behaviour of silicon diaphragms with implanted argon ions

Another set of experiments is to study the effect of the implanted argon ions on elevated temperature behaviour of silicon diaphragms. Ion implantation has been a primary step in the fabrication of the semiconductor devices. This technique changes the physical or electrical properties of a semiconductor by introducing dopant ions

into the target semiconductor. However, the resultant damage of the target surface can affect its mechanical properties, especially when the size of the device is down to the microscale. It has been observed that the surface toughness of single crystal silicon can be increased greatly by the Ar ion implantation at a moderate fluence of 1×10^{16}ions/cm^2 due to the formation of a nano-sized polycrystalline Si layer [4-18]. In addition, the extended defects arising from ion implantation and annealing of silicon may alter its plastic behaviour. These defects can be observed in the TEM (transmission electron microscope). The type and the density of the defects depends strongly on the implant and the anneal conditions [4-13]. However, the surface plasticity of the crystal silicon can be increased greatly if a high density of dislocations is induced.

This experiment investigates deformation of the ion implanted diaphragms at a moderate temperature of 800°C. In order that the experiment can be kept simple, the experiment proposed at section 4.3 is modified first of all. Some of the specimens have to receive Ar ion implantation after they were made. Only one annealing process is applied in this process. Then the damage caused by the Ar ion implantation in crystal silicon is predicted by SUSPRE, an ion implantation simulation package [4-19]. Finally, the deflections of the annealed diaphragms are presented as the function of the Ar ion fluence, and the effect of the Ar ion implantation is concluded based on the measured results.

4.6.1 Experiment procedures

According to the fabrication process presented in section 4.2.1, the silicon diaphragms are made from the device layer of BESOI wafer. A silicon wafer with heavily doped

boron (p-type silicon) or phosphorus (n-type silicon) is very common in fabricating MEMS devices. However, the high density of the dopant may have an effect on the mechanical behaviour of the devices. In order to minimize the effect of boron dopant on the diaphragm behaviour, BESOI wafer which has the device layer with a resistivity larger than 1000ohm-cm was chosen to fabricate ion implanted samples (the lower the boron concentration, the higher the silicon resistivity is). These ultra-high resistivity BESOI wafers are difficult to get and are very expensive.

The modified experimental procedures are presented as follows:

a) The specimens were first of all fabricated using the micromachining technology as described in section 4.3. The BESOI wafers which had the device layer with a resistivity larger than 1000ohm-cm were used as the diaphragm material.

b) Then the surface profiles of these specimens were measured firstly with Zygo NewView 5000^{TM} under the atmospheric pressure. The measurement was conducted at a laboratory temperature of 20°C at Loughborough University.

c) After the measurement, the specimens were sent to the Ion Beam Centre in the University of Surrey, where the Argon implantation was performed at 100keV at room temperature. The Ar^+ fluence was selected as 1×10^{16}ions/cm^2 and 1×10^{17}ions/cm^2, respectively.

d) The specimens were sent back to the laboratory at GE Druck and were annealed in the furnace at a temperature of 800°C for 30 minutes. The nitrogen gas with the atmospheric pressure was supplied during the annealing process.

e) Finally, these annealed samples were sent back to the University of Birmingham. The surface profiles were measured under the atmospheric pressure with a non-contact interferometer MicroXAM (Scantron, UK). Samples are imaged by using 5× objective lens, acquiring images in a grid array, which were subsequently stitched together. The measurement was taken at a temperature of 20°C in the School of Chemical Engineering.

4.6.2 Simulation of Ar ion implantation into silicon

SUSPRE is used to obtain the ion range and damage distribution profiles of Ar ions in single crystal silicon. The ion energy is 100keV. The plot depth is set to 3000Å. The resulting profiles are shown in Figure 4- 34(a) for the fluence of 1×10^{16}ions/cm^2, and in Figure 4- 34(b) for the fluence of 1×10^{17}ions/cm^2, respectively. The green dotted line illustrates the penetration range profile. For both fluence levels, the projected range is 1015.97Å and the straggle (the standard deviation of the projected range) is 324.4Å.

The result shows that the onset fluence for amorphisation is about 9.46×10^{14}ions/cm^2, so an amorphous layer is formed beneath the silicon surface for both fluence levels. However, the ion fluence has a great effect on the depth of the disordered atoms, as indicated by the blue dotted line. It can be seen that the depth of the completely disordered region is larger for the silicon exposed to the fluence of 1×10^{17}ions/cm^2 (Figure 4- 34(b)) than that for the silicon exposed to the fluence of 1×10^{16}ions/cm^2 (Figure 4- 34(a)).

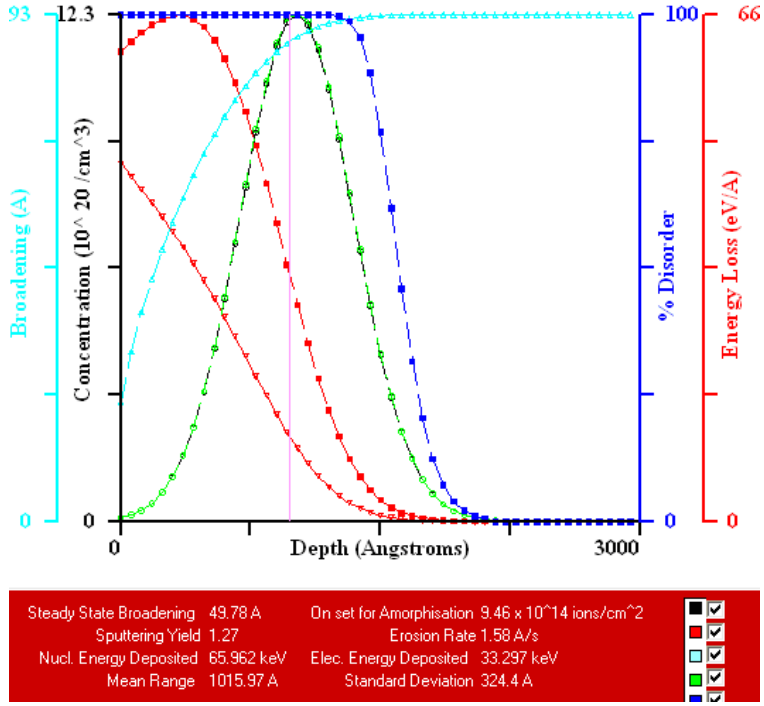

(a) Fluence of 1×10^{16}ions/cm^2

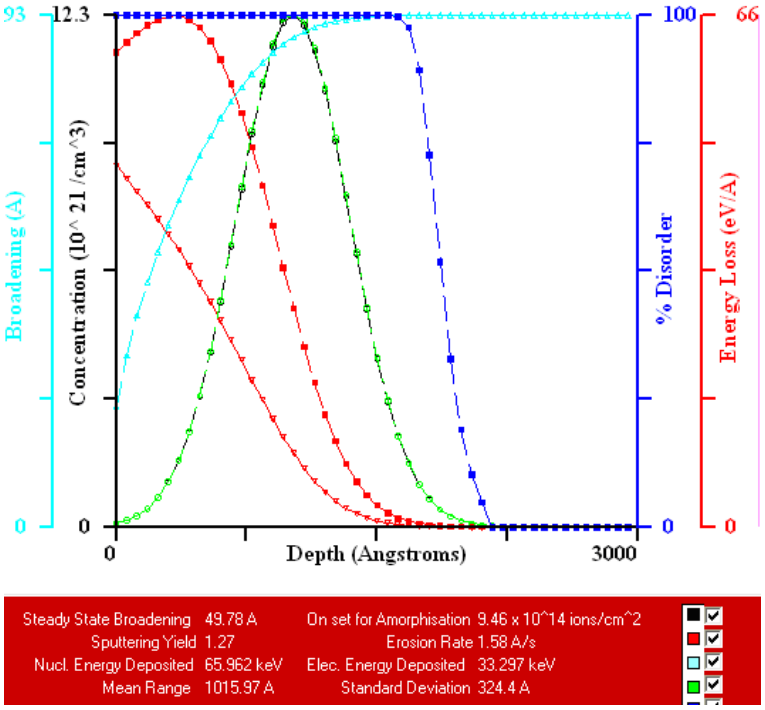

(b) Fluence of 1×10^{17}ions/cm^2

Figure 4- 34 SUSPRE simulation results for silicon implantation of Ar^+ at 100keV

The damage distribution profiles indicate that the implantation damage in silicon is greater at a larger Ar fluence. This can be seen by the appearance of the implanted silicon wafer. Figure 4- 35 and Figure 4- 36 are the photos of the silicon wafers with Ar-implanted fluence of 1×10^{16}ions/cm^2 and 1×10^{17}ions/cm^2, respectively. The photos were taken in the clean room lithography area where the light appeared yellow. It can be seen that the wafer implanted at the fluence of 1×10^{16}ions/cm^2 is slightly reflective (Figure 4- 35). On the contrary, the wafer implanted at a higher fluence turns purple and coarse, most likely due to the highly damaged surface (Figure 4- 36).

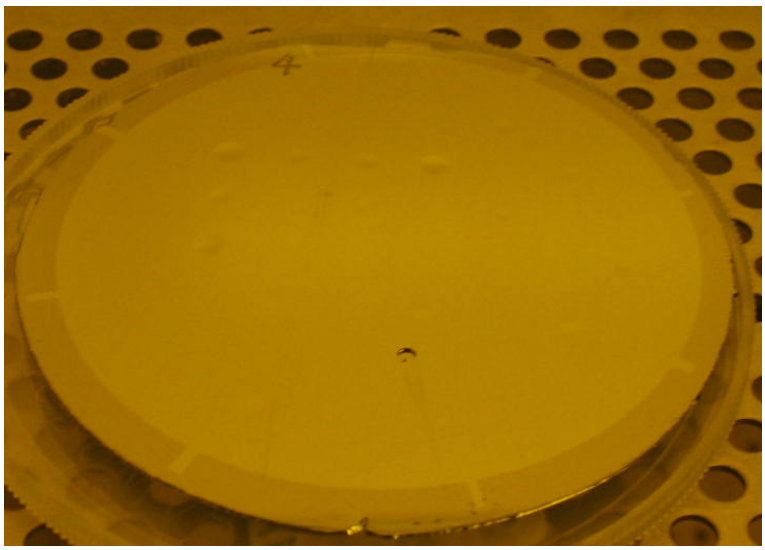

Figure 4- 35 Photo of the silicon wafer implanted with Ar ion at a fluence of 1×10^{16}ions/cm^2

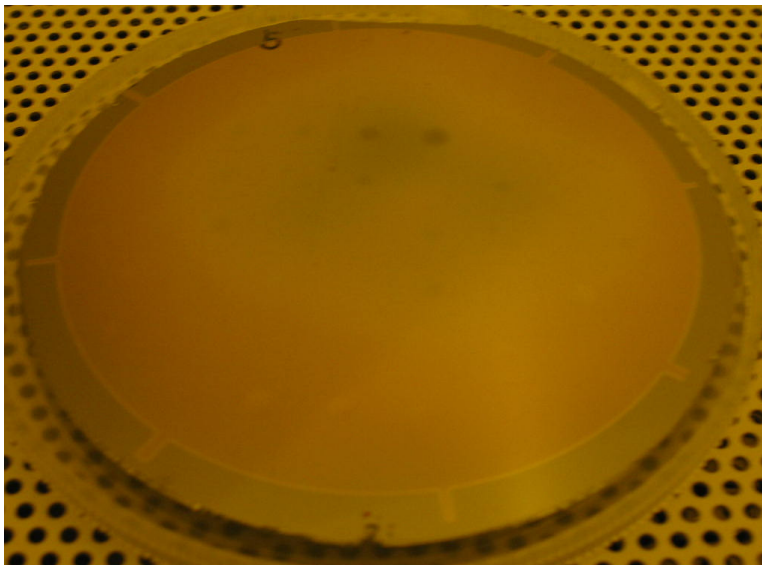

Figure 4- 36 Photo of the silicon wafer implanted with Ar ion at a fluence of 1×10^{17}ions/cm^2

Besides the depth and damage distribution profiles, the energy deposition profile is also obtained by SUSPRE, as indicated by the red dotted line. For both fluence levels, the energy deposited by the nuclear collisions to silicon atoms (deposited nuclear energy) is 65.962keV, while the energy deposited by the electronic collisions to silicon atoms (deposited electronic energy) is 33.297keV. In addition, the sputtering yield for Ar ion implantation into silicon at 100keV is 1.27, which means one incident argon ion causes average 1.27 silicon atoms to be ejected.

4.6.3 Experimental results and discussion

The maximum deflections of the implanted samples after annealing at 800°C for 30 minutes are listed in Table 4- 6 as a function of the Ar ion fluence. For the diaphragms with a radius of 1.75mm and under, the measured deflections do not show any difference with average deflections before annealing. So no measurable plastic deformation is observed. However, when the diaphragm size increases to 2mm or

2.5mm, the deflections increase apparently during the annealing process for ion implanted diaphragms.

Table 4- 6 The measured maximum deflection as a function of Ar ion fluence (μm)

Radius (mm)	Average max deflection before annealing	Maximum deflection after annealing			
			Ar ion fluence (ions/cm^2)		
			0	1.0E+16	1.0E+17
0.75	0.411	Sample 1	0.430	0.447	0.444
		Sample 2	0.413	0.429	0.434
		Sample 3	0.420	0.420	0.430
1.00	1.139	Sample 1	1.285	1.189	1.331
		Sample 2	1.301	1.150	1.307
		Sample 3	1.053	1.246	1.299
1.25	2.726	Sample 1	2.625	2.800	2.658
		Sample 2	2.780	3.377	2.939
		Sample 3	2.864	2.775	2.888
1.50	5.506	Sample 1	5.720	5.304	5.504
		Sample 2	5.855	5.672	5.803
		Sample 3	5.762	5.801	5.858
1.75	10.018	Sample 1	10.200	8.890	10.139
		Sample 2	10.147	10.640	9.983
		Sample 3	10.269	10.219	10.706
2.00	16.497	Sample 1	16.180	15.994	31.400
		Sample 2	16.028	22.173	19.051
		Sample 3	16.863	20.654	17.559
2.50	34.832	Sample 1	35.047	135.795	135.013
		Sample 2	147.452	127.768	140.111
		Sample 3	144.371	136.765	140.209

For the diaphragms with a radius of 2mm, the maximum displacements of the ion implanted Si samples are compared with those of unimplanted samples in Figure 4-37. It can be seen that there is no measurable plastic deformation for the unimplanted diaphragms. However, most Ar-ion implanted samples showed considerable increase in the deflection after the process of annealing. When the fluence is 1×10^{16}ions/cm^2, the deformation increases are up to 24% of the averaged deflection before annealing. When the fluence reaches 1×10^{17}ions/cm^2, the deformation increase is in the range

from 1.06μm to 14.90μm. The variation is caused by the implantation induced defects that are localized in each sample. Because the conditions of ion implantation and annealing process may not be evenly distributed across the silicon wafer, a wide variety of defects can be induced and the localized defects in each test sample are unique. So it is no surprise that the measured results show a wide variation.

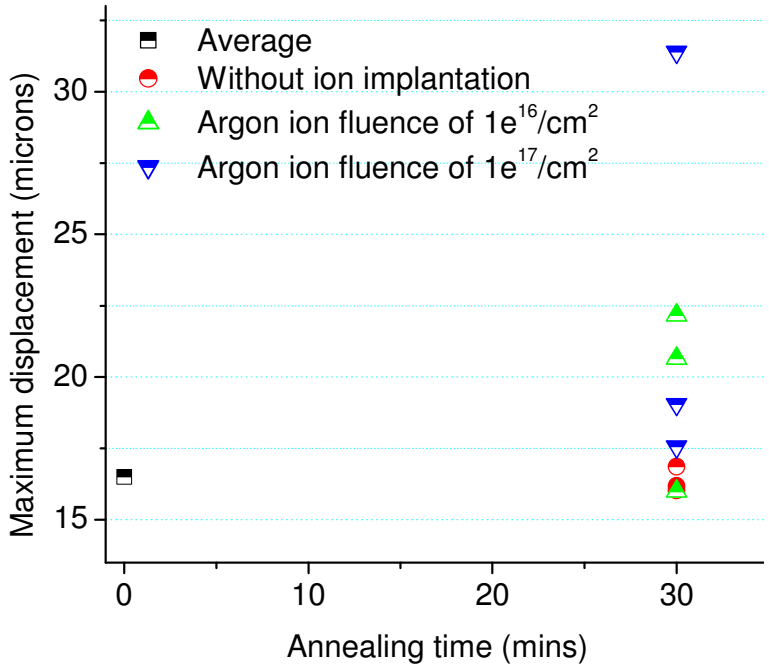

Figure 4- 37 The maximum displacement of unimplanted Si diaphragms and those implanted with Ar ions for the diaphragm with a radius of 2mm

For diaphragms radius of 2.5mm, the maximum displacements of ion implanted Si samples are compared with those of unimplanted samples in Figure 4- 38. It can be seen that two out of three unimplanted test samples showed significant plastic deformation in the annealing process, while all the implanted test samples exhibited considerable plastic deformation. However, the results can not show any correlation between the Ar ion fluence and the deflection after annealing.

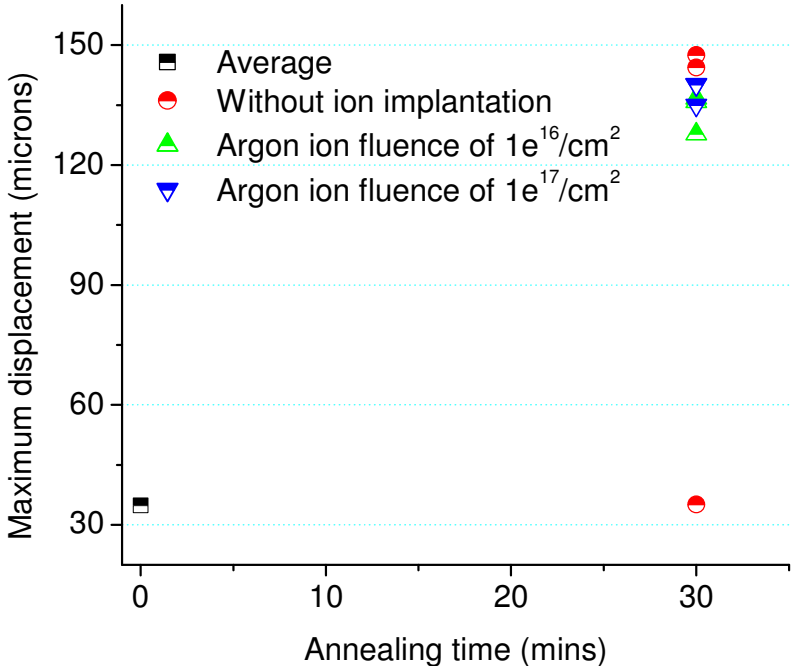

Figure 4- 38 the maximum displacement of unimplanted Si diaphragms and those implanted with Ar ions for diaphragm radius of 2.5mm

The experiment implies that the ion implanted silicon is more likely to deform plastically than the unimplanted silicon. Because the induced defects on the Ar ion implanted surface can provide active sources for the dislocation generation during annealing, the yield strength of the implanted silicon is lower than that of the unimplanted silicon. For the unimplanted silicon, the diaphragms with a radius of 2mm did not deform plastically, while most of the diaphragms with a radius of 2.5mm deformed plastically during annealing at 800°C. Therefore, the yield strength of the unimplanted silicon at 800°C should be above 150MPa (the maximum resolved shear stress for the diaphragm with a radius of 2mm according to Figure 3-13), and may be just under 200MPa (the maximum resolved shear stress for the diaphragm with a radius of 2.5mm according to Figure 3-13). For the Ar ion implanted silicon, most of the diaphragms with a radius of 2mm deformed plastically, while all the diaphragms with a radius of 2.5mm deformed plastically during annealing at 800°C. Therefore, the yield strength of the implanted silicon may be just above 150MPa (the maximum

resolved shear stress for the diaphragm with a radius of 2mm according to Figure 3-13) at 800°C.

It can be seen that the extended defects that form after ion implantation and annealing of silicon play an important role in the evolution of plastic deformation. In order to reveal the effect of the damage on the diaphragm plasticity, the study of the defects and the microstructure by TEM is helpful. The TEM samples of single crystal silicon have been fabricated successfully using the FEI Strata^{TM} Dual Beam 235 FIB/SEM workstation in the Bio-medical and Micro Engineering Research Centre. The samples were prepared automatically by AutoTEM script, as shown in Figure 4- 39. The width of the sample is 30μm and the thickness of the sample is 100nm. Then the sample was lifted out and attached to the TEM grid by Ms Ming Chu in the Centre for Electron Microscopy, as illustrated in Figure 4- 40. However, the preparation for the TEM samples will damage the micromachined silicon diaphragms. Therefore, they are not included in current experiment. But to observe the defects in implanted silicon by TEM can be valuable work in the future.

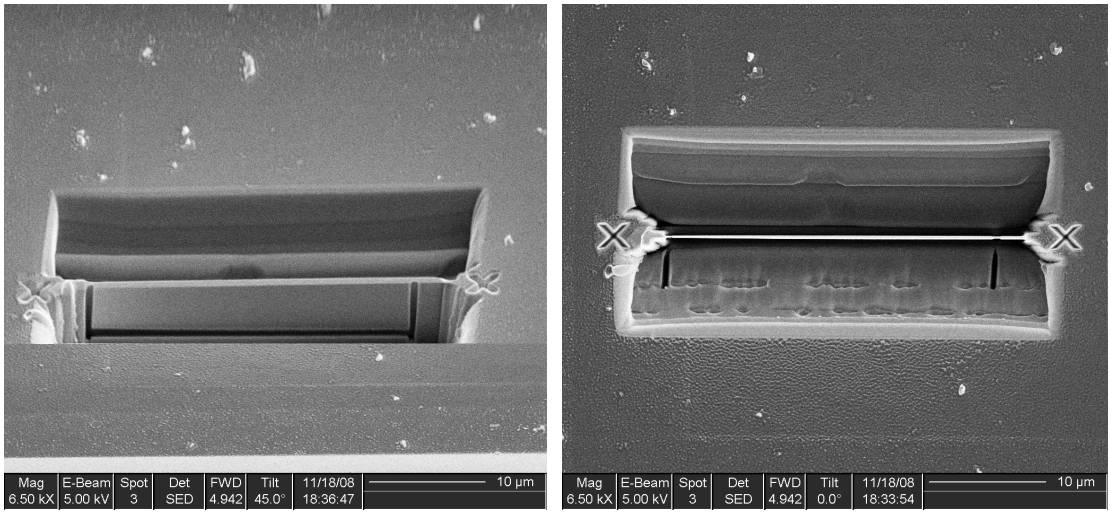

(a) (b)

Figure 4- 39 SEM images of the TEM samples fabricated in the Bio-medical and Micro Engineering Research Centre (a) side view tilt at 45°; (b) Top view

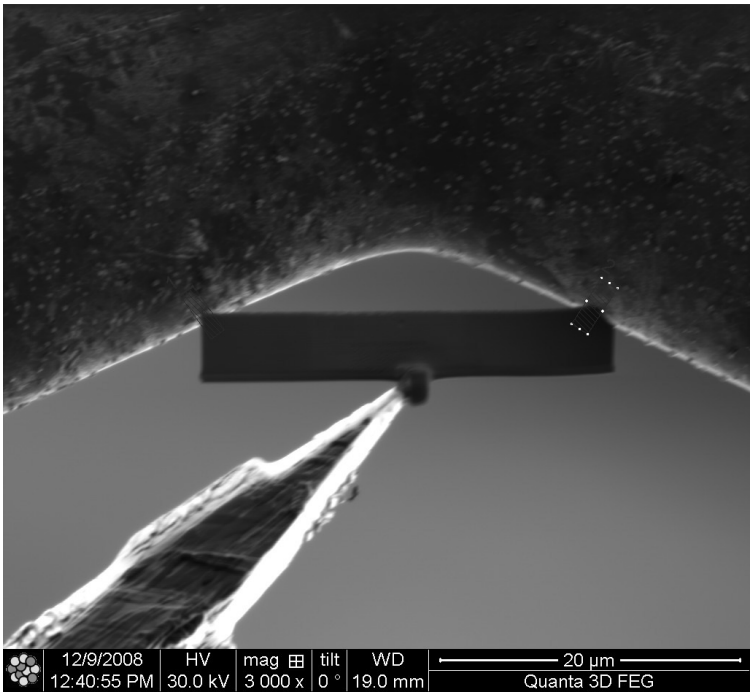

Figure 4- 40 The sample is attached to a copper TEM grid using a Pt deposition

4.7 Conclusions

Because the plastic deformation is a very complicated process, this work is focused on the mechanical aspect of the phenomenon. A series of experiments were performed to investigate the effect of size, temperature and ion implantation on the deformation of silicon diaphragms. The study of the dislocations generated in the implanted diaphragm is helpful for a better understanding of the mechanism of plastic deformation, but is not very important at current stage of the research.

The samples for testing were fabricated by micromachining technology with good control over diaphragm thickness, and the fabrication imperfection contributes to the variety of the experimental data. The experiment measures the surface profiles before and after each anneal stage. The diaphragm behaviour during high-temperature annealing is then obtained by comparing the measured deflections. The experiment takes advantage of the permanent property of the plastic deformation, which allows the measurement of the deflection at room temperature. So the experimental settings are much simplified compared to experiments which take measurement directly at high temperature environment.

The experiment implies that either increasing diaphragm radius or increasing operating temperature will increase the risk of creep and plastic deformation of the pressurized diaphragms. Therefore, the diaphragms with small size are more likely to survive in high temperature environment. The measured results provide good reference data for designing the sensing diaphragm in high temperature pressure sensors (under atmospheric pressure). If the device is required to operate at 600°C, the creep deformation is the main consideration. The available size of the diaphragm is in

a wide range up to 2mm. If the radius is 2.5mm and above, the creep deformation can be significant in 69 hours (anneal stage B for test sample 3). When the operating temperature rises to 800°C, the radius of the diaphragm should be limited to under 1.5 mm. The diaphragms with larger radius would deteriorate a short while after being put in the high temperature environment due to the occurrence of the plastic deformation. At 900°C, the rate of the plastic deformation is very high, and the amount of the plastic deformation can be dramatic for large diaphragms. Therefore, the diaphragm radius should be less than 1.25mm in order that the plastic deformation will not happen.

There are three main conclusions from the experiment. Firstly, since the available dimension becomes smaller with increasing temperature, the sensitivity of the diaphragm to pressure is reduced consequently. Therefore, the transduction mechanism should be selected carefully when using small diaphragms in order that the pressure induced signal can be sensed with a desired resolution. Secondly, the ion implanted silicon is more likely to deform plastically due to the extended defects which formed after ion implantation and annealing of silicon. Therefore, ion implantation should be avoided in the micromachining processes. Or at least, the fluence of the ion needs to be restricted in order to reduce the surface damage. At last, for all the diaphragms with qualified dimensions, it is important to evaluate the creep deformation over long periods of time according to the application requirements.

List of References

[4-1] Silicon materials, Malteserstraße 444a D-86899 Landsberg/Lech

[4-2] Klaassen EH, Petersen K, Noworolski JM, Logan J, Maluf NI, Brown J, et al. Silicon fusion bonding and deep reactive ion etching: a new technology for microstructures. SENSOR ACTUAT A-PHYS 1996; 52(1-3): 132-139

[4-3] Rohm and Haas Company, Philadelphia, PA, USA

[4-4] Surface Technology Systems, Imperial Park Newport, NP10 8UJ United Kingdom

[4-5] Ayón AA.; Zhang X.; Khanna R. Anisotropic silicon trenches 300-500µm deep employing time multiplexed deep etching (TMDE). SENSOR ACTUAT 2001; 91: 381–385

[4-6] Ayón AA.; Braff R; Lin CC; Sawin HH; Schmidt MA. Characterization of a TimeMultiplexed Inductively Coupled Plasma Etcher. J ELECTROCHEM SOC 1999; 146 (1): 339–349

[4-7] Bhardwaj J, Ashraf H, McQuarrie A, Dry Silicon Etching for MEMS, Symposium on Microstructures and Microfabricated Systems, Annual Meeting of the Electrochemical Society, Montreal, 1997

[4-8] Barth PW, Silicon fusion bonding for fabrication of sensors, actuators, and microstructures, SENSOR ACTUAT 1990; A23: 919-926

[4-9] Tada H, Kumpel AE, Lathrop RE, Slanina JB, Nieva P, Zavracky P, et al. Thermal expansion coefficient of polycrystalline silicon and silicon dioxide thin films at high temperatures, J APPL PHYS 2000; 87:4189-4193

[4-10] Kovacs GTA., Maluf NI and Petersen KE, Bulk Micromachining of Silicon, PROC IEEE 1998; 86(8):1536 – 1551

[4-11] Maboudian R, Surface Process in MEMS Technology, SURF SCI REP 1998; 30: 207-269

[4-12] Zhang LM, Uttamchandani D, Culshaw B and Dobson P, Measurement of Young's modulus and internal stress in silicon microresonators using a resonant frequency technique. MEAS SCI TECHNOL 1990; 1: 1343–1346

[4-13] Hull R. Properties of Crystalline Silicon. London: INSPEC; 1999

[4-14] ZYGO CORPORATION, LAUREL BROOK ROAD, MIDDLEFIELD, CT 06455

[4-15] Taylor Hobson Ltd, 2 New Star Road, Leicester, LE4 9JQ, England

[4-16] John V, Introduction to Engineering Materials, 3rd edition, Hampshire and London: MACMLLAN PRESS LTD, 1992, p103-104

[4-17] Shmidt VA, Negative creep during bending of boron-doped silicon, Fizka Tverdogo Tela 1972; 14(12): 3675-3676

[4-18] Sun R, Xu T, and Xue QJ, Effect of Ar+ ion implantation on the nano-mechanical properties and microstructure of single crystal silicon. APPL SURF SCI 2005; 249(1-4): 386-392

[4-19] University of Surrey Ion Beam Centre, Nodus Laboratory, University of Surrey, Guildford, Surrey GU2 7XH, United Kingdom

5 A CONSTITUTIVE MODEL FOR PLASTIC BEHAVIOUR OF SILICON DIAPHRAGMS AT ELEVATED TEMPERATURES

5.1 *Introduction*

In a previous chapter it was reported that plastic deformation due to the slip of dislocations was observed in some of the silicon diaphragms at annealing temperatures of 800°C and 900°C. The magnitude of the plastic deformation depended upon the pressure induced stress at a given temperature, and evolved over the operating time. The onset of the plastic deformation has been predicted using the resolved shear stress (see section 3.4). However, modelling of the plastic deformation can provide a better understanding of the diaphragm behaviour at elevated temperatures, and help to optimize the structure dimensions and estimate the device lifetime.

The plastic behaviour of silicon can be approximated using constitutive models [5-1]. As plastic deformation occurs, the dislocations in silicon begin to move, and the number of the dislocations increases rapidly due to generation by Frank-Read sources. In the initial stage, the dislocation density is low, and the dislocations move primarily on parallel glide planes, so the slip is relatively ‘easy’. Alexander and Hassen’s model proposed that the magnitude of the plastic shear strain rate in the early stage is governed by the density of mobile dislocations [5-2]. After a sufficiently large number of dislocations have been generated, the dislocations in different slip systems interact with each other, and impede their motion through the crystal lattice. Therefore, the

plastic flow is resisted. Based on this phenomenon, it is proposed by Myshlyaev et al. that the slip resistance governs the plastic strain rate in the later stage of the deformation [5-3]. The slip resistance has the dimensions of stress. The larger the slip resistance, the lower the plastic strain rate. The transition between the two deformation regions occurs at a certain critical dislocation density [5-1]. This means when the dislocation density is less than the critical value, the plastic deformation can be described using the dislocation density by the Alexander and Hassen's model; when the dislocation density grows above the critical value, the material deformation can be described by the interactions among dislocations.

This chapter models the plastic behaviour of micromachined silicon diaphragms in the first hour annealing (anneal stage A) at a temperature of 800°C and 900°C respectively. The deformation caused by the temperature ramps of the furnace is included. Because the deformation is at the very early stage, the constitutive model implemented here is based on the Alexander-Hassen model. The rate of the diaphragm deformation is governed by the density of moving dislocations. In the following sections, the basic constitutive equations used in the Alexander and Hassen's model are introduced first of all. The implementation of the constitutive model in the FEA software is then presented. The settings used in the FEA model for the boundary conditions, the mesh and the material parameters are described in detail. The simulation results, including the distribution of dislocation density and the evolution of the diaphragm deflections, are illustrated and discussed.

5.2 *The constitutive equations*

The constitutive model proposed by Alexander and Hassen has been universally used for the study of the elevated temperature behavior of silicon and other semiconductors [5-1] [5-4] [5-5]. Assuming uniform deformation in the whole specimen, the model uses a set of coupled equations to describe the plastic shearing strain rate and the multiplication of the mobile dislocations. It has been shown that the Alexander and Hassen's model is valid for silicon over a stress range of 10MPa to 120MPa and a temperature range of 900K to 1200K [5-2].

The basic constitutive equation for the stress in silicon is taken as the linear relation:

Equation 5- 1

$$\sigma = C\left[\varepsilon - \alpha_T (T - T_0) I\right]$$

where σ is the Cauchy stress tensor, ε is the small strain tensor, C is a fourth-order isotropic elasticity tensor (6-by-6 elasticity matrix, Equation 3-1 in section 3.2.1), $\alpha_T I$ is a second-order thermal expansion tensor, T and T_0 are absolute temperature and a reference temperature, respectively.

At small strains, the strain rate is composed of an elastic part, $\dot{\varepsilon}_{ij}^{el}$, a thermal expansion part, $\dot{\varepsilon}_{ij}^{th}$, and a viscoplastic part, $\dot{\varepsilon}_{ij}^{vp}$:

Equation 5- 2

$$\dot{\varepsilon}_{ij} = \dot{\varepsilon}_{ij}^{el} + \dot{\varepsilon}_{ij}^{th} + \dot{\varepsilon}_{ij}^{vp}$$

The elastic strain rate and the thermal strain rate can be solved by built in equations in Comsol Multiphysics. However the viscoplastic stain rate needs to be defined by the user.

The viscoplastic strain rate tensor can be expressed as [5-6]:

Equation 5- 3

$$\dot{\varepsilon}_{ij}^{vp} = \frac{3}{2}\dot{\bar{\gamma}}^{p}\frac{S_{ij}}{\sigma_e}$$

where $\dot{\bar{\gamma}}^{p}$ is the plastic shear strain rate, σ_e is the von Mises effective stress, and S_{ij} is the deviatoric part of Cauchy stress tensor which tends to distort the stressed body. The stress deviator tensor can be obtained by subtracting the mean normal stress tensor from the Cauchy stress tensor σ_{ij}:

Equation 5- 4

$$S_{ij} = \begin{bmatrix} \sigma_{11} & \sigma_{12} & \sigma_{13} \\ \sigma_{21} & \sigma_{22} & \sigma_{23} \\ \sigma_{31} & \sigma_{32} & \sigma_{33} \end{bmatrix} - \frac{1}{3}\begin{bmatrix} \sigma_{11} & 0 & 0 \\ 0 & \sigma_{22} & 0 \\ 0 & 0 & \sigma_{33} \end{bmatrix}$$

where the second term on the right side represents the mean normal stress tensor which tends to change the volume of the stressed body.

It can be seen from Equation 5- 3 that the viscoplastic stain rate is linearly proportional to the plastic shear strain rate. So the magnitude of the plastic shear strain rate plays an important role in the progress of the plastic deformation. The plastic shear strain rate, which relates to the motion of the mobile dislocations, is given by Orowan's law [5-7]:

Equation 5- 5

$$\dot{\bar{\gamma}}^{P} = Nbv$$

where N is the density of mobile dislocations (dislocation density is defined as the total length of dislocations per cubic centimeter), b is the magnitude of Burgers vector and v is the average velocity of the dislocations.

The velocity of dislocations moving within the deformed single crystal depends on the absolute temperature T and the effective shear stress τ_{eff} :

Equation 5- 6

$$v = v_0 \exp(-Q/kT)(\frac{\tau_{eff}}{\tau_0})^{\frac{1}{m}}$$

where v_0 is a reference value for dislocation velocity, Q is an activation energy, k is the Boltzmann constant, τ_0 is a reference stress, and m is a strain rate hardening exponent. The effective stress necessary to overcome the intrinsic resistance is given by:

Equation 5- 7

$$\tau_{eff} = \sigma_e - \tau_i$$

where τ_i is the internal stress caused by the dislocations:

$$\tau_i = A\sqrt{N}$$

where A is the hardening factor given by:

$$A \approx \frac{\mu b}{2\pi(1-\nu)}$$

where μ is the shear modulus, ν is Poisson's ratio. It is assumed that A is the same for all the generated dislocations in the single crystal.

Therefore by inserting Equation 5- 6 into Equation 5- 5, the plastic shear strain rate can be expressed as:

Equation 5- 8

$$\dot{\bar{\gamma}}^p = Nbv_0 \exp(-Q/kT)\left(\frac{\tau_{eff}}{\tau_0}\right)^{1/m} sign(\tau_{eff})$$

The sign of the effective stress controls the motion of the dislocations. If the effective stress is positive (the applied stress is greater than the internal stress), the dislocations are able to overcome the intrinsic resistance and therefore the slip of the dislocations occurs. Otherwise, the dislocations are trapped in the crystal and there is no plastic deformation.

The multiplication of dislocations in easy glide conditions is given by the empirical equation:

Equation 5- 9

$$\dot{N} = \left(\frac{K}{b}\right)\dot{\bar{\gamma}}^{p}\tau_{eff}$$

where K is a multiplication rate constant. It can be seen that the dislocation multiplication rate is related to the magnitude of the plastic strain rate and the effective stress.

5.3 *FEA Model*

The constitutive model has been implemented in the FEA software, Comsol Multiphysics 3.5a. Because the silicon diaphragm is axisymmetrical, the displacement field is simulated using Stress-Strain application mode of MEMS Module in axial symmetry (2D). Figure 5- 1 shows the schematic drawing of the model geometry. The structure of the silicon substrate is simplified to a square in order to generate a fine mesh in the diaphragm with a reasonable number of mesh elements. The atmospheric pressure is applied on the top of the structure. Because a corner with a right angle introduces the stress concentration, a round corner (as shown in Figure 5- 1) and a

refined mesh (as shown in Figure 5- 2) are used near the diaphragm edge in order to prevent numerical overshoot in the values of dislocation density and the effective stress. The equivalent elastic properties obtained in Table 3-4 in section 3.3.2 for (100) orientated silicon are applied in the model.

Because the whole silicon wafer is free to expand or contract in the furnace during high temperature anneal, and the test structure is made of pure silicon, there is no thermally induced stress in the test samples. But the expansion of silicon would increase the size of the diaphragm slightly. As shown in Figure 3-4 in section 3.2.3, the thermal expansion coefficient of silicon is about 4.25×10^{-6}/K at 1000K. So the size of the silicon diaphragm will expand 0.425%. For the diaphragm with the maximum radius of 2.5mm, the radius of the diaphragm will increase 10.624μm. Since the size increase of the diaphragm is much smaller than the diaphragm radius, it is assumed that the boundaries of the diaphragm are fixed during the high temperature anneal.

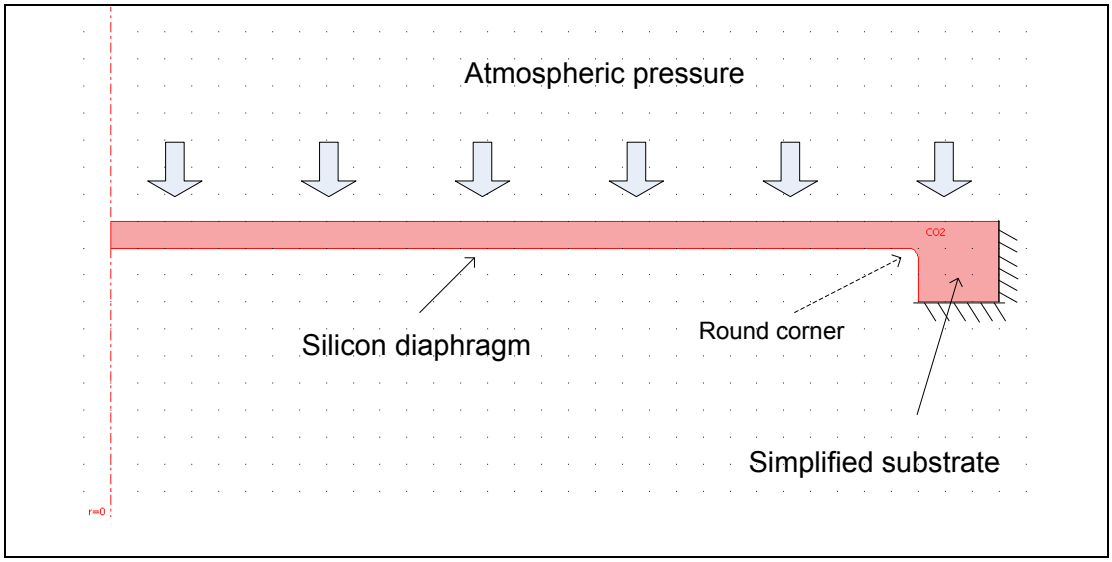

Figure 5- 1 Schematic drawing of the silicon diaphragm (Radius=1. 5mm)

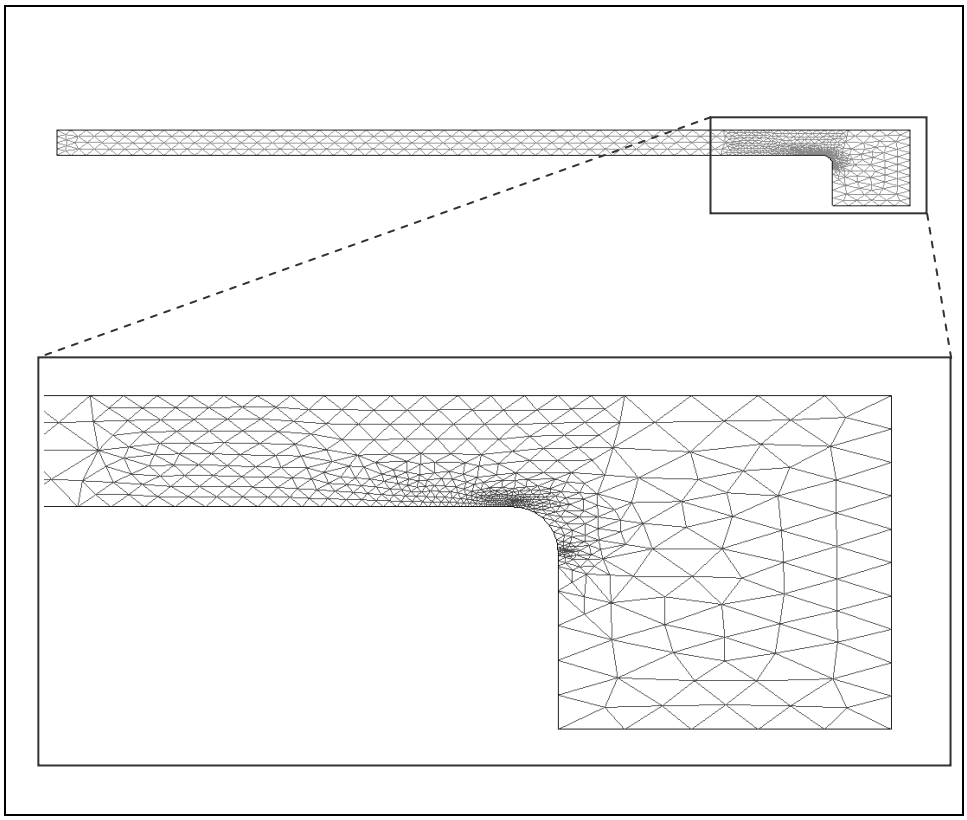

Figure 5- 2 A refined mesh near the diaphragm edge (Radius=1. 50mm)

The plastic shear strain rate is defined by the option of scalar expressions in the MEMS module according to Equation 5- 8. The Burger's vector b is 3.83×10^{-10}m. The activation energy Q is 3.47×10^{-19}J. Parameter m is 0.9. The dislocation velocity for boron doped silicon is only slightly smaller than that in high purity silicon [5-8]. The magnitude of the reference dislocation velocity is 6.0×10^{3}m/s for 60° dislocations and is 7.0×10^{3} m/s for screw dislocations under a shear stress of 20MPa [5-9]. It can be seen that there is no significant differences between the reference dislocation velocities for these two types of dislocations. So an average value of 6.5×10^{3}m/s is taken for v_0 in order to simplify the calculation. The shear modulus μ is 64GPa. The operating temperature is a function of the anneal time. The magnitudes defined for

annealing stage A are 800°C and 900°C as illustrated in Figure 5- 3 and Figure 5- 4 respectively.

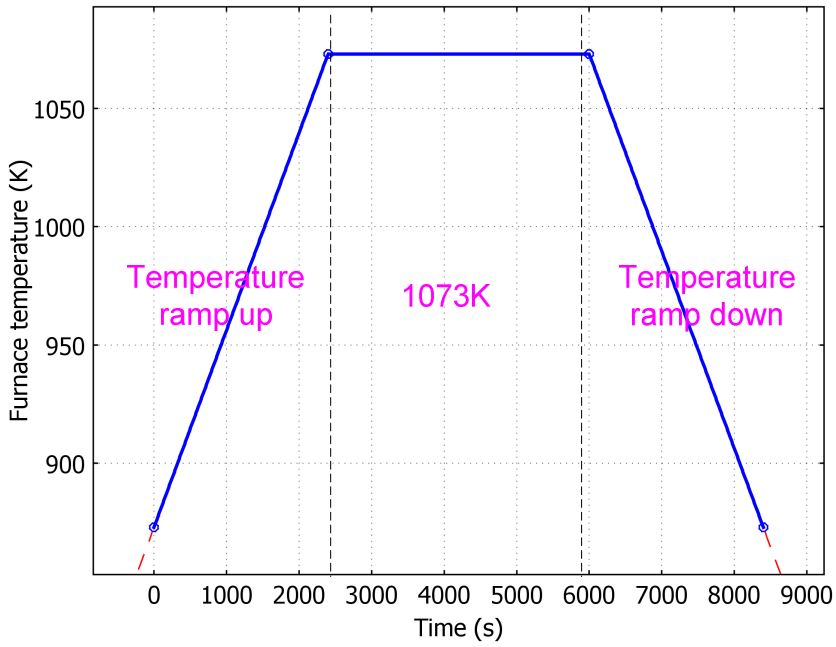

Figure 5- 3 Furnace temperature at stage A for annealing at 800°C

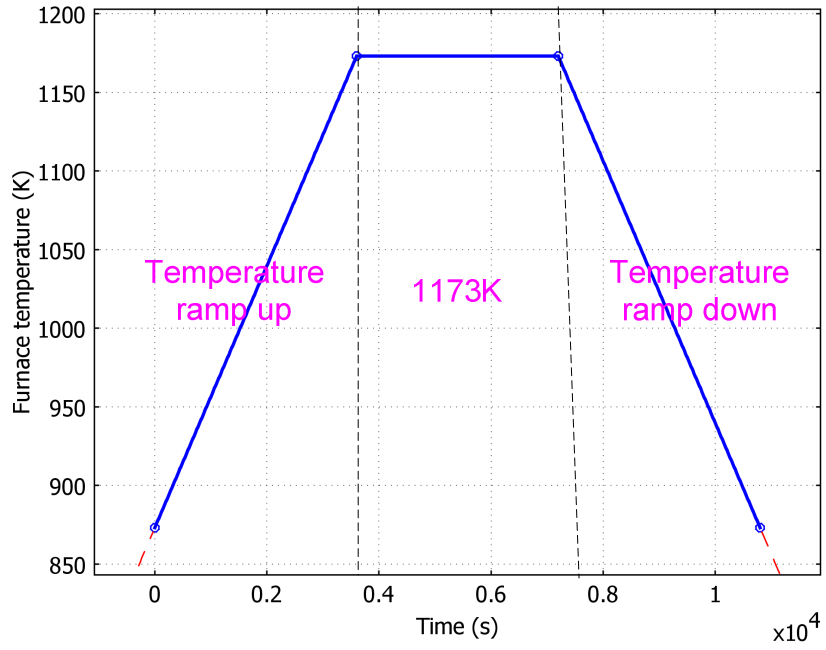

Figure 5- 4 Furnace temperature at stage A for annealing at 900°C

Two PDE general form modes in Comsol Multiphysics are used to compute the dislocation density N and the viscoplastic strain ε^{vp}. The initial dislocation density N_0 is estimated as $2\times10^7/m^2$ [5-1]. The evolution of dislocation density with time is mainly controlled by the multiplication rate constant K. The axisymmetrical model uses cylindrical coordinate r, φ and z. The model assumes that the displacement in the φ direction together with $\tau_{r\varphi}$, $\tau_{\varphi z}$, $\gamma_{r\varphi}$ and $\gamma_{\varphi z}$ components of the stresses and strains are zero. According to Equation 5- 3, the viscoplastic strain rate can therefore be expressed as:

Equation 5- 10

$$(\dot{\varepsilon}^{vp})_r = \frac{3}{2}\dot{\bar{\gamma}}^p \frac{(2\sigma_r - \sigma_\phi - \sigma_z)}{3\sigma_e}$$

$$(\dot{\varepsilon}^{vp})_\phi = \frac{3}{2}\dot{\bar{\gamma}}^p \frac{(2\sigma_\phi - \sigma_r - \sigma_z)}{3\sigma_e}$$

$$(\dot{\varepsilon}^{vp})_z = \frac{3}{2}\dot{\bar{\gamma}}^p \frac{(2\sigma_z - \sigma_r - \sigma_\phi)}{3\sigma_e}$$

$$(\dot{\varepsilon}^{vp})_{rz} = \frac{3}{2}\dot{\bar{\gamma}}^p \frac{\sigma_{rz}}{\sigma_e}$$

The PDE modes are coupled to the Stress-Strain application mode. According to Equation 5- 2, the viscoplastic strains should be excluded from the total strains in the expressions for the elastic stresses of the equation system. Then the displacement obtained from the Stress-Strain application mode represents the sum of the plastic deformation and the elastic deformation.

According to previous work by Moon et al., when the density of the mobile dislocations reaches a critical value, the interaction between dislocations becomes so

intense that the resistance to dislocation slip becomes the dominant factor in the plastic behaviour of silicon [5-1]. The Myshlyaev's model suggests that the plastic shear strain rate is now dependent on the magnitude of the slip resistance and its evolution [5-3]. The initial value of the slip resistance for the Myshlyaev's model can be determined mathematically using the plastic shear strain rates for the model of Alexander and Hassen at the transition moment. So by using smoothed heaviside function (flc1hs), the constitutive equations based on Myshlyaev's model can be operated while the constitutive equations based on Alexander and Hassen mode are deactivated when the dislocation density is above the critical value. However, due to the uneven induced stress across the diaphragm, the plastic shear strain rate varies from nodes to nodes, so does the multiplication of dislocations (according to Equation 5- 9). This means the transitions between the two deformation regimes take place at different moments for different nodes. As a result, how to obtain the initial value of the slip resistance at transition moment is a problem using Comsol Multiphysics. Therefore, modelling of the plastic behaviour at the later deformation stage is not implemented in current FEA model. The plastic deformation of silicon diaphragm is only modelled at the initial stage.

5.4 *Simulation results and discussions*

The diaphragm behavior is modeled at a temperature of 800°C and 900°C respectively. With the aid of finite element method, the outputs from the model cover a wide range of important information. Since the density of the moving dislocations governs the plastic behaviour of silicon diaphragms at the early stage of annealing, the distribution

of the dislocation density and the evolution of the diaphragm deflection are the main interests here.

5.4.1 Predicted diaphragm behaviour at 800℃

5.4.1.1 The distribution of the dislocation density

Figure 5- 5 shows the prediction of the distribution of the dislocation density in the silicon diaphragm with a radius of 1.75mm after annealing at 800°C for one hour. It can be seen that the dislocation multiplication rate is very low at the region close to the middle plane. The dislocation densities of about $3.5\times10^7/m^2$ are found at the upper and lower surface near the diaphragm edge as illustrated by the light blue colour in the figure. The maximum dislocation densities of about $6.345\times10^7/m^2$ are concentrated in a small region at the lower corner near the edge of the diaphragm. This results from the stress concentration at the round corner, as shown in Figure 5- 6. The maximum von Mises effective stress in the small region is 123MPa. This value is much higher than that of about 80MPa in the region nearby.

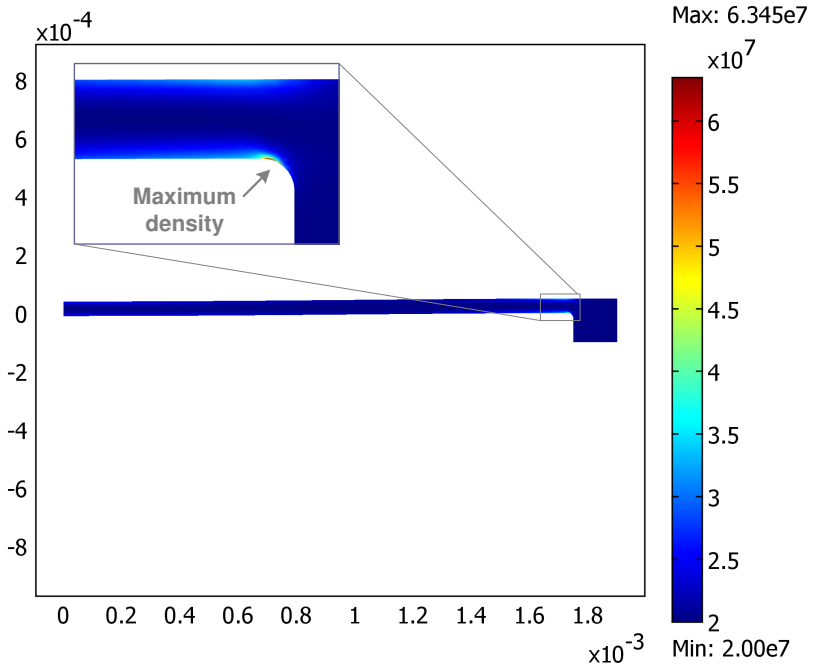

Figure 5- 5 The distribution of dislocation density for the diaphragm with a radius of 1.75mm after annealing at 800°C for one hour

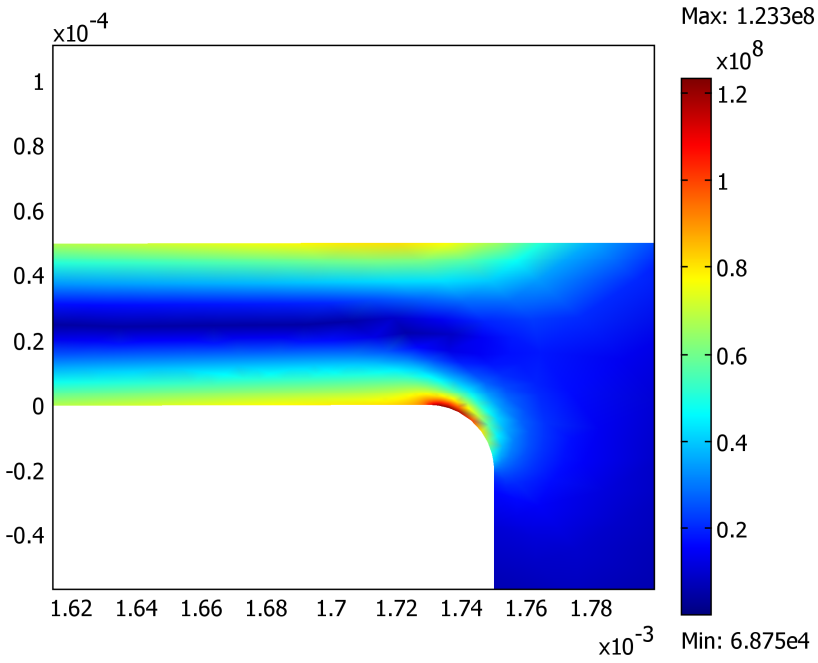

Figure 5- 6 Von Mises effective stress of the diaphragm with a radius of 1.75mm under the atmospheric pressure before annealing

Using the same initial settings, the model was run for various diaphragm dimensions (0.5mm-2.5mm). The dislocation density distributions near the diaphragm edge are shown in

Figure 5- 7. The initial dislocation density is assumed to be $2.0\times10^{7}/m^{2}$. The dislocation density after annealing does not show much increase for the diaphragms with a radius of 0.5mm, 0.75mm and 1mm. With the increase of the diaphragm dimension, the number of dislocations grows slowly in most regions of the diaphragm. However, the maximum dislocation density increases rapidly. This is because a large diaphragm induces high von Mises effective stress near the diaphragm edge. As a result, the plastic shear strain rate can be very high at the area of stress concentration.

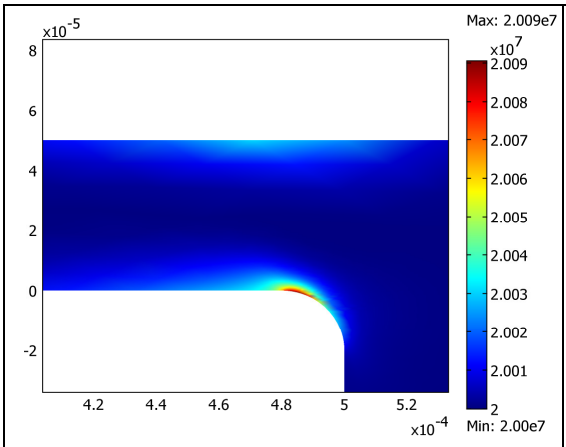

a) Radius=0.5mm

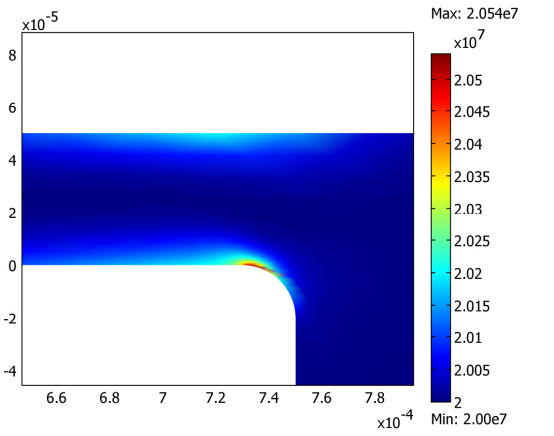

b)Radius=0.75mm

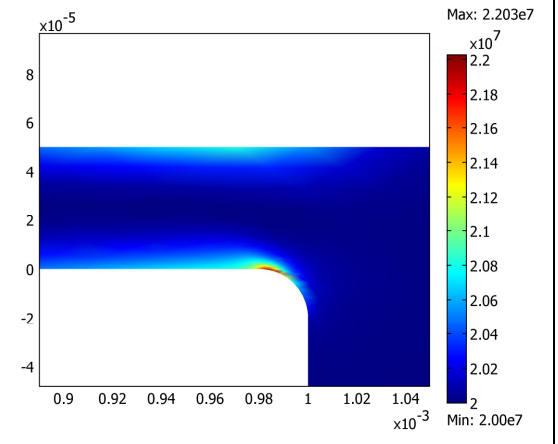

c) Radius=1.0mm

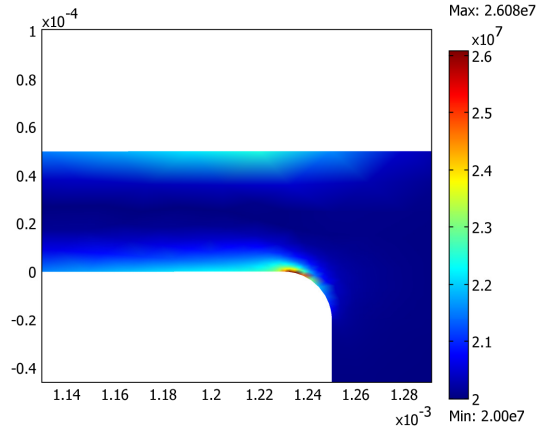

d) Radius=1.25mm

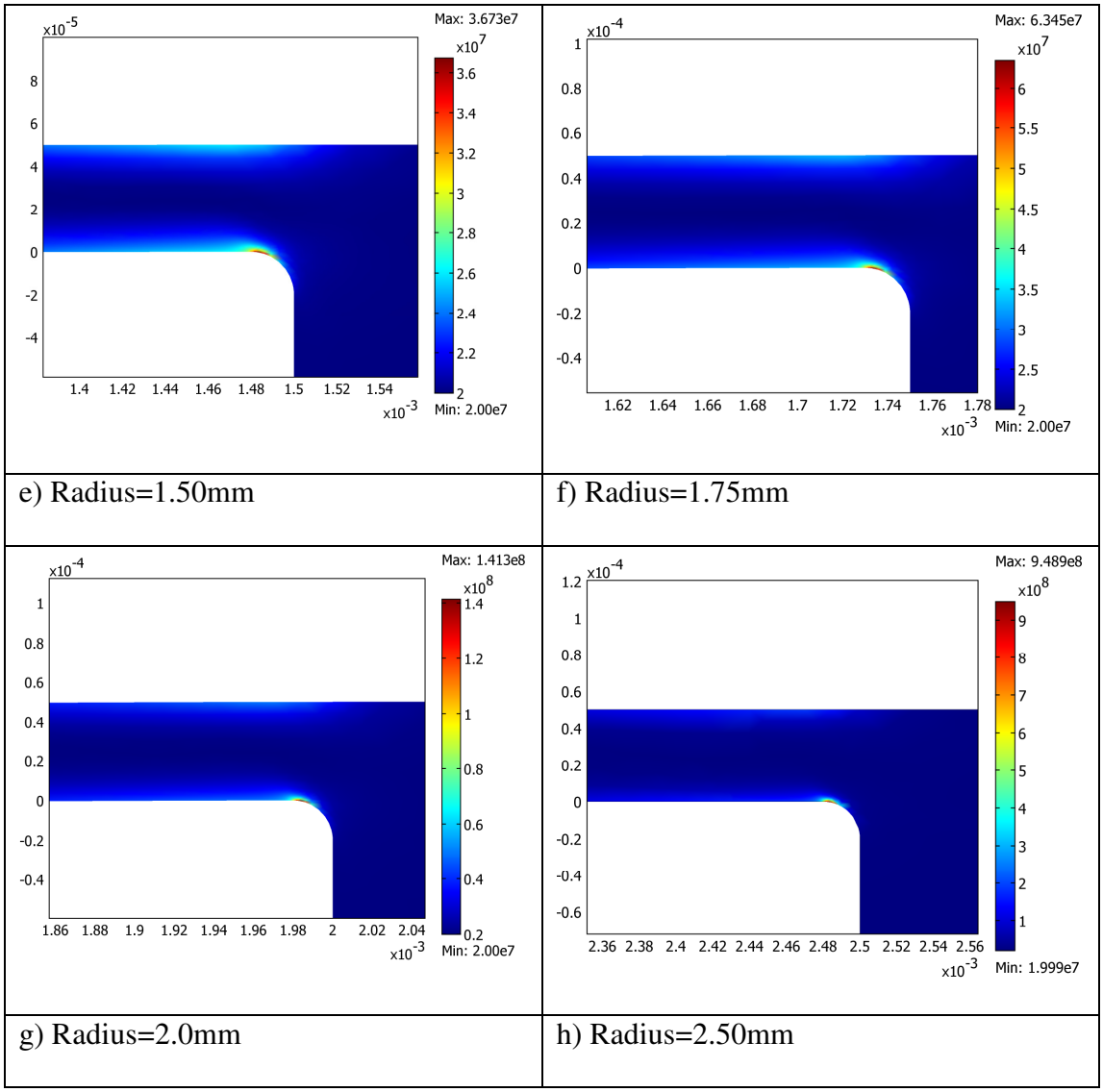

Figure 5- 7 The distribution of the dislocation density at the diaphragm edge after annealing at 800°C (1073K) for an hour

5.4.1.2 The evolution of diaphragm deflection

The main interest in the diaphragm behaviour for the micromachined pressure sensor application is the diaphragm deformation. The evolution of the maximum displacement for silicon diaphragm at 800°C with a radius of 1.75mm is shown in Figure 5- 8. The displacement is initially induced by the atmospheric pressure. The

deformation rate is very slow at the temperature ramp up stage. With the increase of the annealing temperature, the plastic shear strain rate increases, so dose the deformation rate. It can be seen that the rate of the plastic deformation is almost linear when the annealing temperature is maintained at 800°C (1073K). Then the progress of the plastic deformation slows down when the temperature ramps down.

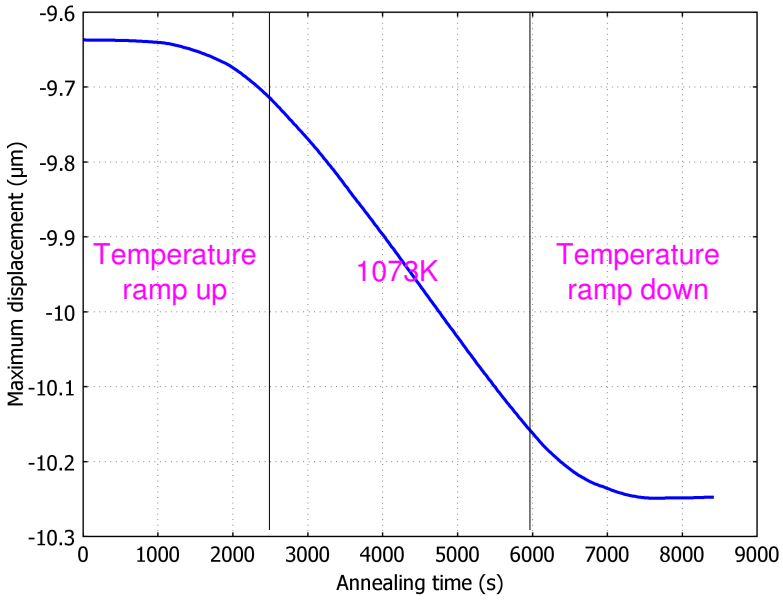

Figure 5- 8 The evolution of the maximum displacement for the diaphragm with a radius of 1.75mm when annealing at 800°C (1073K)

The deformed shapes of the silicon diaphragms before and after annealing at 800°C for one hour are predicted in
Figure 5- 9. The maximum displacement occurs at the diaphragm centre. When the radius is 1.5mm and under, the simulated structure does not show an obvious increase of maximum displacement after anneal. When the radius is 1.75mm and above, the maximum displacement after anneal is considerably larger than that before anneal. The predicted displacement increase is about 3.76μm for the structure with a radius of 2.5mm.

Before anneal	After anneal
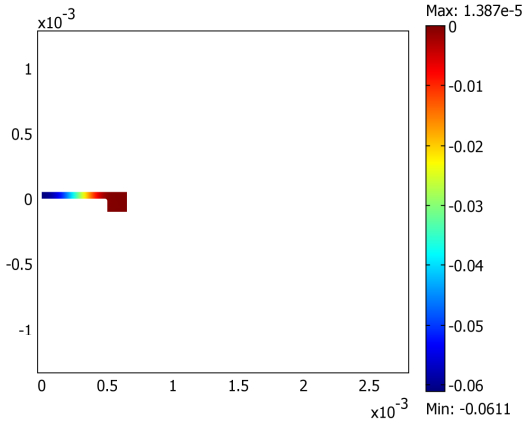	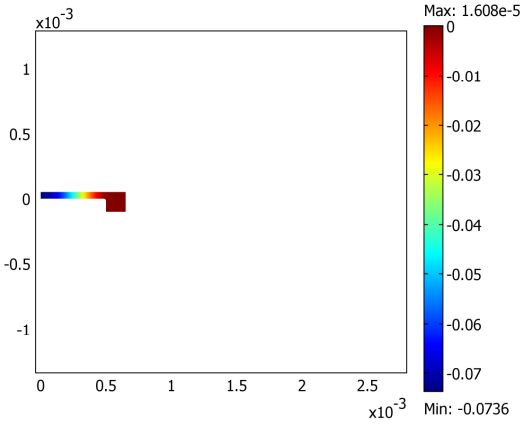
a) Radius=0.5mm	
Before anneal	**After anneal**
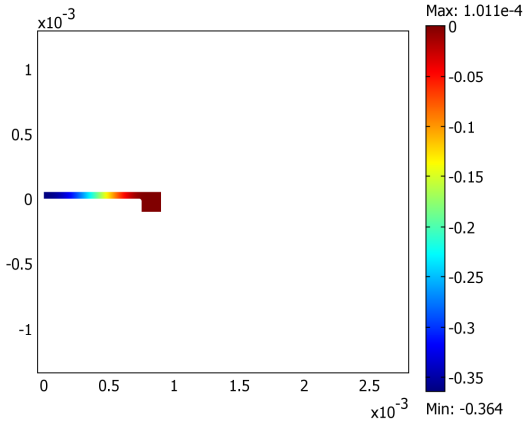	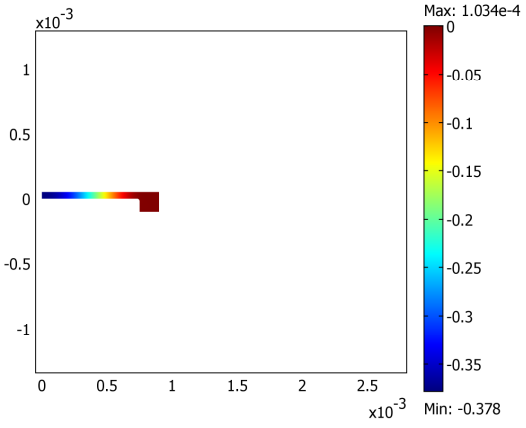
b)Radius=0.75mm	
Before anneal	**After anneal**
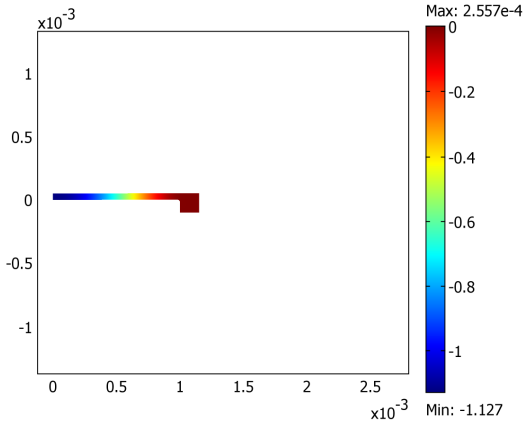	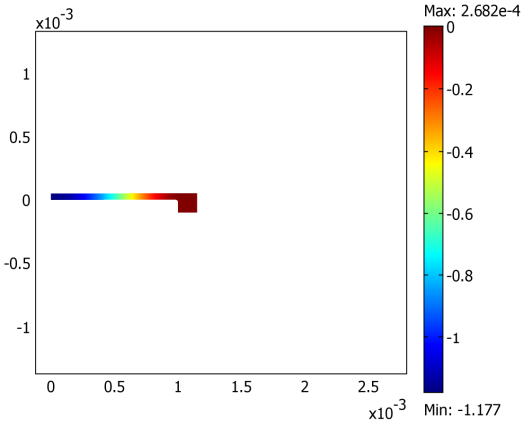
c) Radius=1.0mm	

Before anneal	After anneal
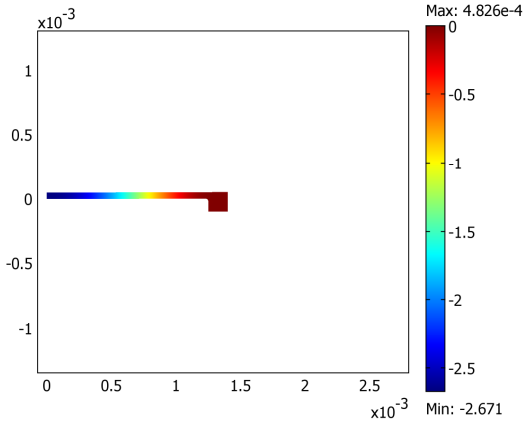	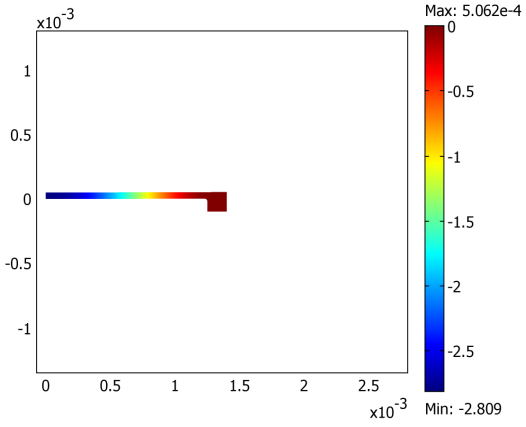

d) Radius=1.25mm

Before anneal	After anneal
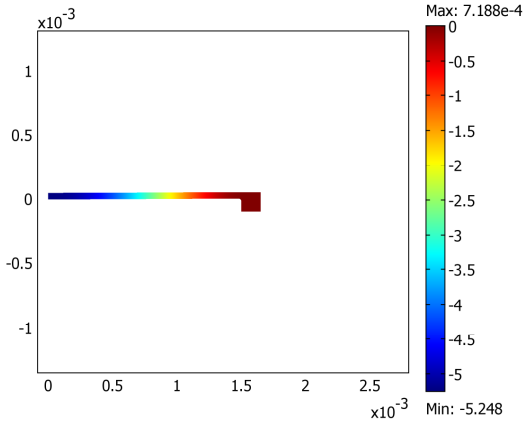	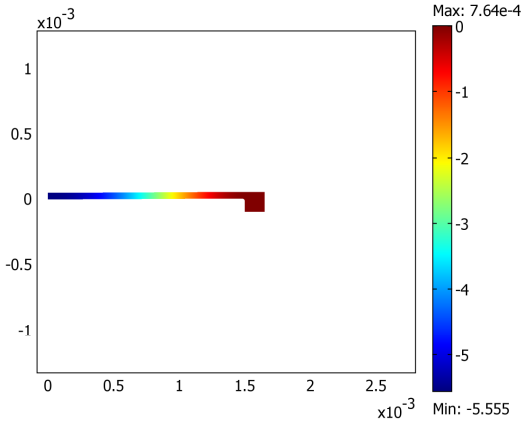

e) Radius=1.50mm

Before anneal	After anneal
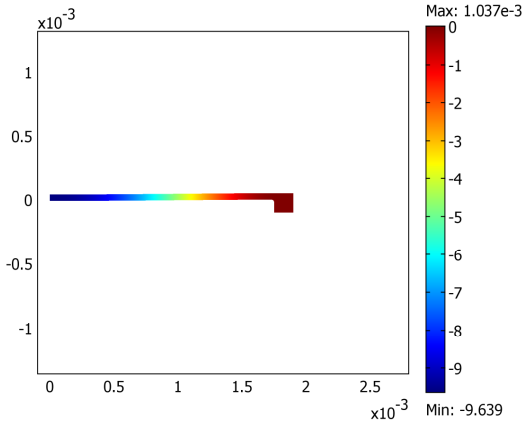	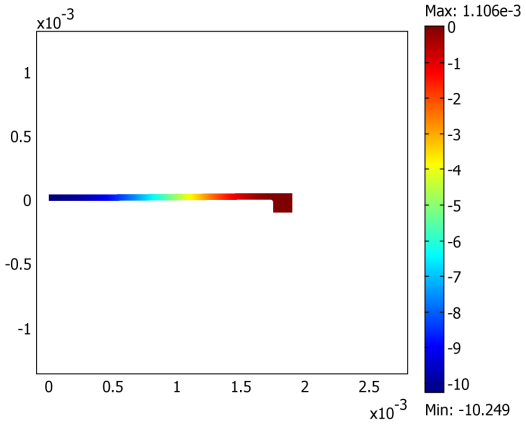

f) Radius=1.75mm

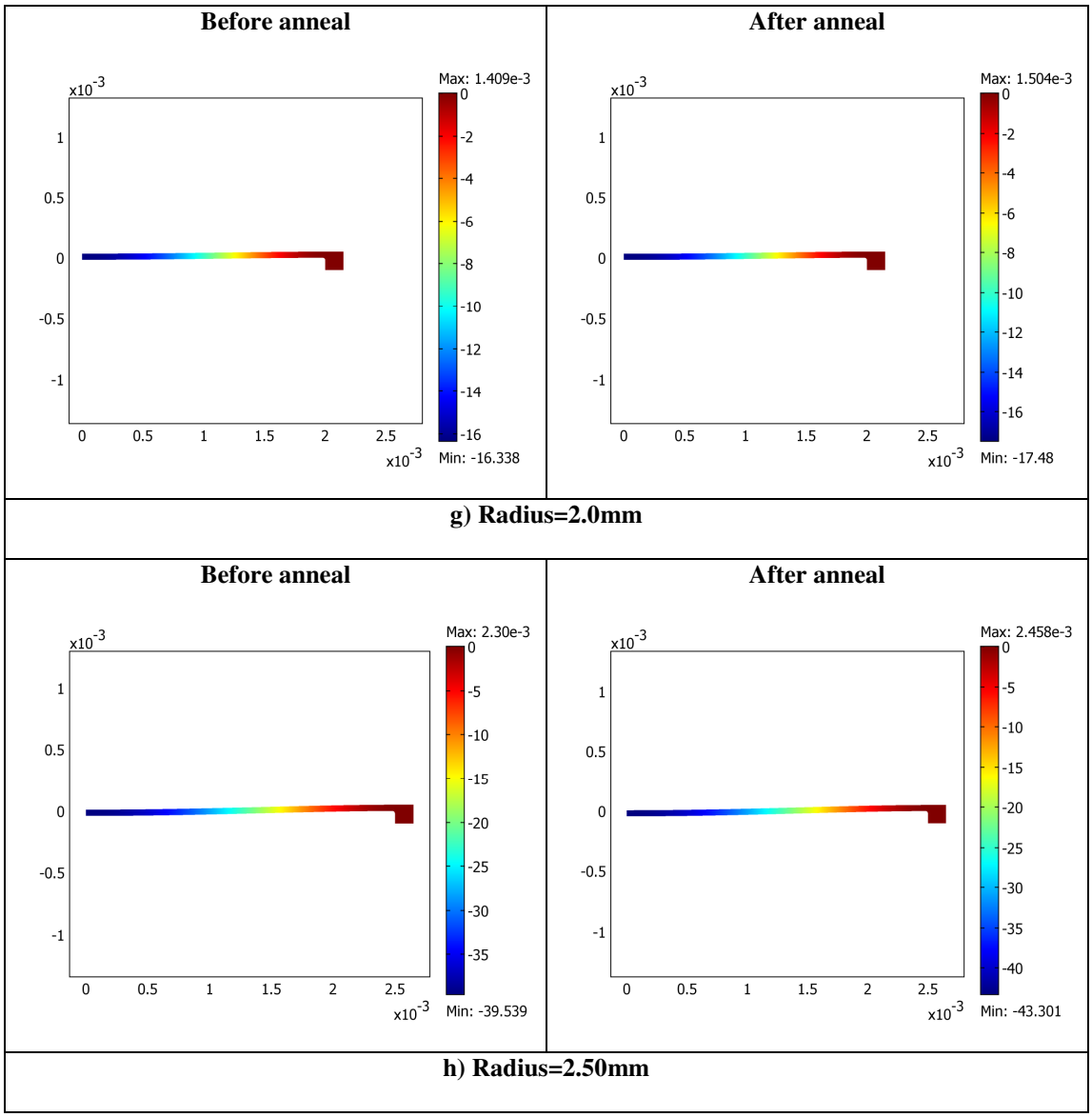

Figure 5- 9 The deformed diaphragm after annealing at 800°C (1073K) for an hour (μm)

5.4.2 Predicted diaphragm behaviour at 900℃

5.4.2.1 The distribution of the dislocation density

The dislocation density for silicon diaphragm annealing at 900°C is predicted for a variety of dimensions (0.5mm-2.5mm). The distribution near the diaphragm edge after an hour annealing is illustrated in
Figure 5- 10. The initial dislocation density is assumed to be $2.7\times10^{7}/m^{2}$. The number of dislocations grows very slowly for the diaphragms with a radius of 0.5mm and

0.75mm. The multiplication rate of dislocation density increases with the diaphragm radius. When the diaphragm radius is 2.5mm, the dislocation density is over $5\times10^{9}/m^{2}$ near the diaphragm edge, and the maximum value reaches $1.32\times10^{10}/m^{2}$.

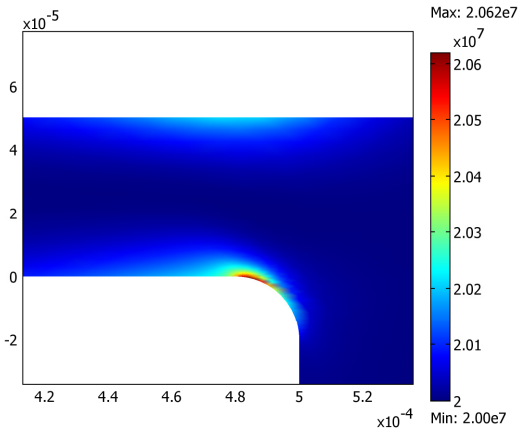

a) Radius=0.5mm

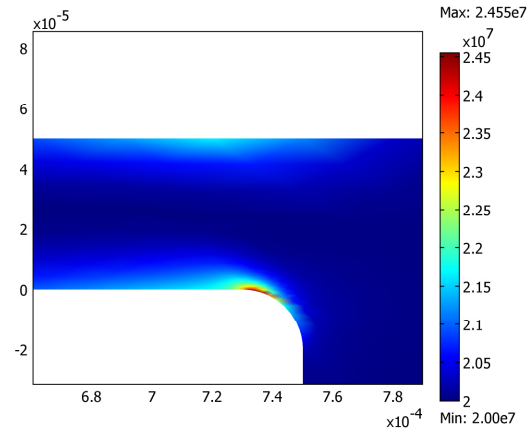

b)Radius=0.75mm

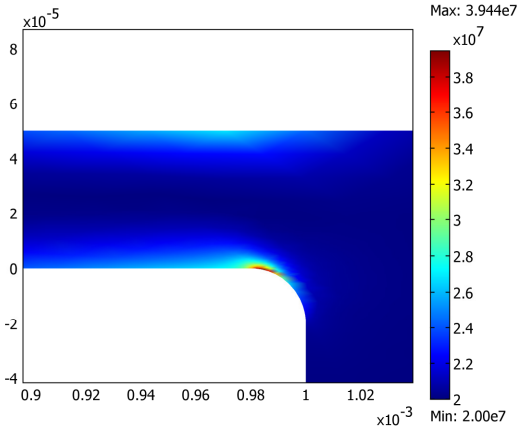

c) Radius=1.0mm

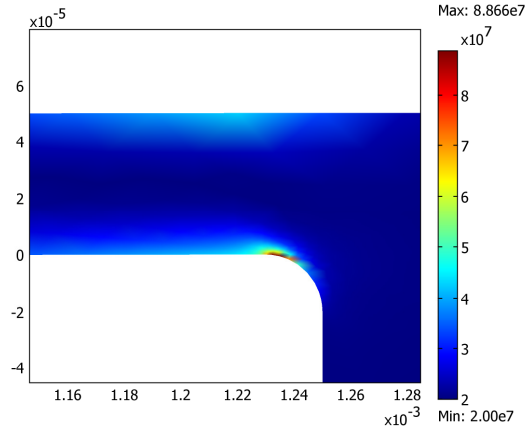

d) Radius=1.25mm

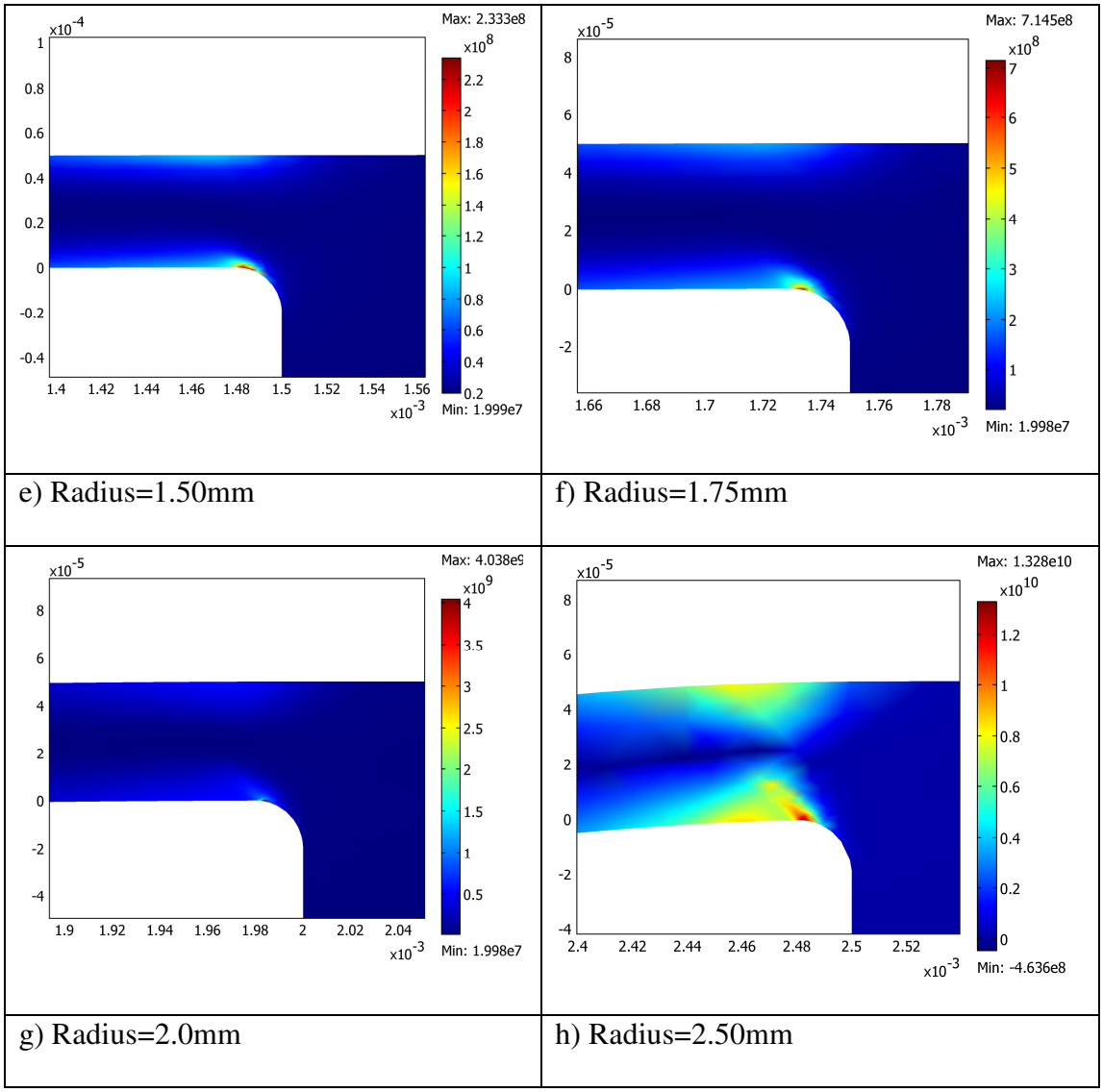

e) Radius=1.50mm

f) Radius=1.75mm

g) Radius=2.0mm

h) Radius=2.50mm

Figure 5- 10 The distribution of the dislocation density at the diaphragm edge after annealing at 900°C (1173K) for an hour

However, for the diaphragm with a radius of 2.5mm, the dislocation density becomes negative at the region close to the middle plane, as illustrated by the blue color in Figure 5- 11. In fact, the dislocation density at the blue region is very close to the initial value. Because the stress near the middle plane is very low, the dislocation multiplication rate could be very low according to Equation 5- 9, or equal to zero if the von Mises effective stress is less than the internal stress. The negative dislocation

density is an artefact of the simulation results and is caused by the convergence problem of the FEA model due to the highly non-linear material properties. In order to prevent numerical overshoot in the value of dislocation density, a refined mesh at the location with high stress concentration is applied. The absolute value of the dislocation density is used for Equation 5- 7 in order to avoid the root of a negative.

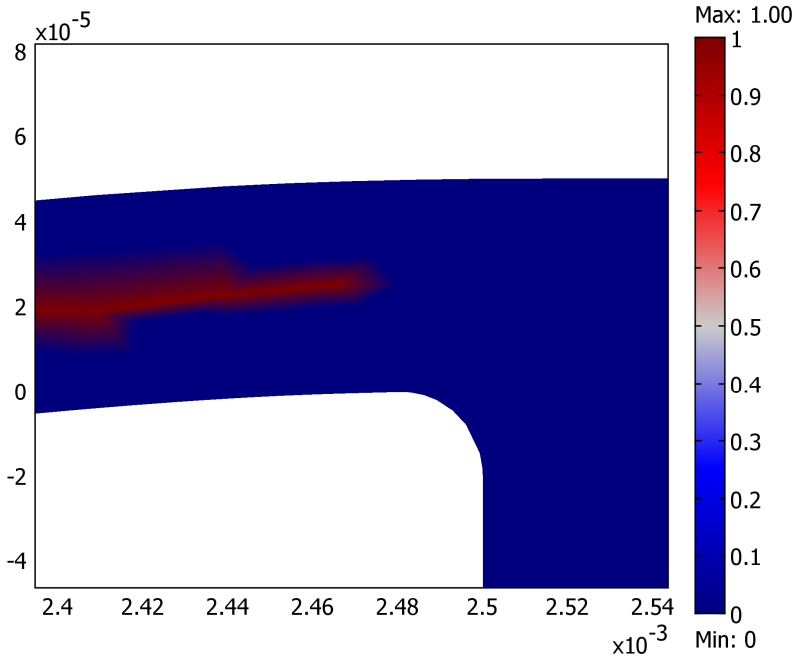

Figure 5- 11 The deformed geometry at edge for the diaphragm with a radius of 2.5mm after annealing at 900°C. (The positive dislocation density is illustrated by the blue color while the negative dislocation density is illustrated by the red color)

5.4.2.2 The evolution of diaphragm deflection

The evolution of the maximum displacement at 900°C for the silicon diaphragm with a radius of 1.75mm is shown in Figure 5- 12. The displacement is initially induced by the atmospheric pressure. The deformation rate is very slow at the temperature ramp up stage. With the increase of the annealing temperature, the plastic shear strain rate increases. It can be seen that the deformation rate is much faster when the annealing

temperature is maintained at 900°C (1173K). Then the progress of the plastic deformation slows down when the temperature ramps down.

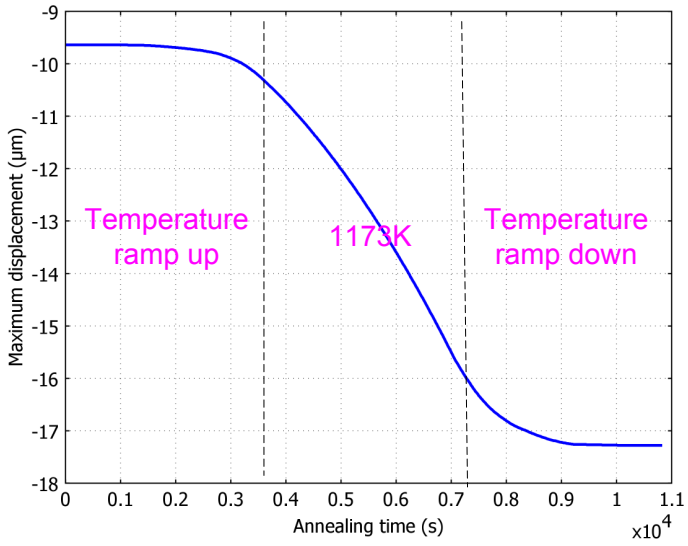

Figure 5- 12 The evolution of the maximum displacement for the diaphragm with a radius of 1.75mm when annealing at 900°C (1173K)

The deformed shapes of the silicon diaphragms before and after annealing at 900°C for one hour are predicted in Figure 5- 13. The maximum displacement takes place at the diaphragm centre. The simulated structure shows an obvious increase of maximum displacement after anneal. The predicted displacement after anneal is about 318μm for the structure with a radius of 2.5mm. The displacement field of the diaphragm can also be illustrated in 3 dimensions, as shown in Figure 5- 14.

Before anneal	After anneal
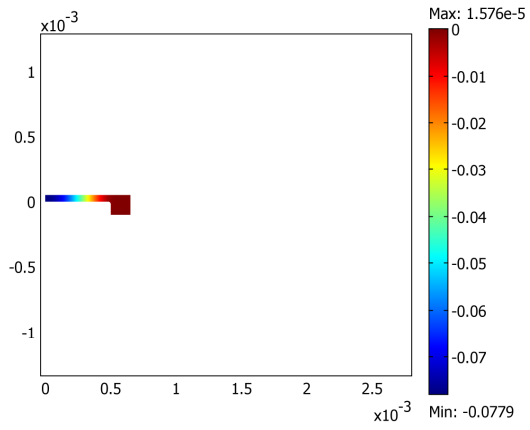	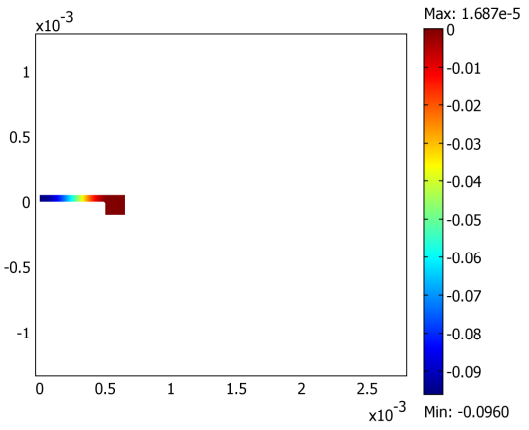
a) Radius=0.5mm	
Before anneal	**After anneal**
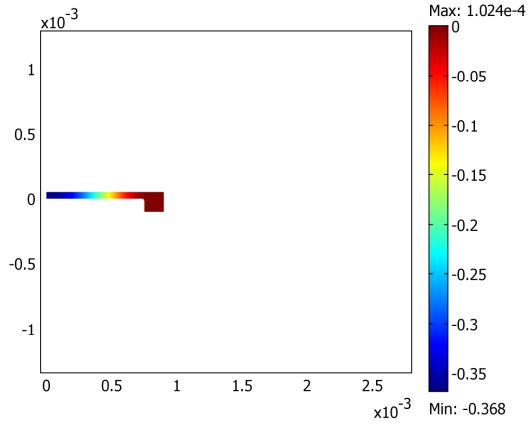	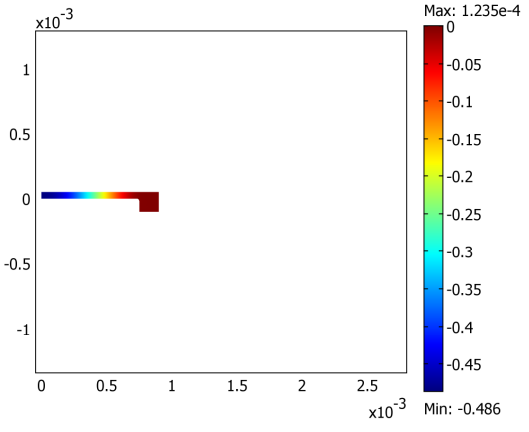
b)Radius=0.75mm	
Before anneal	**After anneal**
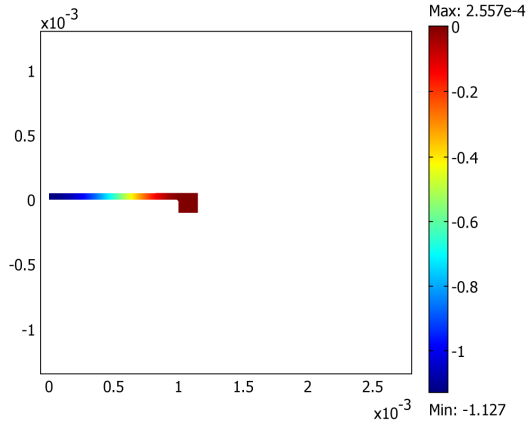	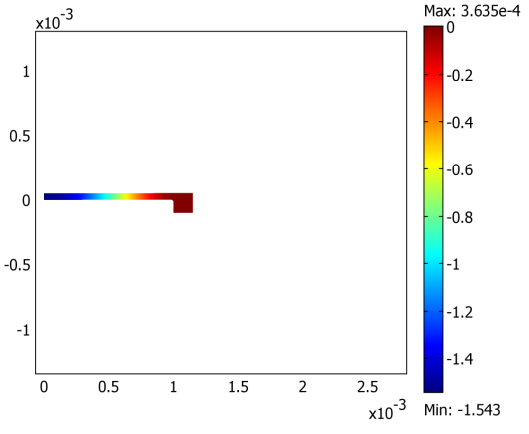
c) Radius=1.0mm	

Before anneal	After anneal
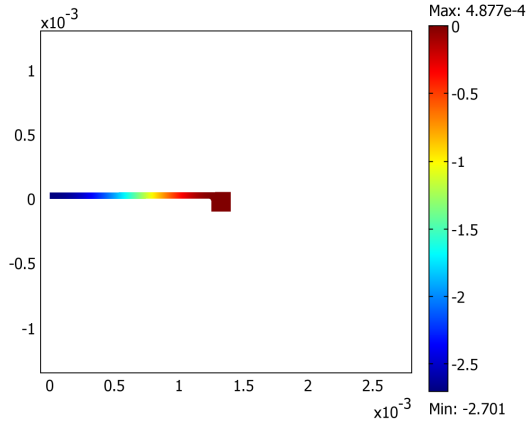	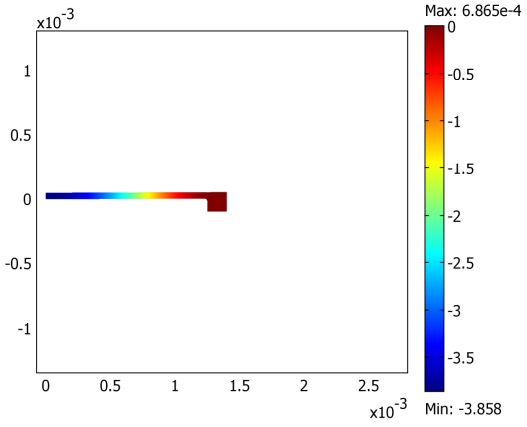
d) Radius=1.25mm	
Before anneal	**After anneal**
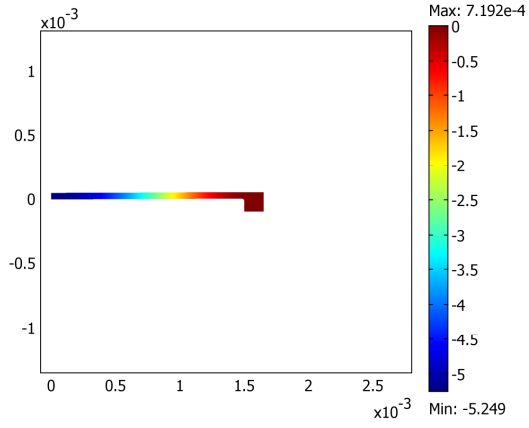	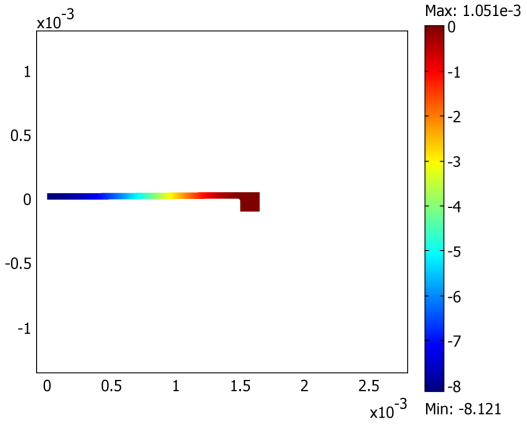
e) Radius=1.50mm	
Before anneal	**After anneal**
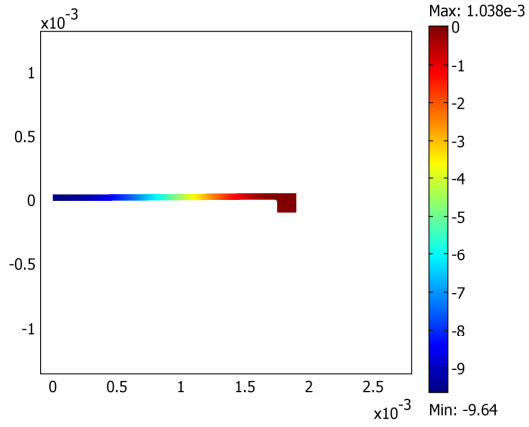	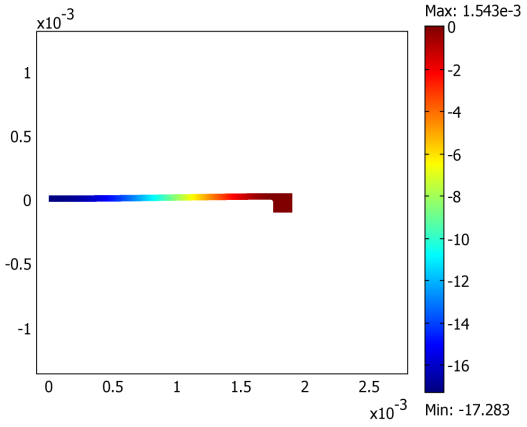
f) Radius=1.75mm	

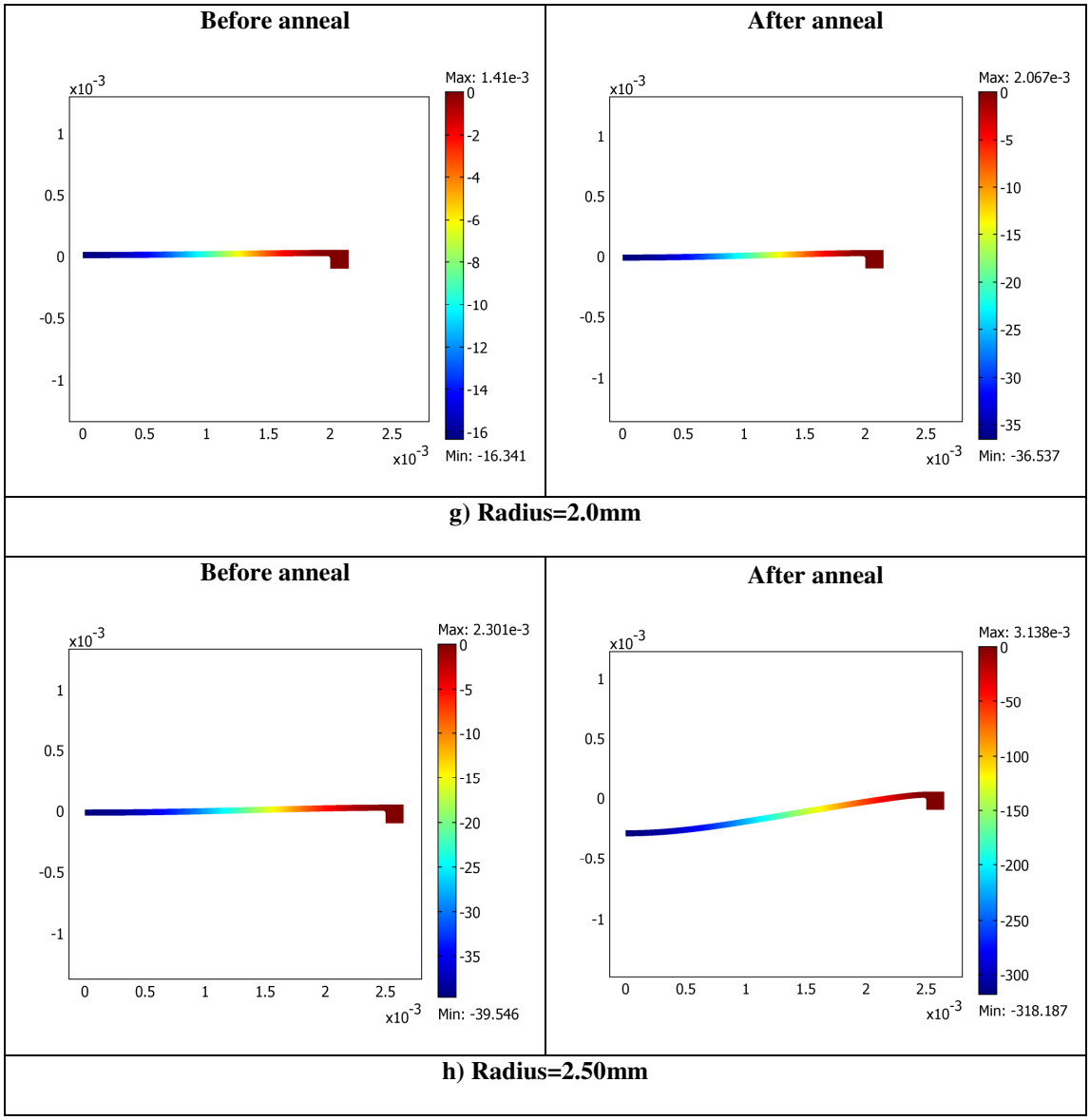

Figure 5- 13 The deformed diaphragm after annealing at 900°C (1173K) for an hour

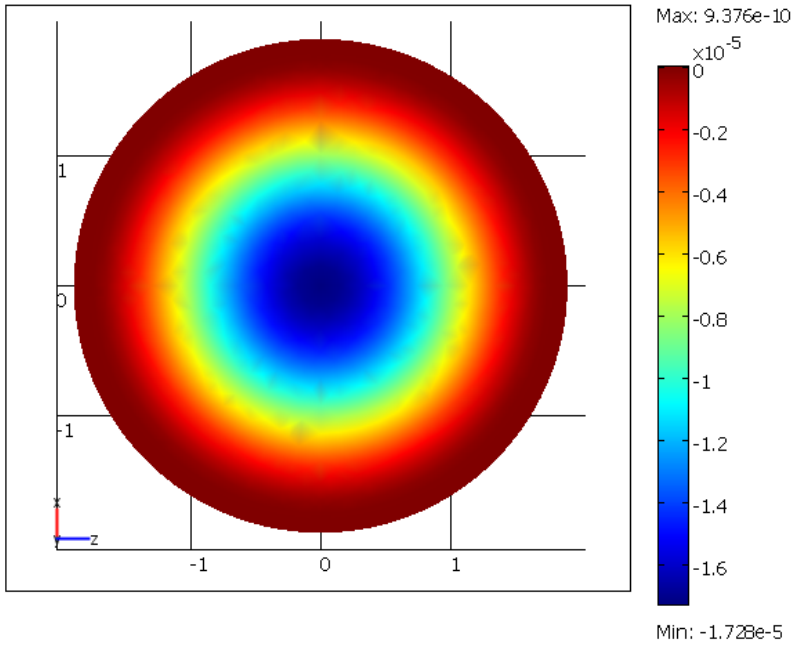

Figure 5- 14 The displacement field of the diaphragm in 3D (radius=1.75mm) at 900°C

5.5 *Conclusions*

A finite element model is built to predict the early plastic behaviour of micromachined silicon diaphragms at a temperature of 800°C and 900°C respectively. The model is based on the constitutive equations proposed by Alexander and Hassen. This model uses two PDE general form modes coupled with the stress-strain application mode. The plastic strain is determined by the plastic shear strain rate, which is related to the evolution of the dislocation density. The dislocation density and evolution of diaphragm displacement are obtained for the diaphragm with radii from 0.5mm to 2.5mm.

List of References

[5-1] Moon H-S, Anand L, Spearing SM. A constitutive model for the mechanical behavior of single crystal silicon at elevated temperatures. In: Mat Res Soc Symp Proc 687, Paper B9.6, 2002

[5-2] Alexander H and Haasen P, Dislocation and plastic flow in the diamond structure, SOLID STATE PHYS 1968; 22:27–158

[5-3] Myshlyaev MM, Nikitenko VI, Nesterenko VI, Dislocation structure and macroscopic characteristics of plastic deformation at creep of silicon crystals, PHYSICA STATUS SOLIDI 1969; 36: 89-95

[5-4] Cacho F, Orain S, Cailletaud G, Jaouen H, A constitutive single crystal model for the silicon mechanical behavior: applications to the stress induced by silicided lines and STI in MOS technologies, MICROELECTRON RELIAB 2007; 47: 161-167

[5-5] Lohonka R, Vanderschaeve G, Kratochvíl J, Modelling of the plastic behaviour of III-V compound semiconductors during compressive tests, MAT SCI ENG A-STRUCT 2002; 337(1-2): 50-58

[5-6] Bower A F. Applied Mechanics of Solids. Boca Raton: CRC press; 2010

[5-7]Orowan E, Problems of plastic gliding, Philos.Trans. R. Soc. London A 52: 8-22.

[5-8] Hull R, Properties of Crystalline Silicon. London: INSPEC; 1999

[5-9] Imai M and Sumino K. In situ X-ray topographic study of the dislocation mobility in high-purity and impurity-doped silicon crystals. PHILOS MAG A 1983; 47: 599-621

6 DISCUSSION OF THE MATHEMATICAL MODELS IN SILICON DIAPHRAGM DEFLECTION

6.1 *Introduction*

This chapter discusses the use of the mathematical models in predicting the silicon diaphragm behaviour. In chapter 3, the load-deflection behaviour of silicon diaphragms has been simulated by both the theoretical models and the finite element models. Moreover, the occurrence of the plastic deformation has been predicted with the aid of the finite element method. In chapter 5, a constitutive model has been used to simulate the rate of the plastic deformation for silicon diaphragms at 800°C and 900°C. The results from these models provide useful reference data in the diaphragm design and the measurement stage. However, the quality of these models needs to be evaluated. Therefore, in this chapter all the predicted results are compared with the experimental results and the implementation of the mathematical models is discussed.

6.2 *Validation of the elastic models*

Analytical modelling of the pressure induced deformation for orthotropic diaphragms is not easy. The complicated elastic properties for single crystal silicon make the mathematical work tedious and difficult especially when the diaphragm deflection is large. So the current orthotropic model is limited to small diaphragm deflections (see Equation 3-7 and 3-8 in section 3.3.2).

The diaphragm behaviour of the test structure can be approximated by the finite element method. Firstly, the boundary conditions for the silicon diaphragm are much

closer to the real sample when the whole test structure is modelled. In order to reduce the computational memory, a quarter of the test structure is modelled in this case with symmetrical boundary conditions. Secondly, the solutions for the structure with complex geometry and orthotropic elastic properties are obtainable by finite-element analysis. However as with all modelling the reliability of the results depends on the model and the input data.

The surface profiles of the test samples were measured under atmospheric pressure at room temperature. Figure 6- 1 compares the simulation results with the average value of the measured deflections. Because the deflection is large when the diaphragm radius is 2mm and 2.5mm, the analytical results of small deflection are not useful. It can be seen that there is a reasonable match between the theoretical predications and experimental observations.

The deflections for the heavily-boron-doped silicon diaphragms (with the resistivity of 0.001 ohm-cm) are larger than those for the lightly-boron-doped silicon diaphragms (with the resistivity of 1000 ohm-cm). This can be caused by the internal stress induced by the boron dopant. However, because the elastic properties of pure silicon crystal are used in the mathematical models, the dopant induced internal stress is not considered. So results from both the FEA model and the analytical model are smaller than the average value of the measured deflections. But it is apparent that the FEA model gives much closer approximation than the analytical model. The results imply that the elastic behaviour of MEMS structures not only depends on the material properties, but also depends on the micromachining processes, such as doping, etching and wafer bonding.

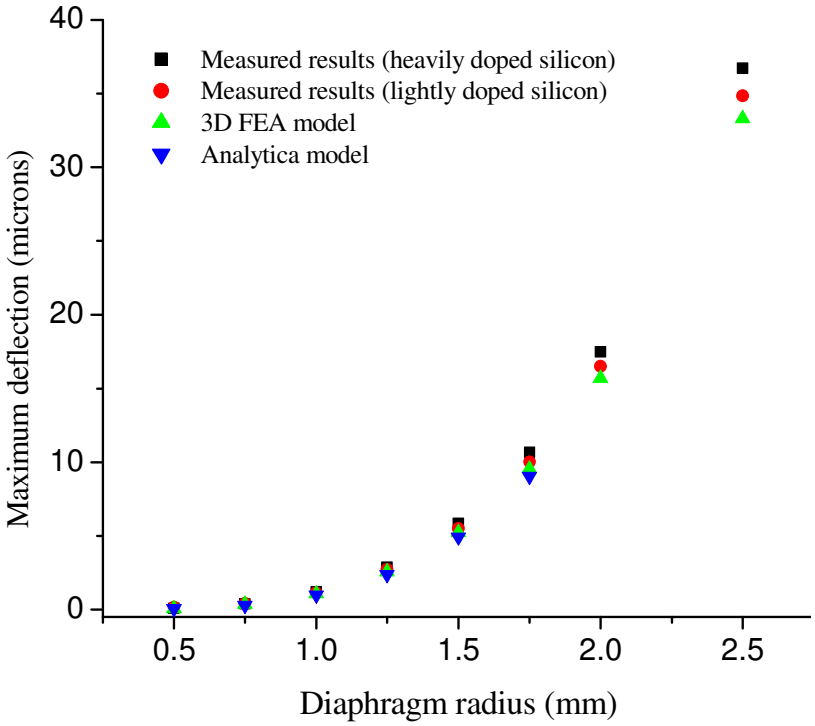

Figure 6- 1 Comparison of simulation results with average measured deflections

6.3 *Evaluation of the occurrence for plastic deformation*

The occurrence of the plastic deformation in the silicon diaphragms can be predicted by analysing the resolved shear stress which is induced by the atmospheric pressure at the operating temperature. Wherever the acting resolved shear stress exceeds the yield strength at the operating temperature, the silicon diaphragm deforms plastically by the crystallographic slip of the dislocations. A three dimensional FEA model has been used to calculate the resolved shear stresses on all the slip systems (section 3.4.1). The model of the test structure is built with ideal conditions. The silicon material is defined as perfect single crystal without any internal stresses, and the temperature and the pressure are distributed evenly across the structure. Since the stress induced in the diaphragms relates to the diaphragm sizes, the diaphragm behaviour was predicted as

a function of the diaphragm radius and the operating temperature (600°C-1000°C) (Figure 3-14).

The prediction behaviour is evaluated in Table 6- 1 using the experimental observation from the heavily-boron-doped silicon (with the resistivity of 0.001 ohm-cm). The mechanical behaviour of the silicon diaphragms was studied experimentally in section 4.5 at a temperature of 600°C (137hs), 800°C (31hs) and 900°C (21hs). The experimental conditions are not perfect, because there are ramp up stage and ramp down stage during the annealing steps at 800°C and 900°C.

Table 6- 1 Evaluation of the prediction behaviour using experimental observation from the heavily-boron-doped silicon diaphragms

Elevated temperature behaviour										
Radius	***600℃***		***700℃***		***800℃***		***900℃***		***1000℃***	
(mm)	P	***O***	P	***O***	P	***O***	P	***O***	P	***O***
0.50	E	***E***	E		E	***E***	E	***E***	E	
0.75	E	***E***	E		E	***E***	E	***E***	E+P	
1.00	E	***E***	E		E	***E***	E	***E***	E+P	
1.25	E	***E***	E		E	***E***	E+P	***E+P***	E+P	
1.50	E	***E***	E		E	***E***	E+P	***E+P***	E+P	
1.75	E	***E***	E		E+P	***E+P***	E+P	***E+P***	E+P	
2.00	E	***E***	E		E+P	***E+P***	E+P	***E+P***	E+P	
2.50	E	***E+C***	E		E+P	***E+P***	E+P	***E+P***	E+P	

(P stands for 'Prediction'; O stands for 'Observation'; E stands for 'Elastic deformation'; C stands for 'Creep'; P stands for 'Plastic deformation')

Current observation shows that the method using resolved shear stress to predict the onset of the plastic deformation is reliable for silicon diaphragms. This method can be a useful tool to predict the elastic failure of Si MEMS structures for elevated temperature environment, especially at the designing stage. The accuracy of the method can be improved by including the actual material properties and the real

experimental conditions in the settings of the FEA model. However, this may make the computation of solutions difficult, especially for complicated silicon device structures. Finally, creep deformation must be considered if the device has to operate at a temperature over 600°C for a long period of time.

6.4 *Validation of the constitutive model in FEA*

A finite element model is built to predict the behaviour of micromachined silicon diaphragms in the first annealing stage (annealing stage A for one hour) at a temperature of 800°C and 900°C in chapter 5. The deformation caused by the temperature ramps of the furnace is also included. The density of the moving dislocations is an important variable because its distribution governs the early plastic deformation, according to the Alexander and Hassen's model. The simulated dislocation density can be evaluated by observing dislocations in the transmission electron microscope (TEM). However, the preparation of TEM samples will damage the test structures for the following experiments. As a result, it was not implemented in the experiments.

For pressure sensor applications, the evolution of the diaphragm deformation is the main concern since it may affect the device output. Due to the experimental limitations, the diaphragm deformation was measured before annealing and after annealing, but not during the process of annealing. However, comparison of the simulated deformation with the measured data is still an effective way to test the constitutive model.

6.4.1 Evaluating the results at 800℃

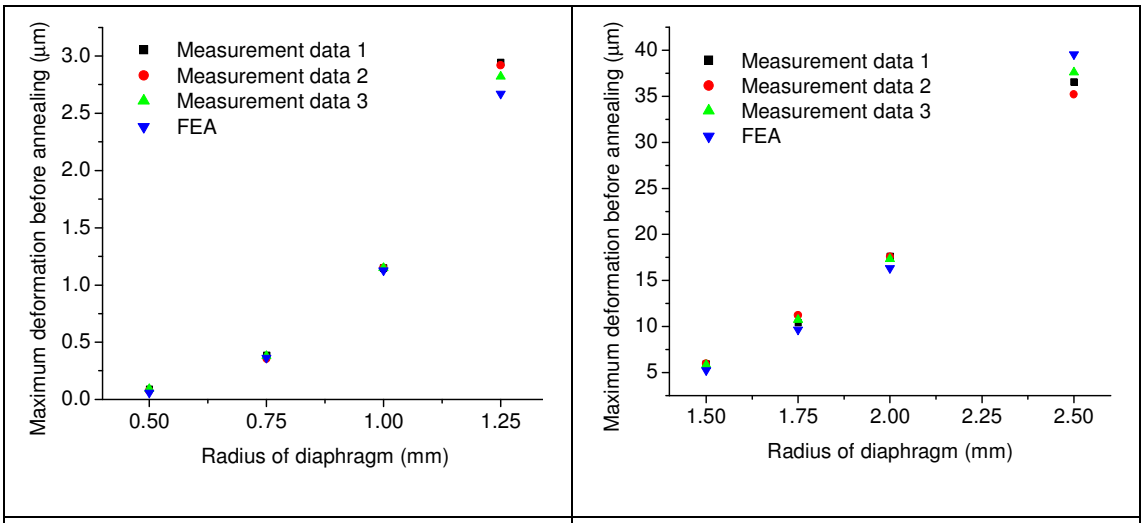

a) Radius from 0.5mm to 1.25mm

b) Radius from 1.50mm to 2.50mm

Figure 6- 2 The comparisons of model prediction and experimental data for the diaphragm displacement before annealing at 800°C

Figure 6- 2 illustrates the comparisons between the predictions from the constitutive model and the measured displacements before annealing at 800°C. It indicates a good match between the simulated and the measured data.

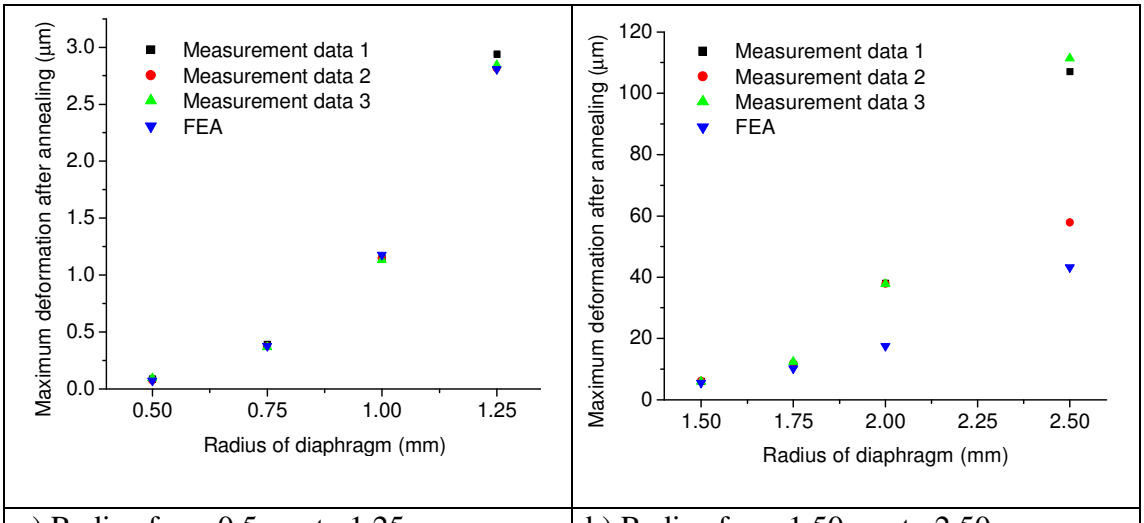

a) Radius from 0.5mm to 1.25mm

b) Radius from 1.50mm to 2.50mm

Figure 6- 3 The comparisons of model prediction and experimental data for the diaphragm displacement after annealing at 800°C

Figure 6- 3 shows the comparisons between the predictions from the constitutive model and the measured displacements after annealing at 800°C for one hour (after anneal stage A). It can be seen that the predicted maximum displacements are in close agreement with the measured points for the diaphragms with a radius in the range of 0.5mm to 1.50mm. Because the model predicts very slow growth of the dislocation density in these diaphragms, the deformation after annealing does not show much difference from that before annealing. And according to the experiment results, no measurable plastic deformation is observed at 800°C for these diaphragms. So it is not a surprise that the prediction is very close to measured data.

When the diaphragm radius is from 1.75mm to 2.5mm, apparent increase of the diaphragm deflection was noticed in the first hour of annealing. However, the simulated results underestimate the plastic deformation during annealing, especially for the diaphragms with a radius of 2mm and 2.5mm. By applying current settings in the constitutive model, the simulated growth of the dislocation density is slow. So the predicted plastic deformation is very small. Because the model fails to simulate the plastic deformation in the annealing process, it is not valid for the behaviour of silicon diaphragms at a temperature of 800°C.

6.4.2 Evaluating the results at 900°C

Figure 6- 4 shows the comparisons between the predictions from the constitutive model and the measured displacements before annealing at 900°C. There is a good match between the simulated data and the measured data.

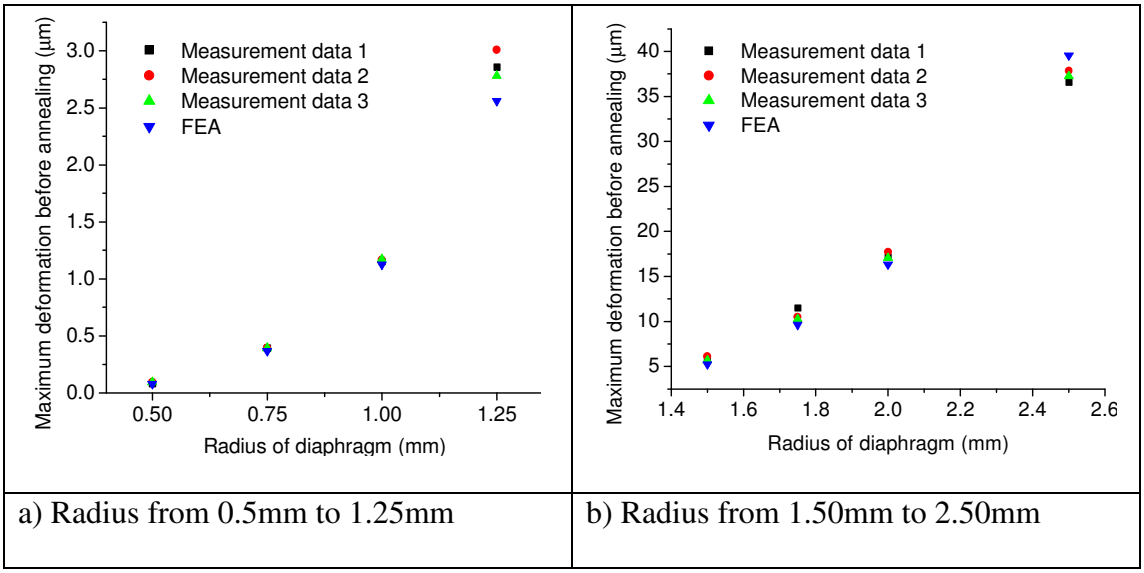

a) Radius from 0.5mm to 1.25mm

b) Radius from 1.50mm to 2.50mm

Figure 6- 4 The comparisons of model prediction and experimental data for the diaphragm displacement before annealing at 900°C

Figure 6- 5 shows the comparisons between the predictions from the constitutive model and the measured displacements after annealing at 900°C for one hour. Here the diaphragm radius is in the range of 0.5mm to 2.0mm. It can be seen that the predictions generally agree to the measured points. For the diaphragms with radii from 0.5mm to 1.0mm, a small amount of plastic deformation is predicted by the model. But according to experiment results, no measurable plastic deformation was observed for these diaphragms. However, the simulated results are acceptable because the constitutive model is based on several assumptions, and the exact prediction is not easy. A considerable amount of plastic deformation was observed in the experiment for the diaphragms with radii from 1.25mm to 2.0mm. From Figure 6- 5(b), it can be seen that the simulated deformations match well with the measured points.

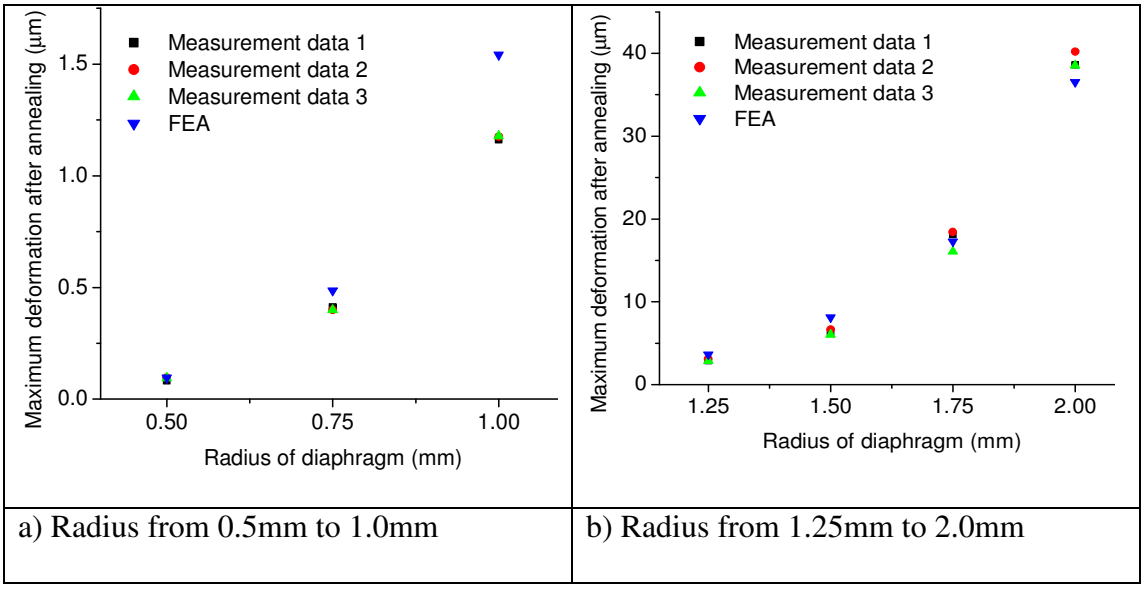

a) Radius from 0.5mm to 1.0mm

b) Radius from 1.25mm to 2.0mm

Figure 6- 5 The comparisons of model prediction and experimental data for the diaphragm displacement after annealing at 900°C

The evolution of the displacement for the diaphragm with a radius of 2.5mm is shown in Figure 6- 6. The maximum displacement after annealing is predicted as 318μm. This value is much larger than the measured average value of about 110μm. The huge gap between the prediction and the measurement is caused by the interaction of the dislocations. It is known that the larger the diaphragm radius, the larger the induced shear stress. So the dislocations in the diaphragm can multiply quickly under the applied stress. After the density of the dislocations reach a high level after a short period of annealing, the dislocations begin to interfere with one another's movement, and the progress of the plastic deformation is therefore impeded. But the constitutive model does not consider effect of the slip resistance on the plastic deformation, the prediction after annealing appears to be extremely large. Therefore, the model is not valid for the behaviour of silicon diaphragms with a radius larger than 2.5mm at temperature of 900°C.

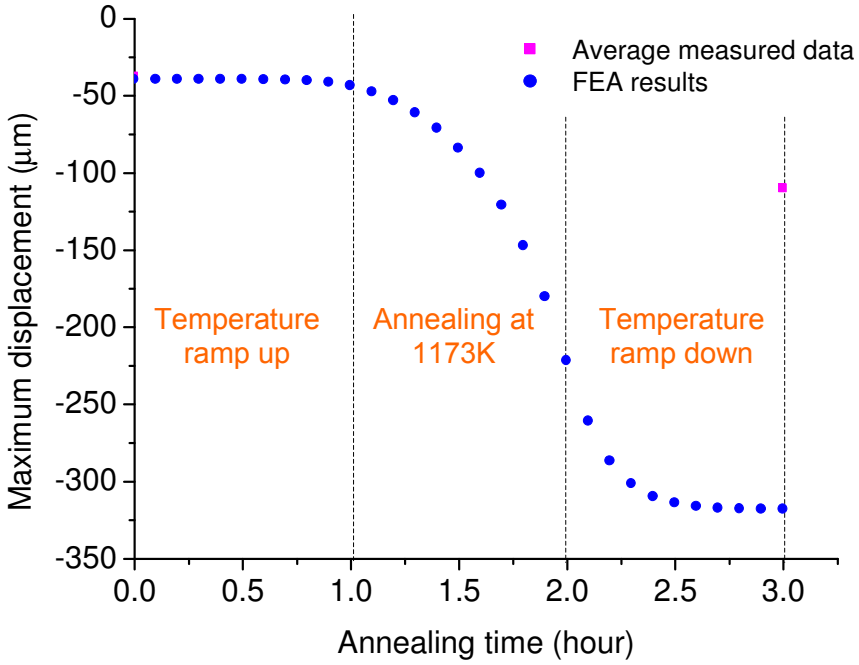

Figure 6- 6 The evolution of the maximum displacement with time (radius=2. 5mm)

6.5 *Conclusions*

This chapter validates the mathematical models used in this work for predicting the mechanical behaviour of silicon diaphragms. Analytical modelling of the elastic deformation for isotropic diaphragms is usual. However, when the material is orthotropic, the mathematic analysis tends to be complicated. The 3-dimentional FEA model gives a much closer approximation of the diaphragm behaviour, and the accuracy of the results can be improved by considering the effect of MEMS manufacturing processes.

The method using resolved shear stress to predict the onset of the plastic deformation is reliable for silicon diaphragms. For a given diaphragm radius at 600°C, 800°C or 900°C, the predicted behaviour is in good agreement with the experimental

observation. The validation of the model is based on the accurate prediction of the resolved shear stress by the aid of the finite element method.

A constitutive model has been used to simulate the magnitude of the plastic deformation for silicon diaphragms in the first hour of annealing. The model fails to predict the mechanical behavior at a temperature of 800°C because the simulated increase of the displacement is much smaller than the measured data. When the operating temperature is 900°C, there is a fairly good match between the theoretical predications and experimental observations for the diaphragms with a radius from 0.5mm to 2.0mm. However, it is not valid for the diaphragm with a radius of 2.5mm because the generated dislocation density is very high, and the slip resistance should be considered.

7 CONCLUSIONS AND RECOMMENDATIONS FOR FUTURE WORK

This project aims to investigate the possibility to apply silicon diaphragms in high temperature pressure sensors. Thus, the elevated temperature behaviour of micromachined silicon diaphragms is studied in the work. The thesis provides a comprehensive understanding of the diaphragm behaviour from mechanical engineering point of view. The content covers a wide range of topics, including the summary of silicon properties and characterization methods, the experimental design and observation, and the mathematical modelling. This chapter summarizes the major conclusions obtained during the research, and outlines the direction for the future research.

7.1 *Conclusions*

The micromachined pressure sensor which can operate in high temperature environment is increasing demanded by the developing of industries. The overview of previous research suggests that the development of high temperature low-cost pressure sensor is desirable because current devices which apply SiC or SOI materials are very expensive. Evidence has shown that a piezeoresistive pressure sensor which is based on the silicon diaphragm could work properly at 500°C with very low pressure hysteresis [7-1]. The key of the design is the choosing of the diaphragm dimensions, so that the diaphragm will not deform plastically at high temperature and

high pressure environment. However, from the literature, the mechanical behaviour of silicon diaphragms at high temperatures has not previously been studied in detail. So the characterization work in this study is valuable to the development of MEMS devices for harsh environments.

A series of experiments were performed to investigate the diaphragm deflection with anneal time at the anneal temperature of 600°C (137 hours), 800°C (31 hours not including temperature ramps) and 900°C (21 hours not including temperature ramps), respectively. The radius of the micromachined silicon diaphragms is from 0.5mm to 2.5mm. The thickness of the diaphragms is 50μm. All the diaphragms were stressed by the application of the atmospheric pressure during measurement and anneal process. The measured results at room temperature show that the deflections for the heavily doped diaphragms (with the resistivity of 0.001 ohm-cm) are larger than those for the lightly doped diaphragms (with the resistivity of 1000 ohm-cm) due to the internal stress caused by the boron dopant. For heavily doped silicon, the experiment results imply that: a) the creep deformation at 600°C can be destructive for diaphragms under high stress, because significant creep has been observed for the diaphragm with a radius of 2.5mm after annealing for 69 hours; b) at 800°C, the radius of the diaphragm should be limited to be under 1.5 mm in order to avoid plastic deformation; c) at 900°C, the radius of the diaphragm should be limited to be under 1mm, because the deformation rate is so high that larger diaphragms deteriorated in the first hour of anneal due to the occurrence of the plastic deformation. For lightly doped silicon, the experiment results imply that: the ion implanted silicon is more likely to deform plastically due to the extended defects which formed after ion

implantation and annealing of silicon. The experiment provides valuable reference data for the diaphragm design of high temperature pressure sensors.

The elastic deformation of the pressurized silicon diaphragm at room temperature has been simulated by both analytical and finite element methods. Due to the orthotropic elastic properties of silicon, the theoretical analysis of the diaphragm deformation is not easy, and the small deflection is approximated by applying equivalent properties of silicon in the solutions for isotropic diaphragms. By comparing the simulated results with the experimental deflections, it is found that the 3D orthotropic FEA model gives a much closer approximation.

Based on the reported critical resolved shear stress of silicon, the onset of the plastic deformation is predicted by the aid of FEA software Comsol Multiphysics 3.5a. For a given diaphragm dimension, the resolved shear stress under atmospheric pressure is calculated for each slip system. The diaphragm behaviour is predicted with a temperature between 600°C and 1000°C. For a given diaphragm radius at 600°C, 800°C and 900°C, the predicted behaviour is in good agreement to the experimental observation. Therefore, the method used has been shown to be a very useful tool in the primary design of the diaphragm dimensions.

Most importantly, a finite element model is built in Comsol Multiphysics to predict the early plastic behaviour of micromachined silicon diaphragms. The model is based on the constitutive equations proposed by Alexander and Hassen. The plastic strain is determined by the plastic shear strain rate, which is related to the evolution of the

dislocation density. The dislocation density distribution and the diaphragm displacement are obtained for each diaphragm size. The model fails to predict the diaphragm behaviour at a temperature of 800°C because it underestimates the growth of the mobile dislocation densities under applied pressure. At 900°C, there is a fairly good match between the theoretical predications and experimental results for the diaphragms with radii from 0.5mm to 2.0mm. However, when the diaphragm radius is 2.5mm, the model overestimates the deflection without considering the slip resistance caused by high density of generated dislocations.

In order that the designed silicon diaphragm could work properly in high temperature environment, there are four suggestions from this research. Firstly, either increasing diaphragm radius or increasing operating temperature will increase the risk of creep and plastic deformation. Therefore, the diaphragms with small size are more likely to survive in high temperature environment. Secondly, the diaphragm sensitivity to pressure decreases with the diaphragm dimensions. So the diaphragm dimension should be chosen carefully in order that the device lifetime and sensitivity are well balanced. In addition, the transduction mechanism needs to be selected carefully in order that the pressure induced signal can be sensed with a desired resolution. Thirdly, it is better to avoid the ion implantation in the micromachining process in order to reduce the risk of the plastic deformation. The fourth recommendation is that for all the designed diaphragms, it is necessary to evaluate their creep deformation according to the application requirements.

7.2 *Suggestion for future work*

The plastic deformation of the silicon diaphragm at high temperature is caused by the slip of dislocations. The slip bands have been observed on the plastically deformed diaphragm surface. In the constitutive model, the density of mobile dislocations is an important variable controlling the plastic shear strain rate in the early stage of deformation. In this research, the TEM sample has been prepared successfully by the FIB/SEM workstation in our laboratory. So the TEM study of the dislocations in plastic deformed silicon is suggested for future work. The study can help to verify the occurrence of the plastic deformation, especially for small diaphragms whose plastic deflection might be too small to be measured. For Ar^+ implanted silicon samples, TEM study of the resultant defects can help to reveal the effect of the ion implantation on the diaphragm plasticity. Because the TEM study of dislocations belongs to the field of material science, it is a good complement to current research which is focused on the mechanical aspect of the plastic deformation. At last, the observed dislocation densities by TEM can help to modify the constitutive model. It is known that the model fails to predict the plastic deformation of the silicon diaphragm at 800°C because it underestimates the growth of the dislocations. Therefore, it may be possible to modify the material parameters using the observed dislocation density, and thus modify the constitutive model.

The presented constitutive model has reasonably predicted the plastic deformation at early stage for silicon diaphragms with radii from 0.5mm to 2.0mm at 900°C. However, it overestimates the plastic deformation for the diaphragm with a radius of 2.5mm. This is because current model regards the dislocation density as a governing

variable for the diaphragm deformation, and the slip resistance caused by the dislocation interactions is not included in the later deformation stage due to the limitation of Comsol Multiphysics 3.5a (see section 5.3). So in the future work, it is suggested to implement the constitutive equations in other FEA software, such as Abaqus. A good reference of the complete set of the constitutive equations for single crystal silicon is presented by Moon and co-workers [7-2]. Then the improved model should be able to predict the diaphragm deformation through all anneal processes.

This thesis gives a comprehensive understanding of the silicon diaphragm behaviour. It shows that by careful design of the diaphragm dimension, the micromachined silicon diaphragm is possible to survive at high temperature environment under atmospheric pressure. However, lots of work needs to be done for the design of a high temperature pressure sensor, for example, the selection of the transduction mechanism, and the package of the sensor device. And most importantly, the creep deformation of the diaphragm can be a major design consideration when the plastic deformation is avoided. Therefore, it is also necessary to evaluate the effect of creep on the sensor output once the test device has been made.

List of References

[7- 1] Shuwen, Q., H. Eriksen, et al. (2008). High temperature high accuracy piezoresistive pressure sensor based on smart-cut soi. Micro Electro Mechanical Systems, 2008. MEMS 2008. IEEE 21st International Conference.

[7-2] Moon H-S, Anand L, Spearing SM. A constitutive model for the mechanical behavior of single crystal silicon at elevated temperatures. In: Mat Res Soc Symp Proc 687, Paper B9.6, (2002)